การวิเคราะห์เชิงโครงสร้างของฟิล์มอินเดียมไนไตรด์แบบคิวบิกที่ปลูกผลึกด้วย
วิธีโมเลกุลาร์บีมเอพิแทกซี

นายสมาน คันธรินทร์

STRUCTURAL ANALYSIS OF CUBIC InN FILMS GROWN BY
MOLECULAR BEAM EPITAXY
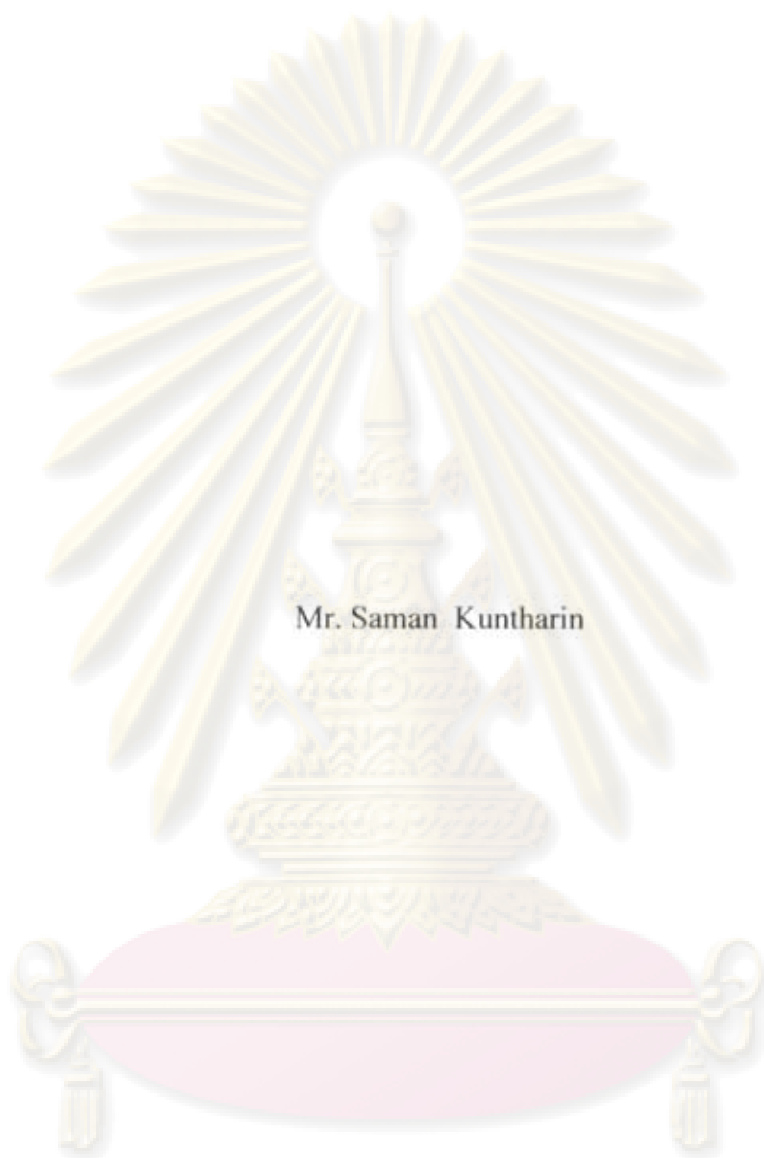
Mr. Saman Kuntharin

A Thesis Submitted in Partial Fulfillment of the Requirements
for the Degree of Master of Science Program in Physics
Department of Physics
Faculty of Science
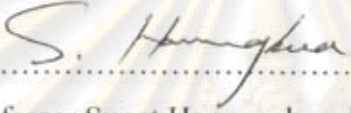Chulalongkorn University
Academic year 2007
Copyright of Chulalongkorn University

500509

Thesis Title	STRUCTURAL ANALYSIS OF CUBIC InN FILMS GROWN BY MOLECULAR BEAM EPITAXY
By	Mr. Saman Kuntharin
Field of study	Physics
Thesis Advisor	Assistant Professor Sakuntam Sanorpim, Ph.D.

Accepted by the Faculty of Science, Chulalongkorn University in Partial Fulfillment of the Requirements for the Master's Degree

....Dean of the Faculty of Science

(Professor Supot Hannongbua, Ph.D.)

THESIS COMMITTEE

..........Wichit Sritrakool........ Chairman

(Associate Professor Wichit Sritrakool, Ph.D.)

.... Thesis Advisor

(Assistant Professor Sakuntam Sanorpim, Ph.D.)

.... Member

(Assistant Professor Somchai Kiatgamolchai, Ph.D.)

.... Member

(Narumon Suwonjandee, Ph.D.)

สมาน คันธรินทร์: การวิเคราะห์เชิงโครงสร้างของฟิล์มอินเดียมไนไตรด์แบบคิวบิกที่ปลูกผลึกด้วยวิธีโมเลกุลาร์บีมเอพิแทกซี (STRUCTURAL ANALYSIS OF CUBIC InN FILMS GROWN BY MOLECULAR BEAM EPITAXY) อ. ที่ปรึกษา: ผศ. ดร. สกุลธรรม เสนาะพิมพ์, 81 หน้า.

ในวิทยานิพนธ์นี้ การเปลี่ยนแปลงเชิงโครงสร้างและคุณภาพผลึกของฟิล์มคิวบิกอินเดียมไนไตรด์ (cubic InN หรือ c-InN) ปลูกผลึกลงบนซับสเตรตระนาบ (001) ด้วยวิธีโมเลกุลาร์บีมเอพิแทกซีได้ถูกตรวจสอบและวิเคราะห์อย่างเป็นระบบ ผลกระทบจากเงื่อนไขการปลูกผลึก คือ สภาวะการปลูกผลึกที่มีอินเดียมและไนโตรเจนที่มากเกินพอ และชั้นบัฟเฟอร์ได้ถูกพิสูจน์ จากการวัดการเลี้ยวเบนรังสีเอ็กซ์กำลังแยกสูงและการกระเจิงแบบรามาน เราพบว่าฟิล์มบาง InN ที่ถูกใช้ในการศึกษานี้ มีโครงสร้างผลึกแบบคิวบิกและประกอบด้วยโดเมนย่อยของโครงสร้างผลึกเฮกซะ-โกนัลที่วางตัวเอียงเทียบกับระนาบ (001) ผลการทดลองนี้ยืนยันว่า โครงสร้างผลึกเฮกซะโกนัลได้ก่อเกิดบนระนาบ {111} และกลายเป็นโครงสร้างผลึกหลักในฟิล์ม c-InN ที่ถูกปลูกผลึกภายใต้สภาวะที่มีไนโตรเจนมากเกินพอ ในทางตรงกันข้าม ฟิล์มที่มีคุณภาพผลึกสูงกว่าและมีการเจือปนของโครงสร้างผลึกเฮกซะโกนัล ในปริมาณที่ต่ำกว่า ได้ถูกปลูกผลึกภายใต้สภาวะที่มีอินเดียมมากเกินพอ นอกจากนี้เรายังพบอีกว่า สำหรับการใช้คิวบิกแกลเลียมไนไตรด์เป็นชั้นบัฟเฟอร์นั้น โครงสร้างผลึกเฮกซะโกนัลในชั้นบัฟเฟอร์มีอิทธิพลอย่างมาก ต่อการก่อเกิดของโครงสร้างผลึกเฮกซะโกนัลและคุณภาพผลึกของชั้นฟิล์ม c-InN ที่ถูกปลูกผลึกต่อเนื่องบนชั้นบัฟเฟอร์ ผลการทดลองนี้แนะนำว่า ชั้นบัฟเฟอร์ที่มีการเจือปนของโครงสร้างผลึกเฮกซะโกนัลในปริมาณที่ต่ำเหมาะสม สำหรับการปลูกผลึกของฟิล์ม c-InN ที่มีคุณภาพผลึกและมีความบริสุทธิ์ของโครงสร้างผลึกแบบคิวบิกสูง ผลการวิจัยได้แสดงให้เห็นว่า เงื่อนไขการปลูกผลึกที่มีอินเดียมมากเกินพอและคุณภาพของชั้นบัฟเฟอร์ มีบทบาทสำคัญในการปลูกผลึกของฟิล์ม c-InN ให้มีคุณภาพผลึกและความบริสุทธิ์ของโครงสร้างแบบคิวบิกที่สูง โดยปราศจากการก่อเกิดของโครงสร้างผลึกเฮกซะโกนัล

ภาควิชา................ฟิสิกส์.................... ลายมือชื่อนิสิต...
สาขาวิชา..............ฟิสิกส์.................... ลายมือชื่ออาจารย์ที่ปรึกษา.....................................
ปีการศึกษา…...........2550.............

4872497023: MAJOR Physics
KEY WORD: CUBIC InN / MOLECULAR BEAM EPITAXY / HIGH RESOLUTION X-RAY DIFFRACTION / RAMAN SCATTERING / CRYSTAL STRUCTURE / STRUCTURAL DEFECTS

SAMAN KUNTHARIN: STRUCTURAL ANALYSIS OF CUBIC InN FILMS GROWN BY MOLECULAR BEAM EPITAXY. THESIS ADVISOR: ASST. PROF. SAKUNTUM SANORPIM, PH.D., 81 pp.

In the thesis, the structural modification and crystal quality of the cubic InN (c-InN) films grown on (001) substrates by molecular beam epitaxy have been systematically investigated and analyzed. The effects of the growth conditions, namely In- and N-rich conditions, and the buffer layer are established. Based on high-resolution X-ray diffraction and Raman scattering measurements, we found that the InN films used in this study have a cubic structure and contain some amount of hexagonal phase subdomains tilted from the (001) plane. These results confirm that the hexagonal phase is generated on the cubic {111} planes and becomes dominance in the c-InN films grown under the N-rich growth condition. In contrast, the films with higher crystal quality and lower hexagonal phase inclusion were grown under the In-rich growth condition. Furthermore, we also found that, with using c-GaN as a buffer layer, the hexagonal phase presented in the buffer layer greatly influences the hexagonal phase generation and crystal quality of the c-InN upper films. This result suggests that the buffer layer with lower hexagonal phase incorporation is suitable for growing the c-InN layers with high crystal quality and high cubic-phase purity. These results demonstrate that the In-rich growth condition and the crystal quality of the buffer layer play an important role in growing high cubic-phase purity c-InN films without generation of hexagonal phase structure.

Department.......... Physics.........................Student's signature...................................

Field of study.........Physics…......................Advisor's signature.................................

Academic year.........2007...............

Acknowledgements

CONTENTS

Chapter   **Page**

List of Tables

List of Figures

Figure   **Page**

Figure   **Page**

CHAPTER I

INTRODUCTION

1.1 Overview of InN

The family of III-nitride semiconductors (GaN, InN and AlN) is one of the promising candidate materials for optoelectronic devices such as light emitting diodes (LEDs), laser diodes (LDs) and solar cells. This is due to the bandgap of the three binary compounds and their alloys covered the spectral region from the infrared to the deep ultraviolet as shown in Fig. 1.1. It is seen that a key component for bandgap energies in the infrared to visible ranges is InN. However, among the three binary InN is still the least explored, due to difficulties in synthesizing high quality single crystal. This problem has been overcome owing to the recent development of the material growth techniques. But, many of the key band parameters have not been conclusively determined until now. The most controversially discussed band parameter is still the fundamental bandgap of InN. For many years, it was believed to be about 1.9 eV [1-3] but other values between 0.65 and 2.3 eV [4, 7] have been also reported. However, recent experiments on higher crystal quality InN film grown by molecular beam epitaxy (MBE) [5-15] and metalorganic vapor phase epitaxy (MOVPE) [16-19] significantly support the lower value around 0.6 - 0.8 eV [9, 12, 15, 20-21]. This suggests that InN single crystal has a much smaller bandgap than the commonly accepted one based on early experiments. Thus, the III- nitride-based optoelectronic devices can now extend to the infrared range of 1.30 μm and 1.55 μm. Furthermore, InN has been predicted to have
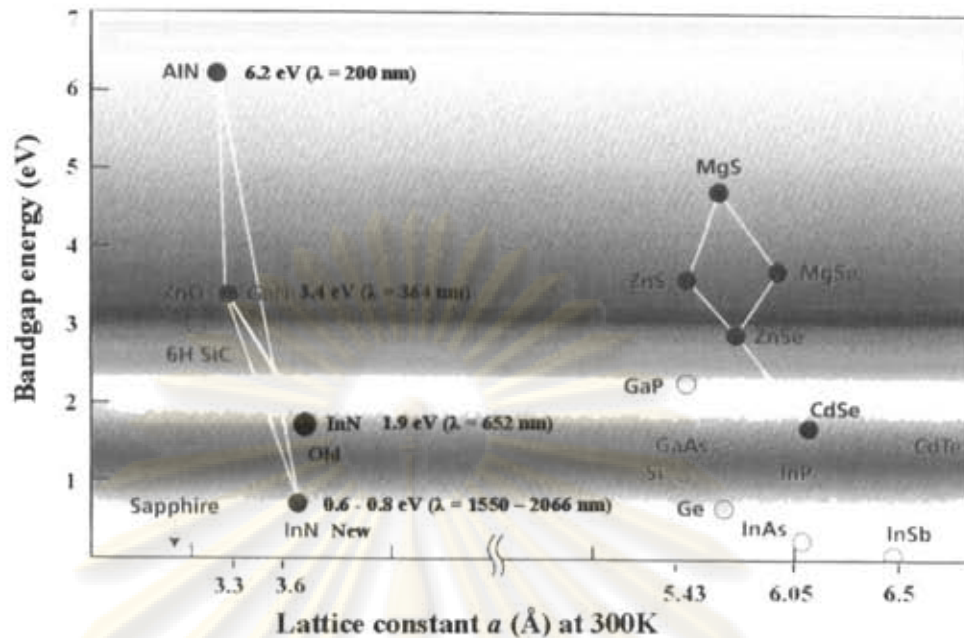
Figure 1.1: Relationship between bandgap energy and lattice constants of binary compound semiconductors [27]. The white line indicates the relationship for their alloys.

the smallest electron effective mass [22] resulting in the highest electron mobility suitable for high-frequency high-speed devices. In addition, InN can also be a potential material for low cost solar cells with higher efficiency. Yamamoto *et. al.* [23] has proposed InN for a top cell material of a two-junction tendem solar cells with conversion efficiency over 30%.

Commonly, the stable crystal structure for the III-nitride semiconductors is the hexagonal structure (wurtzite structure) as shown in Fig. 1.2 a). However, they have been reported to have also the cubic structure (zinc blend structure) (Fig. 1.2 b)) as a metastable phase when grown on substrates having cubic symmetry. For example, cubic phase GaN (c-GaN) was successfully grown on cubic substrates such as GaAs [24] and 3C-SiC [25]. As cubic crystal has higher crystallographic symmetry than hexagonal one, it is expected that cubic phase InN (c-InN) would exhibit lower phonon scattering and different electronic characteristics (bandgap, impurity level, etc.). These reasons have motivated the study of c-InN as a potential material for infrared or high-speed electronic device applications.
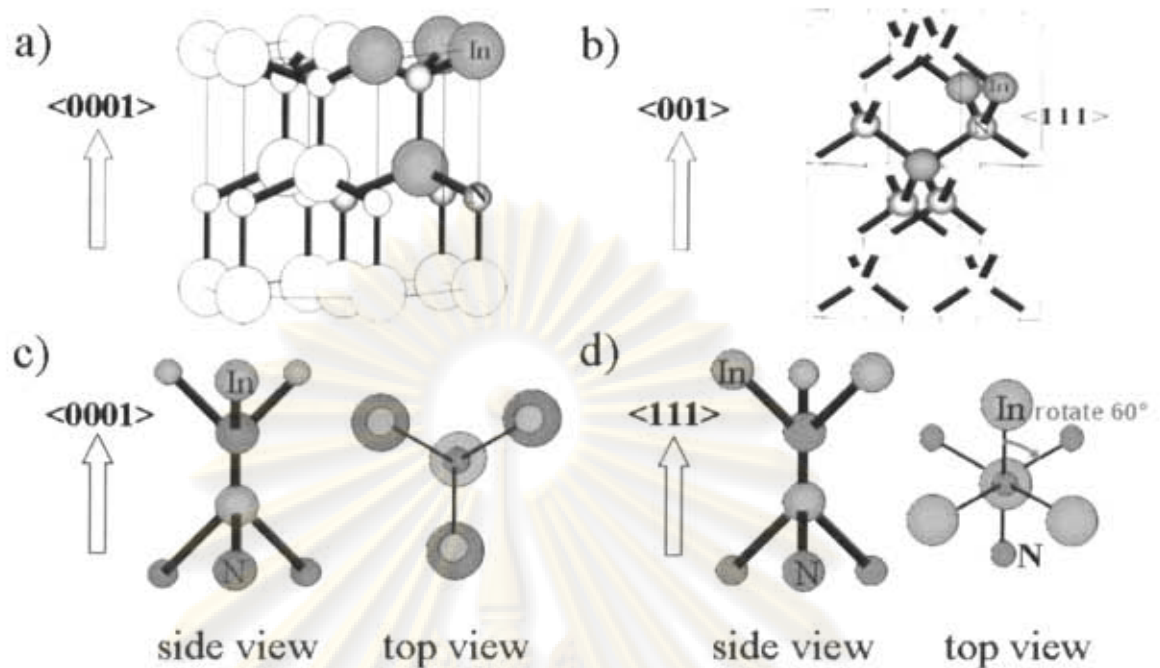
Figure 1.2: Schematic illustration of InN crystal structures, a) hexagonal (wurtzite) structure, b) cubic (zinc blend) structure, c) hexagonal structure along <0001> direction and d) cubic structure along <111> direction. Note that the difference between these two crystal structures is only a rotation 60° along cubic <111> and hexagonal <0001> directions.

1.2 Material problems of c-InN

Up to now, c-InN is not well studied, mostly because high quality c-InN films are difficult to grow. Thus, there are relatively few reports on c-InN [11-12, 15] and the published data are mainly on hexagonal phase InN (h-InN) [5-10, 13-14]. There are several reasons for this situation. The first one is due to the metastable of cubic phase. Growth of metastable phase is unfavorable under the equilibrium growth condition used in MOVPE technique, which is the most common growth method for III-nitride semiconductor [26]. Using the MBE growth method, which is well known as a nonequilibrium growth method, it has been proven the growth of the cubic III-nitride film

with good crystalline quality. The second reason is also due to metastability of the cubic III-nitride crystal, the hexagonal phase is often unexpectedly introduced in the cubic layer. In fact, it has been reported that most of hexagonal phase presented in the cubic III-nitride crystal, such as c-GaN, has generated on the cubic {111} planes as a formation of planar defects, such as stacking faults, twins and hexagonal-phase subdomain. This is because the fundamental difference between cubic and hexagonal structures, which is merely a 60° rotation along the hexagonal <0001> (Figs. 1.2 c) and 1.3 b)) and cubic <111> (Figs. 1.2 d) and 1.3 a)) directions. Thus, the cubic {111} planes can accommodate the growth of hexagonal structure along <0001> direction. Three possible models of the generation of hexagonal structure in the cubic III-nitride layers are shown in Fig. 1.4. There are a number of common properties as following:

(1) Stacking faults in cubic {111} planes is an insertion of 1 monolayer of hexagonal between two cubic structures, which are identical crystal orientation (Fig. 1.4 a)).

(2) Twins in cubic {111} planes are formed by the insertion of stacking fault (1/2 monolayer of hexagonal) between two of cubic structures, which are different crystal orientations (Fig. 1.4 b)).

(3) Hexagonal phase subdomain generated on the cubic {111} planes is an extension of stacking faults to be a single crystal of hexagonal structure (Fig. 1.4 c)).

Density and distribution of such planar defects seriously affect on both the crystalline quality and electronic properties of cubic III-nitride films. Thus, it will be helpful for the epitaxial growth to measure an amount of the mixed structural phases and to analyze their formation mechanism for future device improvement.

Another problem that affects the crystal growth of c-InN is a lack of suitable substrates. Table 1.1 summarizes the lattice constants and thermal expansion coefficients of c-InN film and some prospective substrate materials [27]. As shown in Table 1.1, there is a large difference of lattice constants and thermal expansion coefficients between c-InN and the substrate materials. This large mismatch causes a high density of structural defects such as threading dislocations and stacking faults in InN epitaxial films. To improve the quality of c-InN grown film, there are several research groups, which are studying and finding for the affecting parameters, such as growth methods, growth

a)

b)
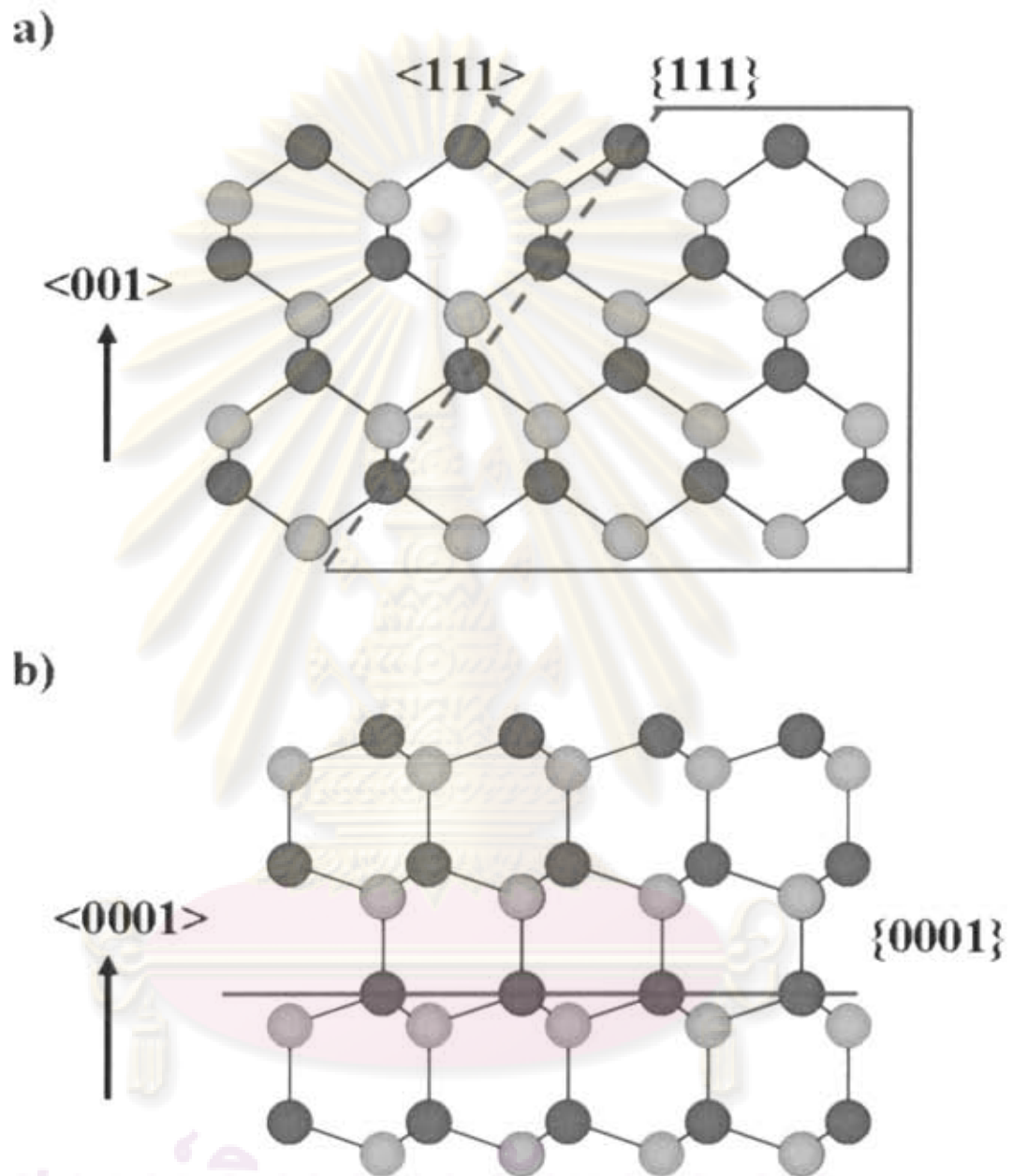
Figure 1.3: Two-dimensional atomic models of crystal structure for InN along (-110) cross-section, a) cubic structure and b) hexagonal structure.

6
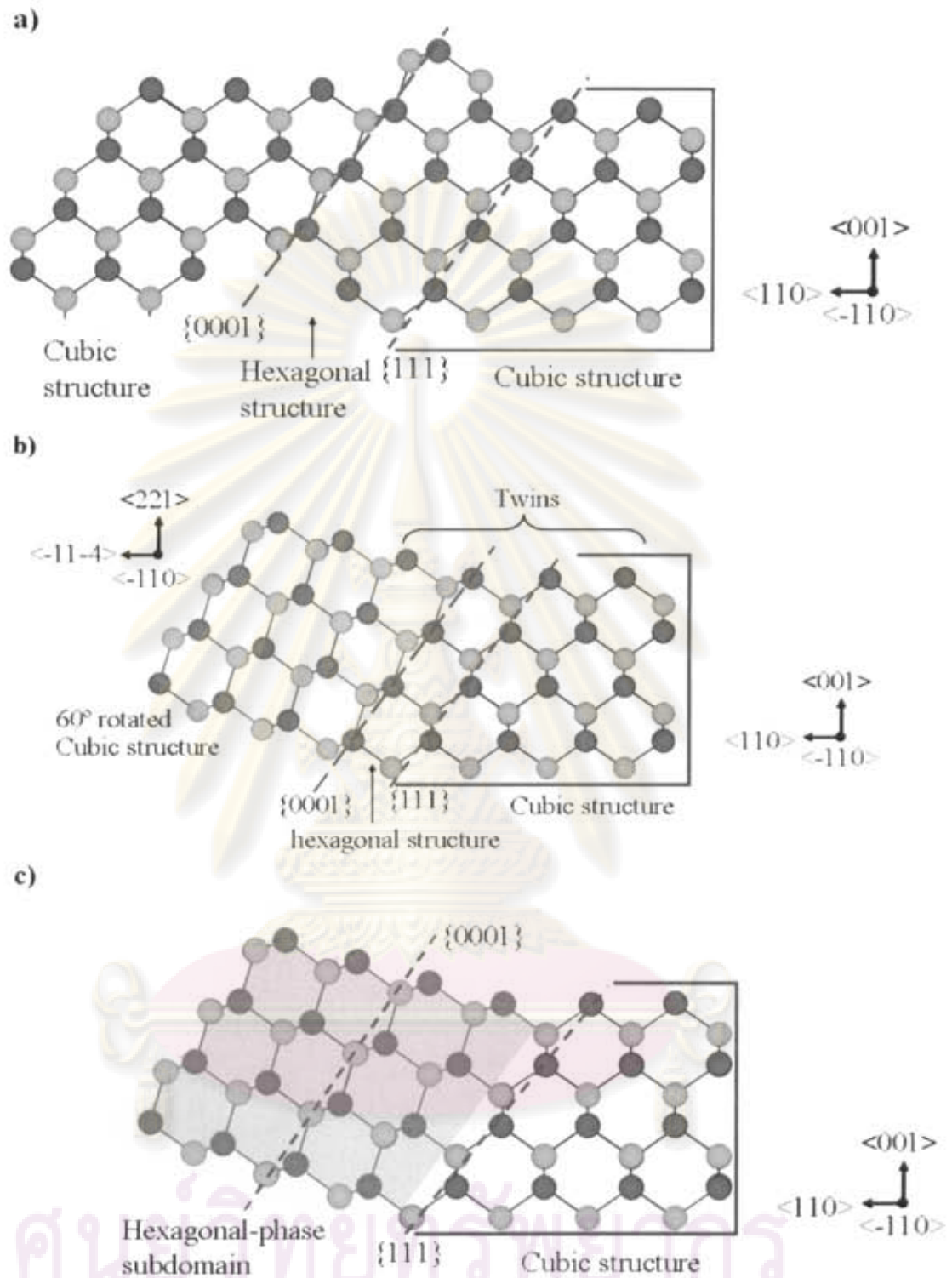
Figure 1.4: Schematic view of possible structures of planar defects, namely a) stacking faults, b) twins and c) hexagonal-phase subdomain in cubic structure along (-110) cross-section [46].

Substrate materials	Lattice constants (Å)	Lattice mismatch (%)	Thermal expansion coefficients ($\times 10^{-6}$ K^{-1})
c-InN	4.98	0	3.8
c-GaN	4.502	-10.67	3.17
MgO	4.210	-18.29	10.5
3C-SiC	4.359	-14.23	3.9
GaAs	5.653	+11.90	6.0

Table 1.1: Lattice constants, lattice mismatch and thermal expansion coefficients for substrate materials of c-InN film [27].

conditions, substrate material, etc. In fact, the c-InN epitaxial films were successfully grown by MBE on MgO [11] and GaAs [12] substrates despite the large mismatch. Nakamura *et al.* [12], for example, reported that the high quality c-InN films were successful grown on GaAs (001) substrate at relatively high temperature (~500°C) and low V/III ratio, corresponding to the In-rich growth conditions. Moreover, Iwahashi *et. al.* [11] suggested that the group III-atom rich growth conditions are essential to the growth of cubic III-nitride semiconductors. However, there are a number of structural defects, which degrade the optical and crystal qualities.

As mentioned above, many affecting parameters were found to obtain high quality of the c-InN film, in this work we focus on the growth conditions, specifically In- and N-rich growth conditions, which may result in the generation of crystal defects during the growth. Effects of the buffer layer on the crystal quality are also mentioned.

1.3 Objectives and organization of the thesis

The aim of the thesis is to investigate and analyze the generation of crystal defects in the c-InN layers grown by MBE. The effects of the In- and N-rich growth conditions as well as the buffer layer on the coexistence of hexagonal phase in the c-InN films were

investigated. The thesis is organized as follows:

Chapter II: In this chapter, we introduce the experimental techniques, including high-resolution X-ray diffraction (HRXRD) and Raman scattering, which are used to study structural modification and crystal quality of the c-InN films. The basic principal, advantages, limitations and interpretation of these techniques are described. Then, for instance, we show the effectiveness of these techniques, which are used to certify the crystal quality and structural phases in the c-InN grown film.

Chapter III: This chapter focuses on the effects of growth conditions, namely In- and N-rich growth conditions, on the structural modification and crystal quality of the c-InN film on GaAs (001) substrates by MBE. Firstly, the growth identification of In- and N-rich conditions is described. Based on the results of HRXRD and Raman scattering, correlation between the In- and N-rich growth conditions and the hexagonal phase generation in c-InN grown films are discussed. It is found that the hexagonal phase is constructed on the cubic $\{111\}$ planes and becomes the main crystal structure in the c-InN films grown under the N-rich growth condition. To quantitatively determine an amount of hexagonal/cubic ratio or called "hexagonal phase inclusion", the theoretical calculation of integrated XRD intensities of the cubic (002) and hexagonal (10-11) planes measured by the ω-scan is purposed. Consequently, we modified the effecting parameters to calculate the integrated XRD intensities for the InN crystal, which have never been reported before, then applied them to determine the amount of hexagonal phase inclusion in the c-InN films. Our results suggest that the In-rich growth conditions play a critical role in the growth of single structural phase c-InN with higher crystalline quality.

Chapter IV is a continuation of Chapter III. This chapter focuses on the c-InN on MgO (001) substrates grown under the In-rich growth condition with a c-GaN buffer layer. Crystal structures investigated by HRXRD and Raman scattering is described. The effects of the hexagonal phase presented in the c-GaN buffer layer on structural modification and crystal quality of the c-InN films are mainly discussed. In addition, the correlation between the amount of hexagonal phase inclusion and vibrational properties of the c-InN films are also addressed.

Finally, Chapter V gives the conclusions of the thesis.

CHAPTER II

EXPERIMENTAL TECHNIQUES
AND INTERPRETATIONS

In this chapter, we discuss the measurement and analysis of epitaxial structures. After describing experimental techniques including high-resolution X-ray diffraction (HRXRD) and Raman scattering techniques, we show how to derive the basic parameters: lattice constant, crystal misorientation and tilt. We then discuss X-ray reciprocal space mapping, which is used to characterize all the structural phases in the samples and their amount.

2.1 Why high-resolution X-ray Diffraction?

In an epitaxial layer, the crystal information of the underlying single-crystal substrate is indented to be continued into the thin film. This material system exhibits a high degree of crystalline perfection. In order to resolve the very closely spaced peaks occurred in the diffraction pattern of the epitaxial layer-substrate material system, the special X-ray diffractometer is required. This is a reason for naming "high-resolution X-ray diffraction (HRXRD)". It often happens that observable peaks are as close as 0.001° [28]. Commonly, this spacing cannot be obtained with the X-ray diffractometer setting presented so far for the investigation of polycrystalline materials. This is due to the X-ray beam divergence and the spectral width of the
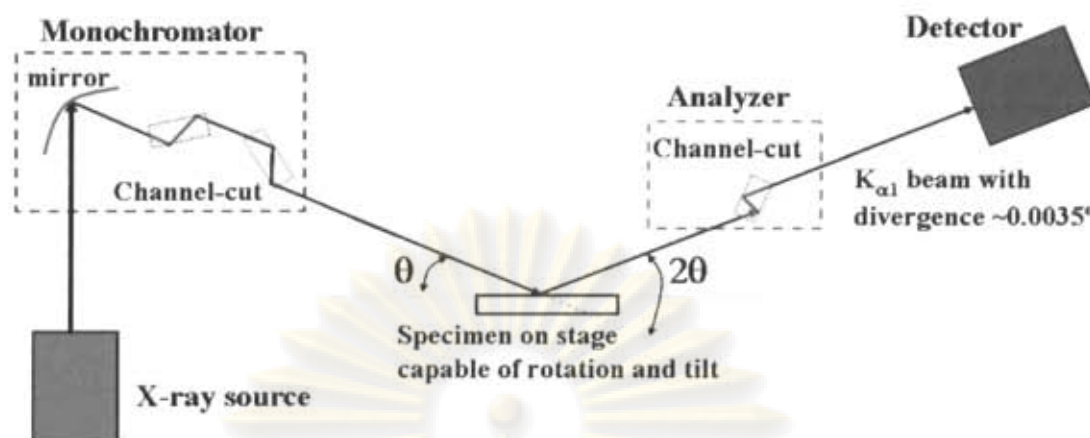
Figure 2.1: Diagram of high resolution X-ray diffraction arrangement.

characteristic X-ray lines. According to the formula of precision of interplanar spacing, $\Delta d / d$ [28].

$$\frac{\Delta d}{d} = \frac{\Delta \lambda}{\lambda} + \frac{\delta}{\tan \theta},$$

(2.1)

where $\Delta \lambda$ is the spectral width of the X-ray beam and δ is the beam divergence. To obtain the lowest value of $\Delta d / d$, we need to limit the divergence and wavelength spread of the X-ray beam incident upon the specimen. As a result, we see that the requirement is for a system with high "angular resolution" and sufficient "monochromatisation".

2.2 High resolution system

Figure 2.1 shows a diagram of a higher resolution X-ray diffractometer, which is known as a three-axis instrument. The three axes are those controlling the monochromator, the specimen and the analyzer. The monochromator consists of two components: a graded parabolic mirror and a channel-cut crystal. The graded parabolic mirror eliminates the K_β[a] radiation and the channel-cut crystal removes the

---

[a]K_β: Emission lines results when electron transition to the ground state "K" shell (quantum number n = 1) from a 3P orbital of the "M" shell (n = 3)

$K_{\alpha2}$[a] component from the X-ray beam. For the analyzer, a secondary channel-cut crystal was used to select X-ray beams that are scattered from the sample within a limited angular acceptance of the detector. Note that the channel-cut crystals, such as Si (220), Si (111) and Ge (220), are widely used to provide a high resolution option for the III-V and II-VI semiconductor systems [29].

HRXRD is very important technique that has been used to analyze crystal structure of the epitaxial layer, such as lattice constant, crystal orientations, etc. The measurement is performed by projecting the X-ray beam onto the sample. The diffraction condition can be occurred according to Bragg's law

$$2d_{hkl} \sin \theta_B = \lambda, \qquad (2.2)$$

where d_{hkl} is the lattice plane spacing of the (hkl) plane, θ_B is the Bragg's angle and λ is the wavelength of X-ray. Despite the implication that the HRXRD technique is only applicable to very high perfection material, Tlafford et al. [29] reported that it is also highly appropriate to relatively poor epitaxy materials such as GaN.

In this study, HRXRD measurements were performed using the Bruker-AX8 D8 DISCOVER at Scientific and Technology Research Equipment Center, Chulalongkorn University. Figure 2.2 shows HRXRD instrument with a conventional Cu target operated at 40 kV and 40 mA. The CuK_α radiation is monochromatized into $K_{\alpha1}$[b] ($\lambda = 1.5406$ Å with $\Delta\lambda / \lambda = 3 \times 10^{-4}$ [28]) by a four-crystal Ge (022) channel-cut monochromator. In addition, a two-crystal Ge (022) channel-cut analyzer was placed in front of the detector to restrict the angular acceptance of the detector.

2.3 Interpretation of HRXRD results

2.3.1 $2\theta / \omega$-scan mode

In HRXRD measurements, most frequently used scan mode is $2\theta / \omega$-scan. In this mode, variations of lattice plane spacings are detected. For epitaxial layers, only

---

[a] $K_{\alpha2}$: Emission lines results when electron transition to the ground state "K" shell ($n = 1$) from a 2P orbital of the "L" shell ($n = 2$, and $l = 3/2$)

[b] $K_{\alpha1}$: Emission lines results when electron transition to the ground state "K" shell ($n = 1$) from a 2P orbital of the "L" shell ($n = 2$, and $l = 1/2$)

a)

Monochromator

Detector

X-ray source

Analyzer

Specimen on stage capable of rotation and tilt

Power supply

b)

Monochromator   Analyzer

Detector

Specimen

X-ray source
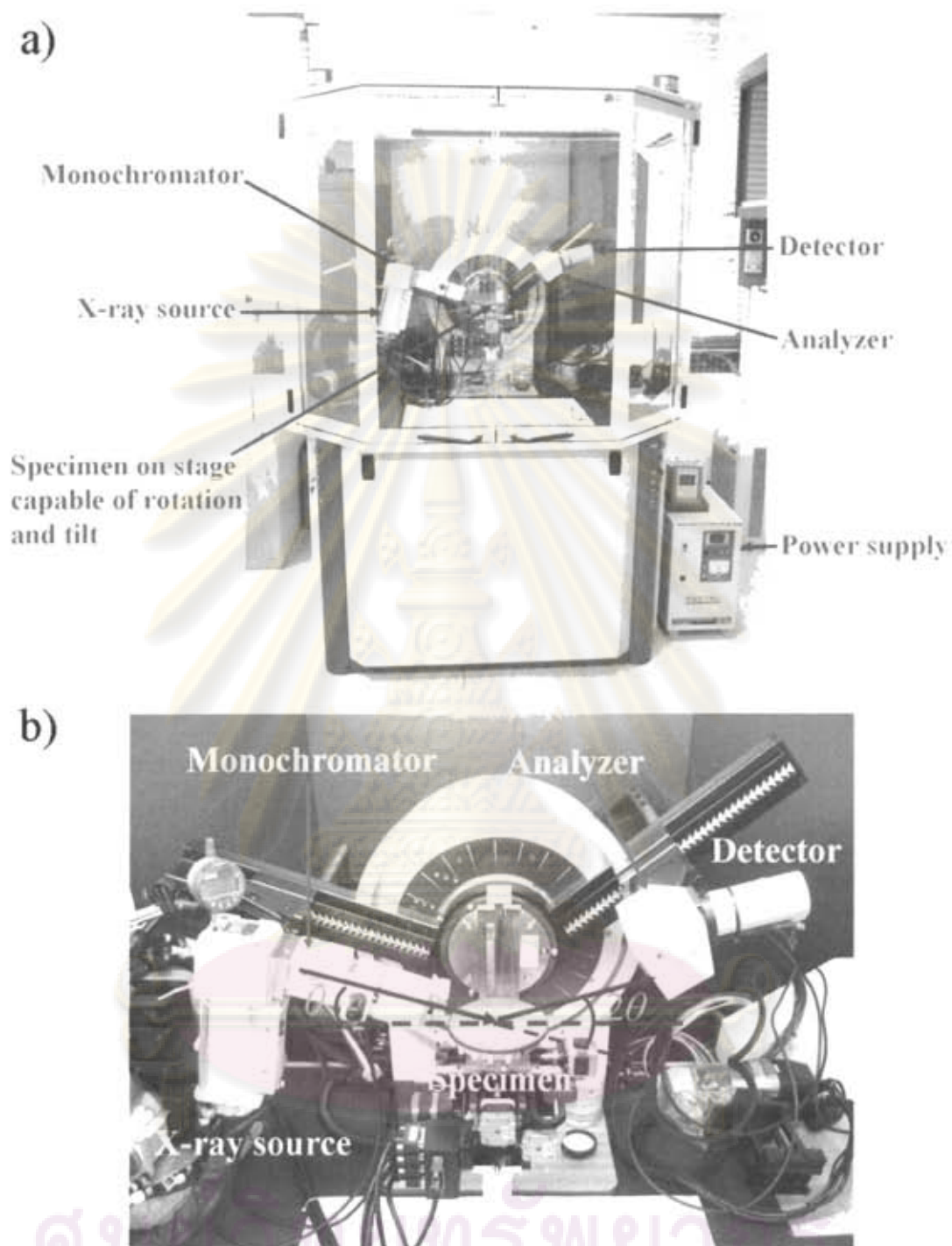
Figure 2.2: Schematic diagram of HRXRD instrument at Scientific and Technology Research Equipment Center, Chulalongkorn University.
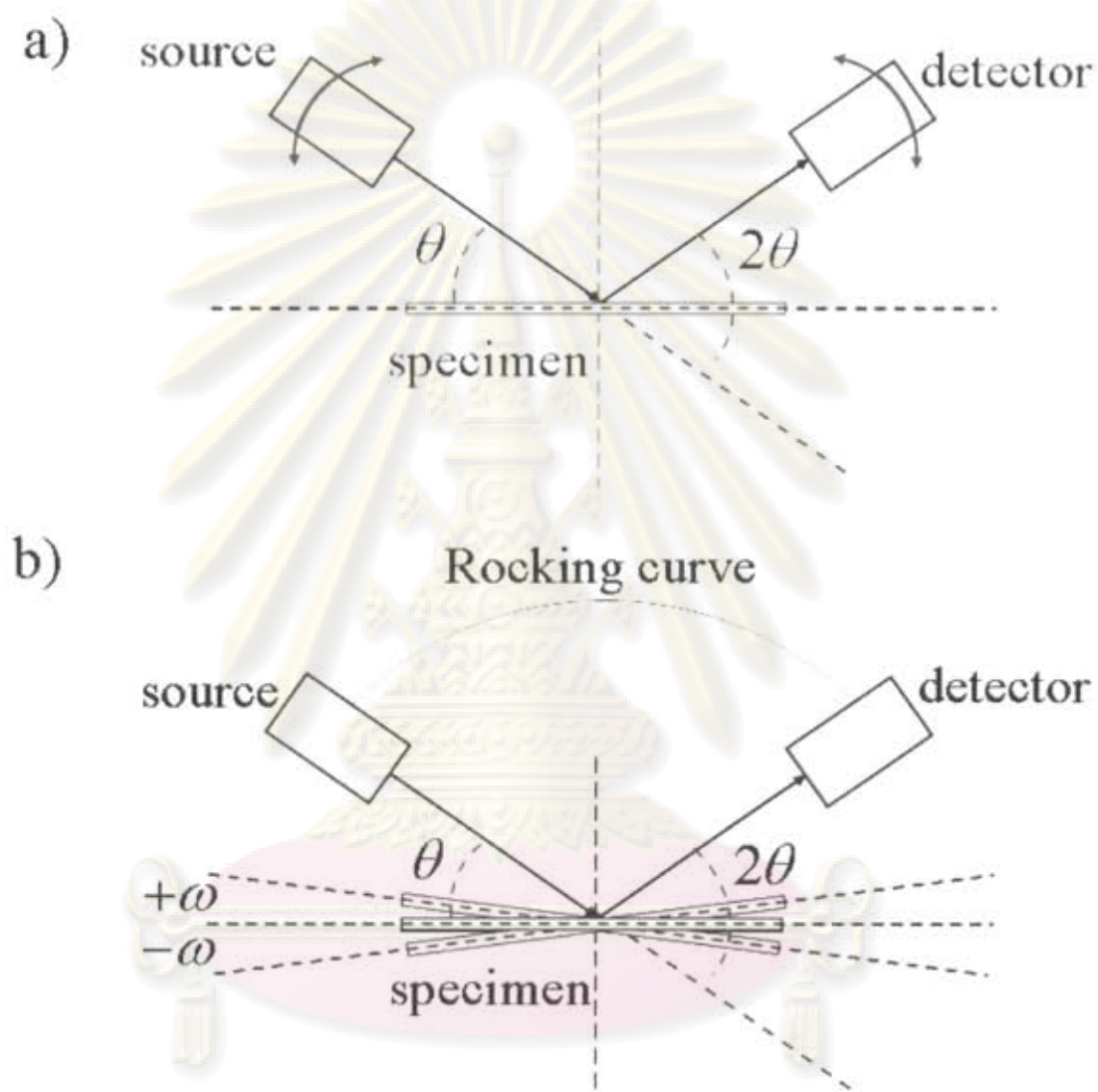
Figure 2.3: Schematic illustrations of the HRXRD measurements in a) $2\theta/\omega$-scan and b) ω-scan modes.

the lattice plane spacings parallel to the film surface are usually measured. The HRXRD measurements in $2\theta/\omega$-scan mode is shown in Fig. 2.3 a). The diffraction pattern is collected by varying the incident angle θ of the incoming X-ray beam and the scattering angle 2θ, while the specimen is fixed. Then, the scattered X-ray intensity is measured as a function of the scattering angle 2θ. For example, Fig. 2.4 a) shows a typical (002) $2\theta/\omega$-scan profile obtained from c-InN film grown on GaAs (001) substrate (sample D discussed in Chapter III). The diffraction peaks corresponding to the GaAs (002) and c-InN (002) reflections are seen at $2\theta = 31.63°$ and $35.92°$, respectively. From these diffracted peak positions, the lattice plane spacings of both the GaAs (002) and c-InN (002) planes can be determined. The relationship between the lattice plane spacing (d_{hkl}) and lattice constant (a) for the cubic crystal can be expressed by

$$d_{hkl} = \frac{a}{\sqrt{h^2 + k^2 + l^2}},$$ (2.3)

In this case, (hkl) = (002) and $\theta_B = \frac{2\theta_B}{2}$. With a combination of these quantities and Eq. 2.3, then, Eq. 2.2 becomes

$$a \cdot \sin(\frac{2\theta_B}{2}) = \lambda,$$ (2.4)

For the c-InN crystal, $2\theta = 35.92°$, thus, Eq. 2.4 becomes

$$a \cdot \sin(\frac{35.92}{2}) = \lambda,$$ (2.5)

In this study, the CuK$_{\alpha1}$ with wavelength of 1.5406 Å is used. Then, the lattice constant of c-InN crystal was calculated to be 4.99 Å. In addition, the full width at half maximum (FWHM) of $2\theta/\omega$-scan reflects to the variations of lattice constants. As seen in Fig. 2.4 a), the FWHM of the GaAs (002) diffraction is much narrower than that of the c-InN (002) diffraction. This indicates that the variations of lattice plane spacing of GaAs (002) (a_c) are lower than that of the c-InN layer as schematically shown in Fig. 2.4 b). One of the causes of the large width compared
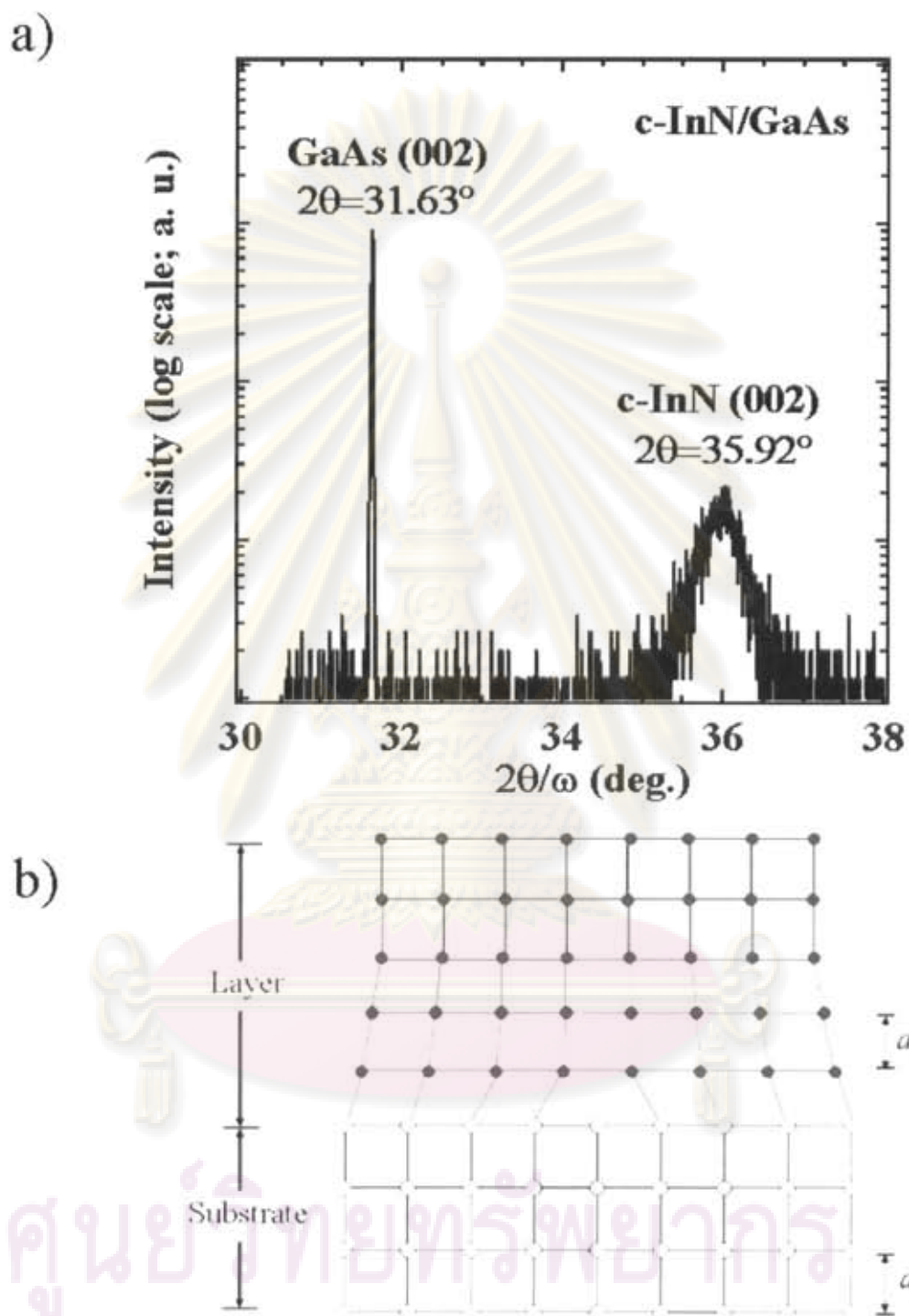
Figure 2.4: a) A typical (002) $2\theta/\omega$-scan profile and b) illustration of variations of lattice constant in the c-InN layer grown on the GaAs (001) substrate.

with GaAs substrate is the existence of a high density of dislocations and stacking faults in the epitaxial layer due to the large lattice mismatch between InN and GaAs.

2.3.2 ω-scan mode

In order to characterize c-InN epitaxial layers properly, it is also necessary to detect inclined or off-axis cubic and hexagonal planes from the film surface. Since, the mixing of the hexagonal phase and the inclination of cubic planes are serious problems. For this purpose, HRXRD measurements by rotating the sample along the ω-axis should be carried out. Contrary to $2\theta/\omega$-scan, ω-scan gives crystal orientation variation of a fixed plane distance. On the other hand, observed peak width corresponds to the reciprocal lattice point width perpendicular to the diffraction vector. The measurement of ω-scan is performed in the following conditions. The X-ray source and detector are fixed at the position of $2\theta_B$, which is corresponding to the interested Bragg angle. On the other hand, the specimen is tilted along the ω-axis in the vicinity of the Bragg angle θ_B. Therefore, ω is defined as the difference between the incident and the reflection angles into the specimen for a certain detection position. The HRXRD measurements in ω-scan mode is shown in Fig. 2.3 b). For the fixed value of $2\theta_B$, the value of ω is restricted to a range between $-\theta$ to $+\theta$. Thus, the peak position in the ω-scan mode refers to the inclination of epitaxial plane from the film surface. In addition, the FWHM in the ω-scan mode reflects to the variations of oriented crystal planes (mosaic). Figure 2.5 a) shows a typical (002) ω-scan profile obtained from the c-InN layer. In the experiment, the detector angle 2θ was set for the c-InN (002) diffraction plane ($2\theta = 35.92°$), and angle ω was scanned. It is found that the c-InN (002) plane is parallel to the film surface. The simple model of crystal orientation variation in the vicinity of (002) refection for the c-InN layer on GaAs (001) substrate is shown in Fig. 2.5 b).

2.3.3 X-ray reciprocal lattice space mapping

Two-dimensional scan composed of $2\theta/\omega$- and ω-scans give reciprocal lattice space mapping (RSM), which is used to characterize all the structural phases tilted from the film surface. Figure 2.6 shows the possible growth models of InN on GaAs (001) substrate in four different ways; a) c-InN (002) // GaAs (001), b) h-InN

a)

b)
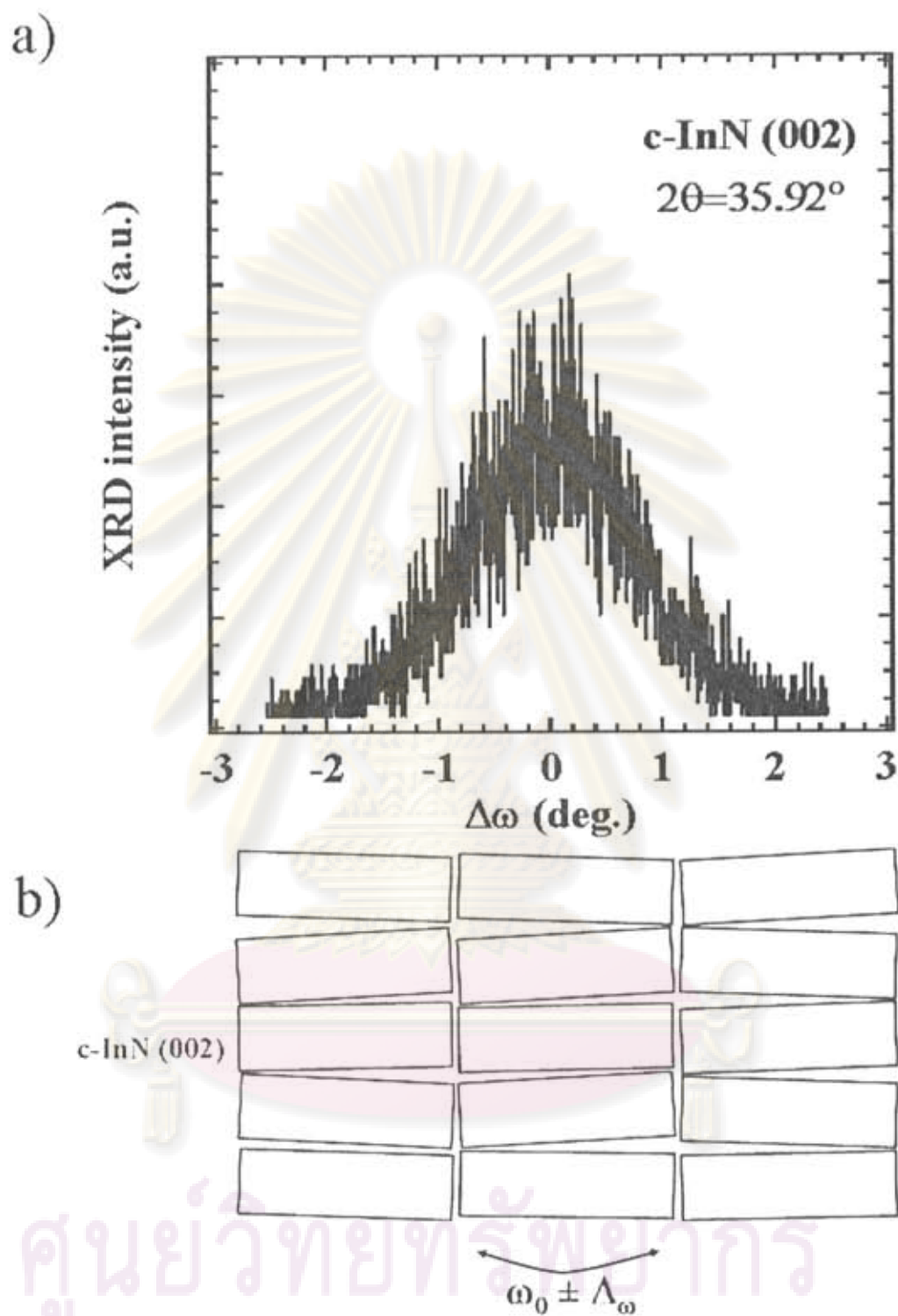
Figure 2.5: a) A typical (002) ω-scan profile of the c-InN layer on GaAs (001) substrate, which is shown in Fig. 2.4 and b) illustration of a simple model of crystal orientation variation in the vicinity of the c-InN (002) reflection.
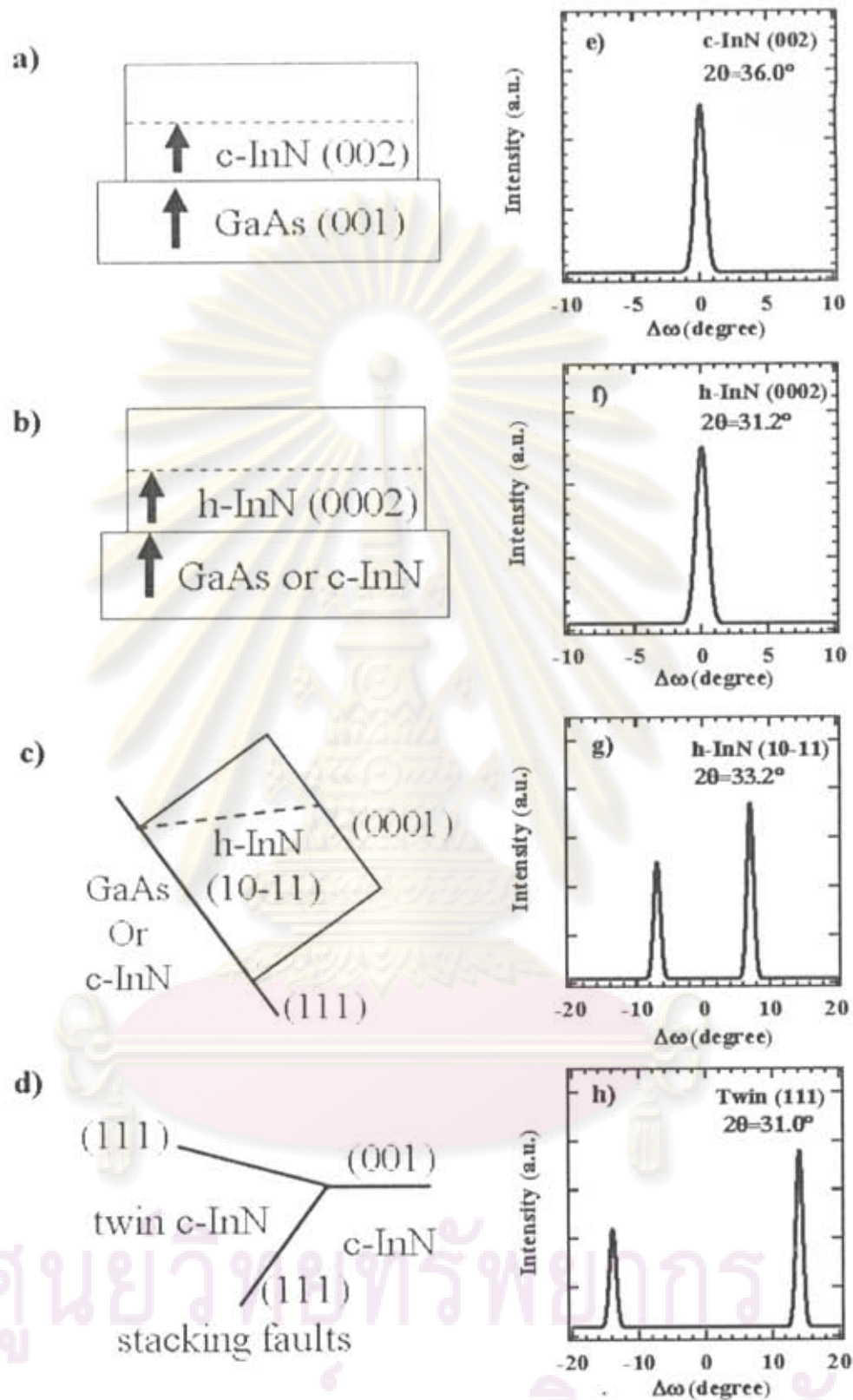
Figure 2.6: (a-d) Growth models of InN in four different ways and (e-h) the results measured by the ω-scan mode as reported in the case of GaN by F. Hasegawa [47].
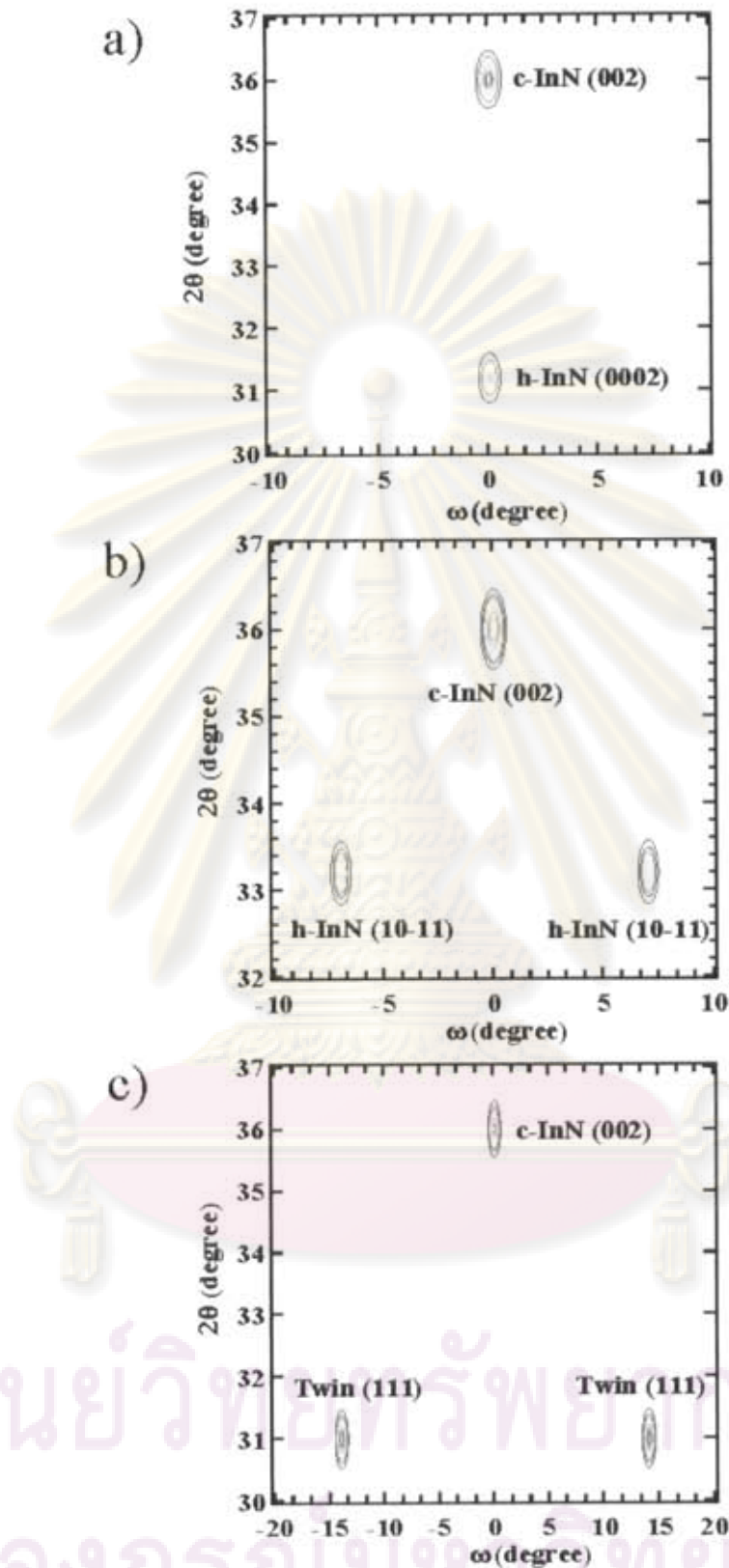
Figure 2.7: Schematic diagrams of possible X-ray reciprocal lattice space mappings of a) the (0002), and b) (10-11) diffractions of h-InN, and c) the (111) diffractions of twined c-InN presented in the c-InN layer grown on cubic (001) substrate.

(0002) // GaAs (001), c) h-InN (0002) // GaAs (111) or c-InN (111) and d) twined c-InN (111). To detect all the structural phases as shown in Figs. 2.6 a) – d), the ω-scan mode was performed for the fixed $2\theta_B$ of each crystal planes. Figures 2.6 e) – h) show the ω-scan profiles of cubic (002), hexagonal (0002), hexagonal (10-11) and twined (111) c-InN crystal planes, respectively. From ω-scan profile of the h-InN (0002) plane in Fig. 2.6 f), it is known that the InN layer has a hexagonal structure with [0001] direction perpendicular to the GaAs (001) substrate. On the other hand, from ω-scan profile of the h-InN (10-11) planes in Fig. 2.6 g), hexagonal (10-11) planes are tilted from GaAs (001) plane about ±7°. In this case, it is found that the <0001> axes of hexagonal domain in the layer is parallel to the <111> axes of the GaAs crystal, taking into account that the angles between the GaAs (001) and GaAs (111) planes and between hexagonal InN (0001) and hexagonal InN (10-11) planes were 54.7° and 61.8°, respectively. In addition, from ω-scan profile of the twined c-InN (111) planes in Fig. 2.6 h), the crystal orientation of twined cubic domain can also be observed with the same way.

Therefore, the X-ray RSM mode in HRXRD measurements is highly applicable to record all the structural phases shown in Fig. 2.6. Figure 2.7 displays schematic diagrams of X-ray RSMs of the c-InN film on the cubic (001) substrate measured along the [110] direction, corresponding to the growth models of InN described above. The case along [1-10] direction is similar to that along [110] direction. The related diffractions from different planes are labeled in the figure. Besides the (002) diffraction peak of c-InN, the (0002) and (10-11) diffraction peaks of h-InN and the (111) diffraction peak of twined c-InN are seen in Figs. 2.7 a), b) and c), respectively. This indicates that all the structural phases that are oriented on various directions can be easily recorded by X-ray RSMs.

2.3.4 Co-ordinate transformation in X-ray RSM

The full map of the scattered X-ray intensity around the reciprocal lattice point is known as a reciprocal lattice space mapping or "X-ray RSM" and this is straightforward of transformation of the reciprocal lattice units (hkl) into the angular co-ordinates (2θ and ω) via the X-ray wavelength. In fact, the recorded data of X-ray RSM obtained by the Bruker-AX8 D8 DISCOVER instrument gives the full map of the scattered intensity in the reciprocal lattice units. For instance, the full reciprocal

lattice space mapping of the c-InN sample shown in Figs. 2.4 a) and 2.5 a) is given in Fig. 2.8. This map shows a typical (002) X-ray RSM of the c-InN film on the GaAs (001) substrate measured along the [110] azimuth axis. As seen in Fig. 2.8, the horizontal axis (*hk*), which corresponds to the ω-axis, indicates off-axis planes of crystals. The vertical axis (*l*), which relates to the $2\theta/\omega$-axis, indicates on-axis planes. Note that the reciprocal lattice units used in the figure is the same as the reciprocal lattice index used for the GaAs crystal lattice.

To obtain the X-ray RSM plotted in the angular co-ordinates, transformation of the reciprocal lattice units (*hkl*) into the angular co-ordinates ($2\theta/\omega$ and ω) via the X-ray wavelength was done. According to Bragg's law and the lattice plane spacing (d_{hkl}) in the cubic crystal given in Eqs. 2.2 and 2.3, thus, the $2\theta/\omega$ angles can be expressed as:

$$2\theta = 2 \cdot \sin^{-1}\left(\frac{\lambda \cdot \sqrt{h^2 + k^2 + l^2}}{2 \cdot a_{GaAs}} \right),$$ (2.6)

where the lattice constant of the substrate is $a_{GaAs} = 5.653$ Å. For example, when (*hkl*) = (002), the value of $2\theta/\omega$ is calculated to be 31.63° corresponding to the (002) diffraction of GaAs.

On the other hand, the value of ω is a tilted angle measured with respect to the film surface. The inclination between the on-axis (002) and off-axis (*hkl*) planes in the cubic crystal lattice is shown in Fig. 2.9. The tilted angle between the (00*2*) plane and the (*hkl*) plane can be obtained from the scalar products of the <002> and <*hkl*> directions ($\vec{a} \cdot \vec{b} = |\vec{a}||\vec{b}|\cos\omega$). Thus, we have

$$\omega = \pm\cos^{-1}\left(\frac{l}{\sqrt{h^2 + k^2 + l^2}} \right),$$ (2.7)

Therefore, the $2\theta/\omega$ and ω angles for each (*hkl*) values can be calculated using Eqs. 2.6 and 2.7, respectively. For instance, for (*hkl*) = (0 0 2), (0.18 0.18 2.08) and (1 1 1) the values of ω were calculated to be 0°, 7° and 54.7°, respectively. Figure 2.10 shows the (002) X-ray RSM plotted in the angular co-ordinates ($2\theta/\omega$ and ω) of the
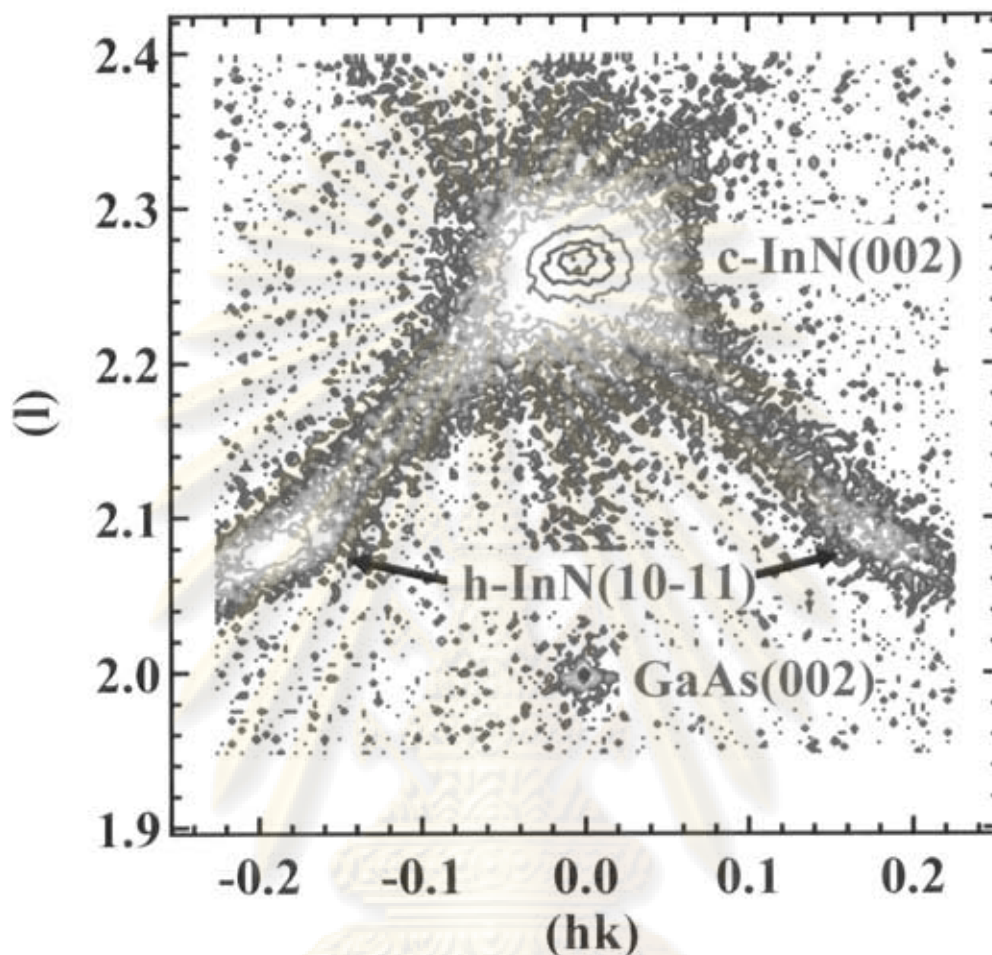
Figure 2.8 A typical X-ray RSM of the (002) c-InN diffraction peak of the c-InN sample shown in Figs. 2.4a and 2.5a, which was measured along the [110] azimuth axis by the Bruker-AX8 D8 DISCOVER instrument, plotted in the reciprocal lattice units, which is the reciprocal lattice of GaAs crystal. This also shows the (10-11) diffraction peaks of h-InN and the (002) diffraction peak of GaAs substrate.
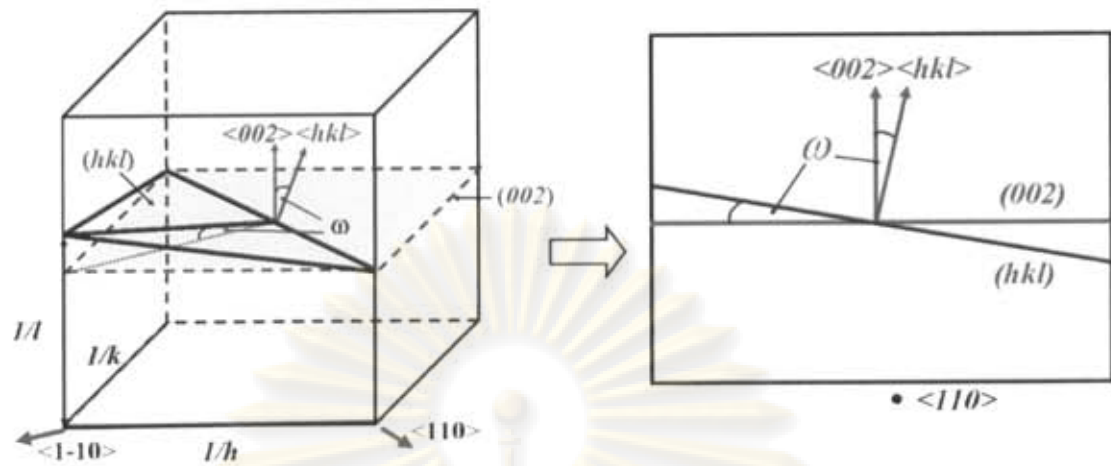
Figure 2.9: The angle difference (ω) between the on-axis (002) and off-axis (hkl) planes in the cubic crystal lattice for the <110> azimuth axis.
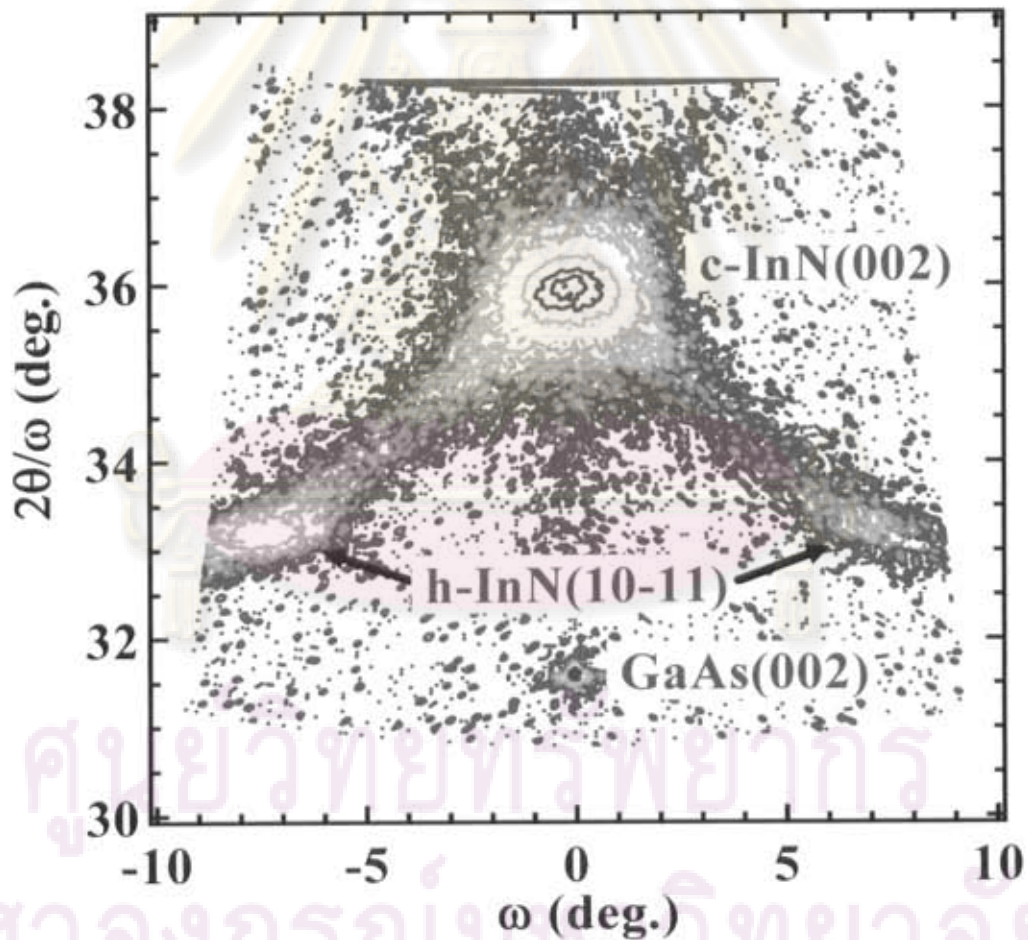
Figure 2.10: (002) X-ray RSM of the sample shown in Fig. 2.9 plotted in the angular coordinates. A rectangle shaped X-ray RSMs data in the reciprocal lattice units was transformed to be a trapezoidal-like shape in the angular co-ordinates.
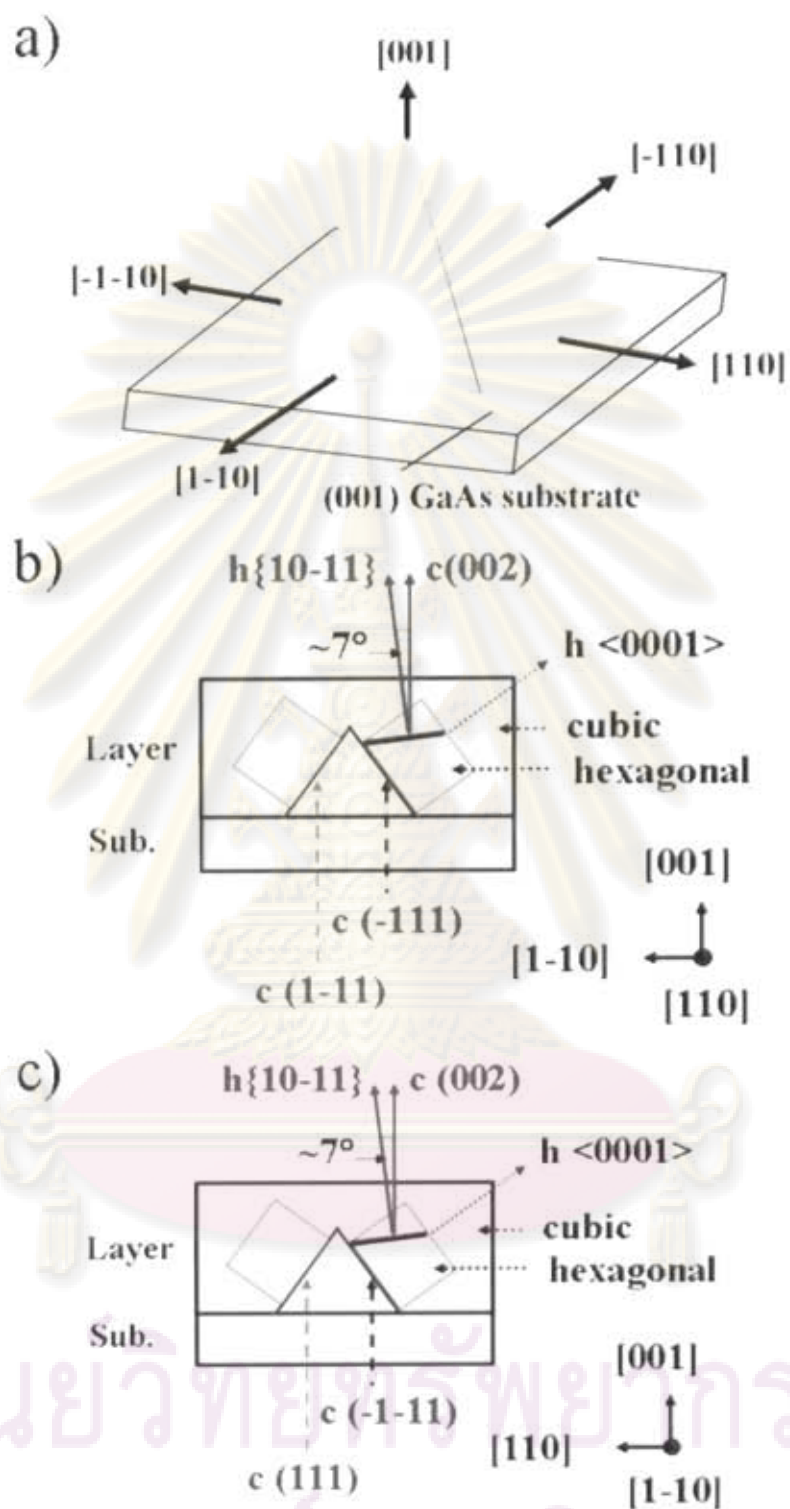
Figure 2.11: a) Schematic views of similar {111} planes in the cubic crystal and crystalline relationship between c-InN (002) and h-InN (10-11) for the b) [110] and c) [1-10] azimuth axes.

c-InN film on GaAs (001) substrate measured along the [110] azimuth axis. Note that that a rectangle-like shaped X-ray RSM data in the reciprocal lattice units was transformed to be a trapezoidal-like shape in the angular co-ordinates. Thus, we can now assign the peak positions in the $2\theta/\omega$ and ω positions. For $\omega = 0°$, the (002) diffraction peaks of c-InN and GaAs were clearly observed at $2\theta = 36.0°$ and $31.6°$, respectively. On the other hand, the (10-11) diffraction peaks of h-InN were observed at $2\theta = 33.2°$ and $\omega = \pm7°$, which are corresponded to the growth model presented in Figs. 2.6 c), 2.6 g) and 2.7 b).

Furthermore, it is well known that there are four similar {111} planes, as seen in Fig. 2.11 a), in the cubic structure [40]; (1-11) and (-111) planes along the [110] direction or azimuth axis (Fig. 2.11 b)), and (111) and (-1-11) planes along the [1-10] azimuth axis (Fig. 2.11 c)). In order to collect the diffraction peaks from all the hexagonal phase subdomains generated on these four similar {111} planes, X-ray RSMs measuring along both the [110] and [1-10] azimuth axes are found to be necessary.

2.4 Raman scattering

C. V. Raman was awarded the Nobel Prize in 1930 for his discovery of inelastic light scattering from molecules. The process which now carries his name refers to scattering from high frequency excitation such as vibrational modes of molecules. In the present context of phonon physics, it refers specifically to inelastic scattering from optical phonons. The process is identical to the inelastic scattering of X-rays and it is also similar to the inelastic scattering of neutrons by a crystal.

Inelastic light scattering can be subdivided into two types, Stokes scattering and anti-Stokes scattering. Stokes scattering corresponds to the emission of phonon, while anti-Stokes scattering corresponds to phonon absorption. The interaction shown in Figs. 2.12 a) and b) is Stokes and anti-Stokes process, respectively. Mostly Stokes scattering is used. Conservation of energy and momentum during the interaction requires that: $\omega = \omega_i \pm \omega_s$ and $\bar{k} = \bar{k}_i \pm \bar{k}_s$, where ω_i and $\bar{k}_i$ are frequency and wavevector of the incident photon, respectively. ω_s and $\bar{k}_s$ are frequency and wavevector of the scattered photon, respectively. The + signs correspond to phonon emission (Stokes scattering), while the − signs correspond to phonon absorption (anti-
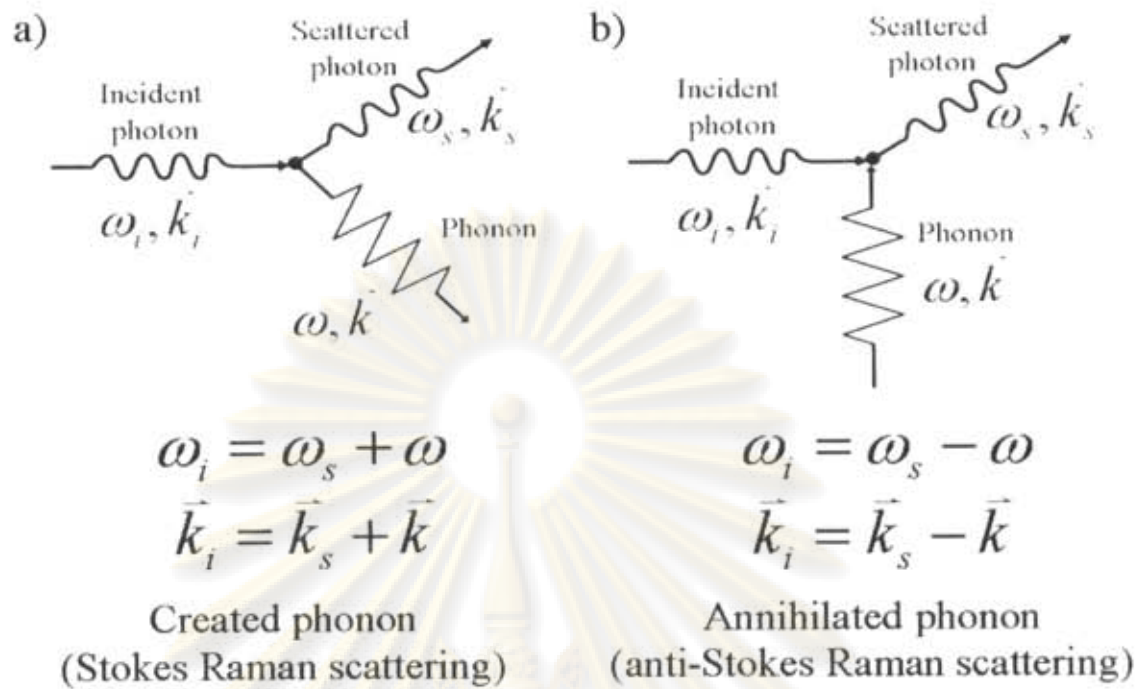
Figure 2.12: Schematic representation of Raman scattering of a photon with a) emission and b) absorption of a phonon [31].
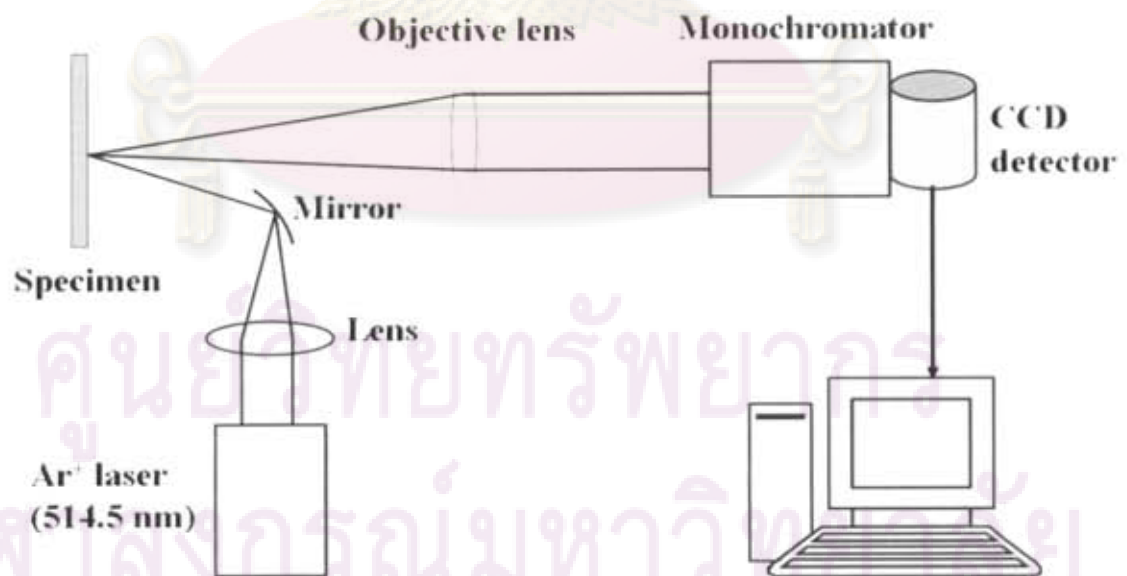
Figure 2.13: Schematic drawing of Raman scattering system.

Stokes scattering). Thus the light is shifted down in frequency during a Stokes process and up in frequency in the anti-Stokes process. The frequency of the phonons can be scattered photons is named as "Raman frequency" or "Raman shift". Thus the main use of inelastic light scattering is to measure phonon frequencies.

Raman scattering experiment requires a monochromatic light source, typically a laser, a spectrometer and a sensitive photon-counting detector such as a photo multiplier tube or a multi-channel charge couple device (CCD) [30]. Experimental apparatus used to record Raman spectra is shown in Fig. 2.13. The specimen is excited with a laser light, and the scattered photons are collected and focused into a monochromator. The signals are recorded using a sensitive photon-counting detector. Raman spectra are usually plotted in term of the intensity of the scattered photons versus the Raman shift in wave number unit (cm^{-1}), which is a standard for vibrational studies. Commonly, the unit of "cm^{-1}" is used to clarify the energy shift of the scattered photons. Raman shift of 1 cm^{-1}, for example, corresponds to the energy shift of ~1/8 meV [30].

The scattering geometry is commonly written as $\vec{k}_i(e_i,e_s)\vec{k}_s$, which is so called Portó notation [30]; where $\vec{k}_i$ and $\vec{k}_s$ are the directions of incident and scattered photons; e_i and e_s are the polarizations of incident and scattered photons, respectively. The simplest scattering geometry is the backscattering. From the conservation of wavevector, the wavevector $\vec{k}$ of the phonon must be along the [001] direction also for backscattering from a (001) surface of cubic crystal. The longitudinal optical (LO) phonon is polarized in the z direction (or [001] direction), while the transverse optical (TO) phonon is polarized in x-y plane (or (001) plane). Thus, the scattering geometries for backscattering from the (001) surface of cubic crystal are $z(x,y)\bar{z}$ or $z(y,x)\bar{z}$.

Recently, Raman spectroscopy has proved to be a power tool for the investigation of material properties such as doping concentration, crystal orientation and defect identifications etc. H. Yaguchi et al. [33] has used Raman spectroscopy to clarify the spatial distribution of the hexagonal and cubic phases in the GaN layers grown on 3C-SiC (001) substrates. In addition, X. L. Sun et al. [34] confirmed that the occurrence of optical phonon mode from hexagonal phase can be spectrally separated from the phonon mode of the cubic phase. Their results uniquely showed the presence of the hexagonal phase subdomain. In this study, Raman spectroscopy is
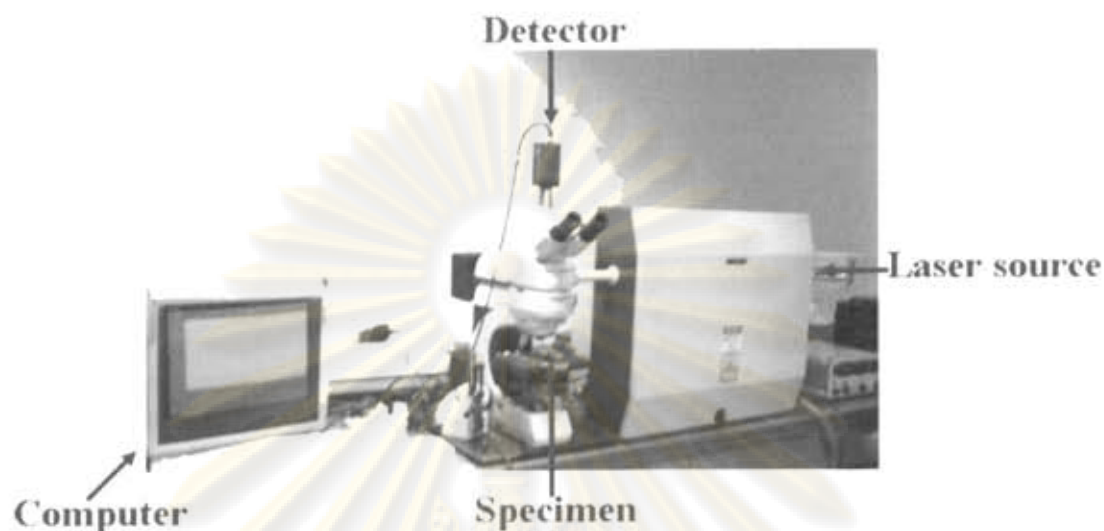
Figure 2.14: Raman spectroscopy system at the Gem and Jewelry Institute of Thailand (Public Organization), Chulalongkorn University.

Structural phases	Phonon frequencies (cm^{-1})			
	E_2 (high)	A_1 (LO)	TO	LO
h-InN	490[a]	590[a]	-	-
	488[b]	586[b]	-	-
	491[c]	590[c]	-	-
c-InN	-	-	472[a]	586[a]
	-	-	457[d]	588[d]
	-	-	467[e]	596[e]

Table 2.1: Phonon frequencies of InN crystals including both hexagonal and cubic crystal lattices.

[a] [45] G. Kaczmarczyk *et. al., Appl. Phys. Lett.* **76** (2000): 2122.
[b] [49] V. Yu *et. al., Appl. Phys. Lett.* **75** (1999): 3297.
[c] [43] Ming-Chin Lee *et. al., Appl. Phys. Lett.* **73** (1998): 2606.
[d] [44] A. Tabata *et. at.,Appl. Phys. Lett.* **74** (1999): 362.
[e] [11] Y. I wahashi *et. al., phys. stat. sol. (c)* **3** (2006): 1515.

used to clarify the spatial distribution of the hexagonal and cubic phases in the c-InN films grown by MBE. The expected results are summarized in Table 2.1. For c-InN, the frequency of the optical phonon is spit into LO and TO components [42] associated with the incident photons. On the other hand, for h-InN, the LO and TO phonons are represented as the A_1 and E_2 phonons, respectively.

In this study, the Raman scattering measurements were carried out at room temperature using the Renishaw Ramanscope RM1000 at the Gem and Jewelry Institute of Thailand (Public Organization), Chulalongkorn University. Figure 2.14 shows the Raman spectroscopy system. A 514.5-nm line of an Ar$^+$ laser is used as a monochromatic high frequency light source. The optical penetration depth, skin depth, ($d = 1/2\alpha$; where α is the absorption coefficient of InN) is estimated to be about 70 nm [32]. The laser beam is focused on the sample with the spot size of ~ 2 µm. The Raman spectra were obtained in the backscattering geometry $z(x, y)\bar{z}$ and recorded in the range of 250-800 wave number (cm^{-1}).

CHAPTER III

EFFECT OF GROWTH CONDITIONS

In this chapter, we focus on the effect of growth conditions, namely In- and N-rich growth conditions on the structural modification of the c-InN film on GaAs (001) substrates. First of all, the growth identification of In- and N-rich conditions is discussed. The crystal qualities and crystal defect information in the grown films at different growth conditions are compared. Moreover, the possible impact of the In- and N-rich growth conditions on the hexagonal phase generation and vibrational properties of the c-InN films were evaluated by HRXRD and Raman spectroscopy. Finally, we report that the ratio of cubic to hexagonal components in the c-InN layers grown on the GaAs (001) substrates can be estimated from the ratio of the integrated X-ray diffraction intensities of the cubic (002) and hexagonal (10-11) planes measured by the ω-scan, as far as the h-InN is grown with the <0001> axes parallel to the cubic <111> directions.

3.1 Sample descriptions

The series of the c-InN films in this study were grown on GaAs (001) substrates with a GaAs buffer layer grown by molecular beam epitaxy (MBE)[a] [12] at Department of Advanced Materials Science, The University of Tokyo, Japan. Sample structure is shown schematically in Fig. 3.1. A standard MBE source provided the In flux. A radio-frequency (rf) plasma source was used to produce an active N flux. The growth temperature was varied in the range of 450-490°C. The In flux and rf power

---

[a] Molecular beam epitaxy (MBE) is a sophisticated from evaporation in ultra high vacuum. It is the oriented overgrowth, i.e. the growth of one crystal on another in a single, well defined and related orientation. Using a single crystal substrate and correct epitaxial growth conditions, therefore, a monocrystalline deposit can be obtained [50].

c-InN layer (400 nm)
GaAs buffer layer (200 nm)
GaAs (001) substrate
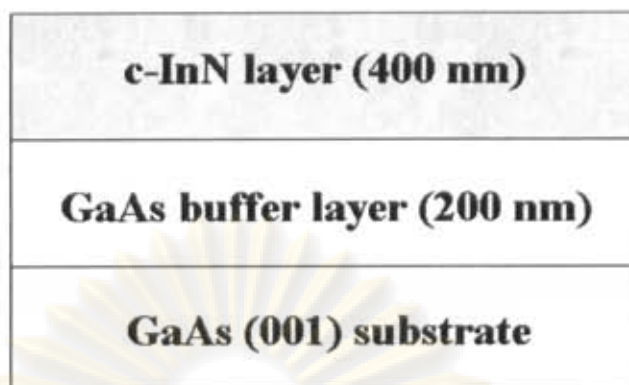
Figure 3.1: Schematic illustration of c-InN film grown on GaAs (001) substrate.

were kept constant at 1.5×10^{-4} Pa and 300 W, respectively. To change the V/III ratio, the supplied N_2 flow rate was varied in the range of 1.50-2.25 standard cubic centimeters per minute (sccm). According to these growth conditions, it is found that the In- and N-rich growth conditions can be controlled by the growth temperature and the supplied N_2 flow rate as well as the V/III ratio. The film thickness was estimated to be 400 nm for the growth time of 1 hour.

3.2 Identifications of growth conditions

The key issue to identify the growth condition is the In droplet [12], which can be seen on the surface for lower supplied N_2 flow rate and higher growth temperatures as shown in Fig. 3.2 (samples A, B and C). An appearance of the In droplets indicates an insufficient V/III ratio, resulting in the In-rich growth condition. On the other hand, the In-droplet-free surface reflects that the growing surface is under the N-rich growth condition as also seen in Fig. 3.2 (samples D, E and F). In addition, we evaluated an impact of the In- and N-rich growth conditions on the size of the grains in these films. Figure 3.3 shows AFM plan-view images of the films grown at different growth temperatures and supplied N_2 flow rates. The condition for the surface-stoichiometry is designated by the bolded line [12]. As shown in Fig. 3.3, it is clearly seen that the In- and N-rich growth conditions strongly effect on the size of the grains. For the In-rich growth condition, the surface root mean square (RMS) roughness of the films increases with decreasing growth temperature. In contrast, for the N-rich growth condition, the surface RMS roughness of the films increases with increasing growth temperature. The results suggest that, unlike the N-rich growth condition, the
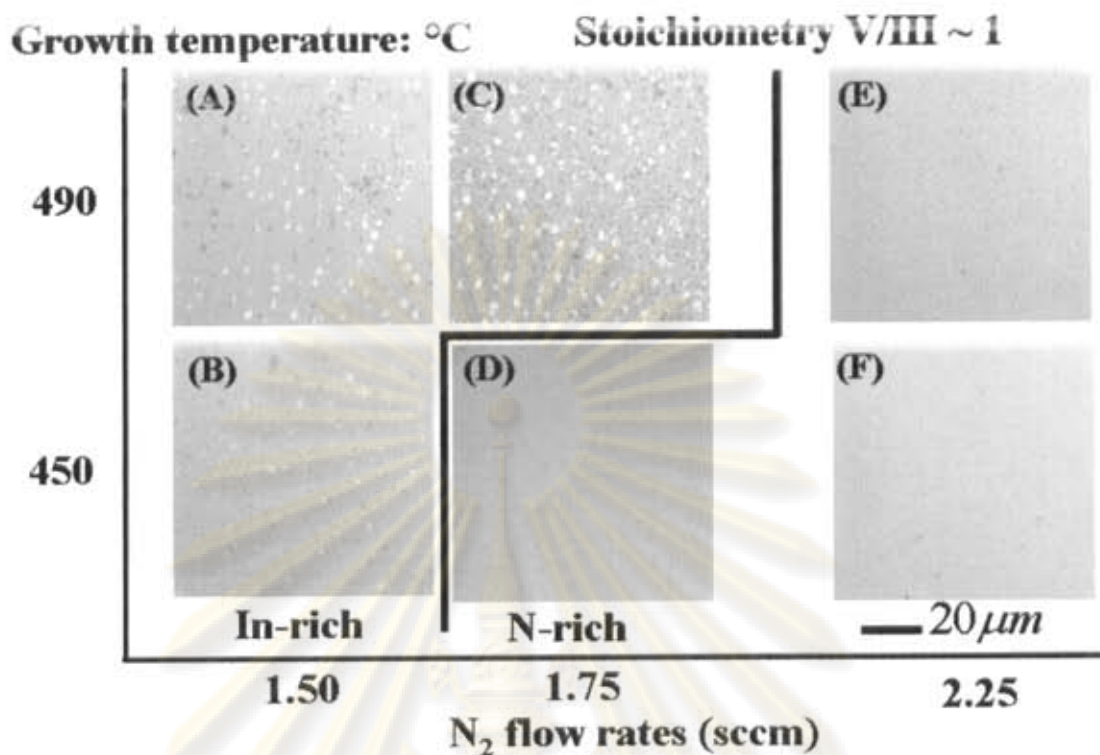
Figure 3.2: SEM images of the c-InN films grown at different growth temperatures and supplied N_2 flow rates. White spots in samples A, B and C indicate the In droplets.
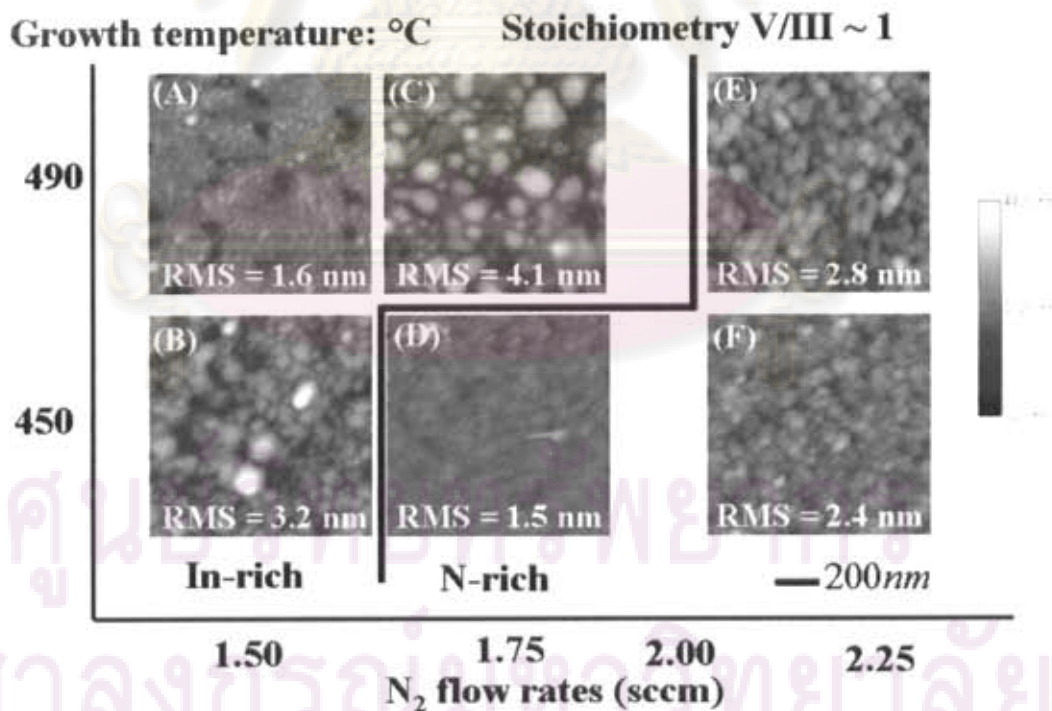
Figure 3.3: AFM images of the c-InN films grown at different growth temperatures and supplied N_2 flow rates.

formation of grains in the c-InN films grown under the In-rich growth condition is caused by limited surface diffusion processes due to the insufficient V/III ratio.

3.3 Crystal quality of the c-InN grown films

All samples were investigated by HRXRD in order to determine the perpendicular lattice constant ($a_\perp$) and check the crystalline qualities. Figure 3.4 a) shows the (002) $2\theta/\omega$-scan profiles of the c-InN films on GaAs (001) substrates grown under In- (blue solid lines) and N- (red dotted lines) rich growth conditions. The cubic (002) diffractions are clearly observed about $2\theta = 36°$, whereas the hexagonal (0002) and (10-11) diffractions are absent. This clearly demonstrates that all the InN grown films have cubic structures and no hexagonal (0002) and (10-11) grains parallel to the GaAs (001) substrate. However, it cannot be concluded that no generation of hexagonal crystal in these c-InN films as described in Chapter II.

From the separation between the (002) diffraction peaks of c-InN and GaAs, the average value of perpendicular lattice constant of the c-InN film was calculated to be $a_\perp \sim 4.99$ Å with standard deviation of 0.02 Å. The calculated value of $a_\perp$ is in good agreement with theoretical calculated of 4.98 Å [41]. Full width at half maximum (FWHM) of the (002) reflections obtained from $2\theta/\omega$- (Fig. 3.4 a)) and ω-scan curves (Fig. 3.4 b)) for the c-InN films grown under the In-rich condition (blue solid lines) are narrower than that for the films grown under the N-rich condition (red dotted lines). These indicate that both lattices fluctuation and mosaicity in the c-InN films grown under In-rich condition is lower than that of the films under N-rich condition. The narrowest FWHM of ω-scan is around 36 min for the film grown at 490°C with supplied N_2 flow rate of 1.75 sccm. Consequently, the c-InN films with higher crystal quality can be achieved under the In-rich growth condition.

3.4 Correlation between vibrational properties and structural modification

In this part, we evaluated the possible impact of the In- and N-rich growth conditions on the vibrational properties in the c-InN films using Raman spectroscopy.
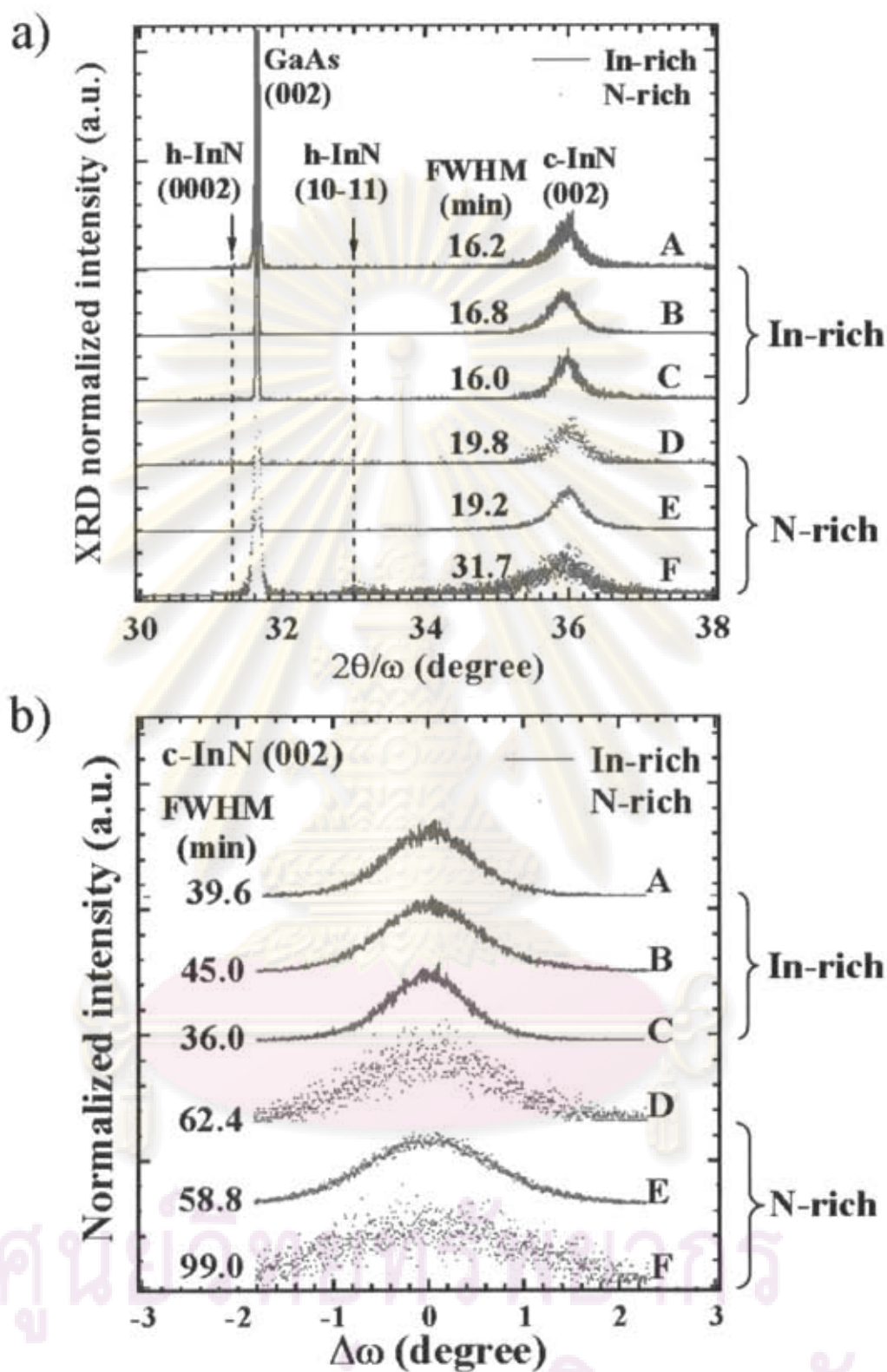
Figure 3.4: (a) (002) $2\theta/\omega$ -scan profiles and (b) (002) ω -scan profiles of the corresponding c-InN films grown on GaAs (001) substrates.
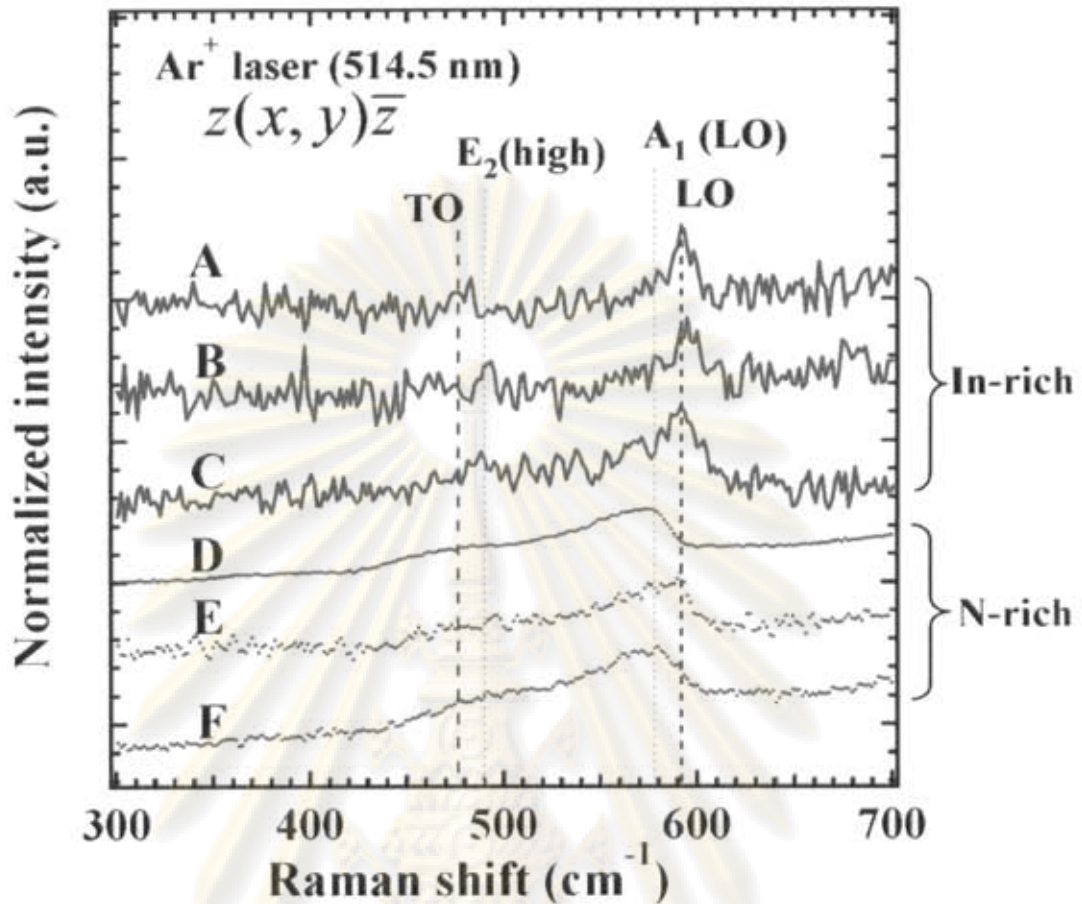
Figure 3.5: Raman spectra of the c-InN films grown under In-(blue solid curves) and N-(red-dotted curves) rich growth conditions. Black-dashed lines and green-dotted lines indicate the characteristic phonon frequencies of c-InN and h-InN phases, respectively.

Figure 3.5 shows Raman spectra of the c-InN films on GaAs substrates grown under In-(blue solid curves) and N-(red dotted curves) rich growth conditions. The black-dashed and green-dotted lines indicate the characteristic phonon frequencies of cubic [45] and hexagonal [49] structures of the InN crystals, respectively. For reference, values of these characteristic phonon frequencies for both cubic and hexagonal InN crystals have already presented in Table 2.1. It is found that the cubic LO phonon is clearly observed in the c-InN films grown under the In-rich growth condition (samples A, B and C). On the other hand, the c-InN films grown under the N-rich growth condition (samples D, E and F), Raman spectra exhibit a mixture of cubic and hexagonal phonon modes. For these films, the A_1 (LO) mode shows broadening and its wide band covering from 550-600 cm^{-1}. In fact, the phonon mode broadening is

attributed to structural disorder-activated scattering as that observed in other III-N semiconductors [34]. The results demonstrate that the difference in the Raman spectra is in connection with the different amounts of hexagonal phase inclusion in the c-InN films. Based on $2\theta/\omega$ HRXRD and Raman scattering measurements, the grown c-InN layers also contain some amount of inclined hexagonal subdomains. Under these observations, thus, HRXRD measurements of off-axis planes as well as on-axis planes are found to be necessary, for complete characterization of structural phases in c-InN layers.

3.5 Detection of inclined hexagonal-phase subdomains

In order to detect the inclined hexagonal-phase subdomains in the c-InN films, X-ray RSMs were performed. Figure 3.6 shows the X-ray RSMs around the (002) diffraction point measured along the [110] azimuth axis for the c-InN films grown under the In-rich growth condition (sample A, at 490°C with the N$_2$ flow rates of 1.50 sccm) and the N-rich growth condition (sample F, at 450°C with the N$_2$ flow rates of 2.25 sccm). The related diffractions from different planes are labeled in the figure. Beside the (002) diffraction peak of GaAs substrate, the cubic (002) and hexagonal (10-11) peaks of InN are clearly seen. The tilted angles between the cubic (002) and hexagonal (10-11) reflections in the c-InN layers are about $\pm7^{\circ}$. This result indicates that the c-InN layers are found to contain some amount of inclined hexagonal-phase subdomains. The intensity of h-InN being smaller than that of sample F suggests a lower amount of the inclined hexagonal-phase subdomains in sample A. The hexagonal (10-11) peaks as seen in Fig. 3.6 are analyzed as that the hexagonal phase presented in the c-InN layer is mainly generated on the cubic (111) surfaces, which is shown schematically in Fig. 2.11. The orientation of the hexagonal-phase subdomains are in the direction of [0001]//[111].

In addition, the shape characteristic of the hexagonal (10-11) peaks can be clarified. It is clearly seen in Fig. 3.6 that there is a streak connecting the c-InN (002) reciprocal lattice point to the h-InN (10-11) points. This diffraction pattern indicates that there are a few hexagonal-phase subdomains with different lattice constant and crystal orientation. Since, the atomic arrangement of hexagonal (0001) surfaces is the
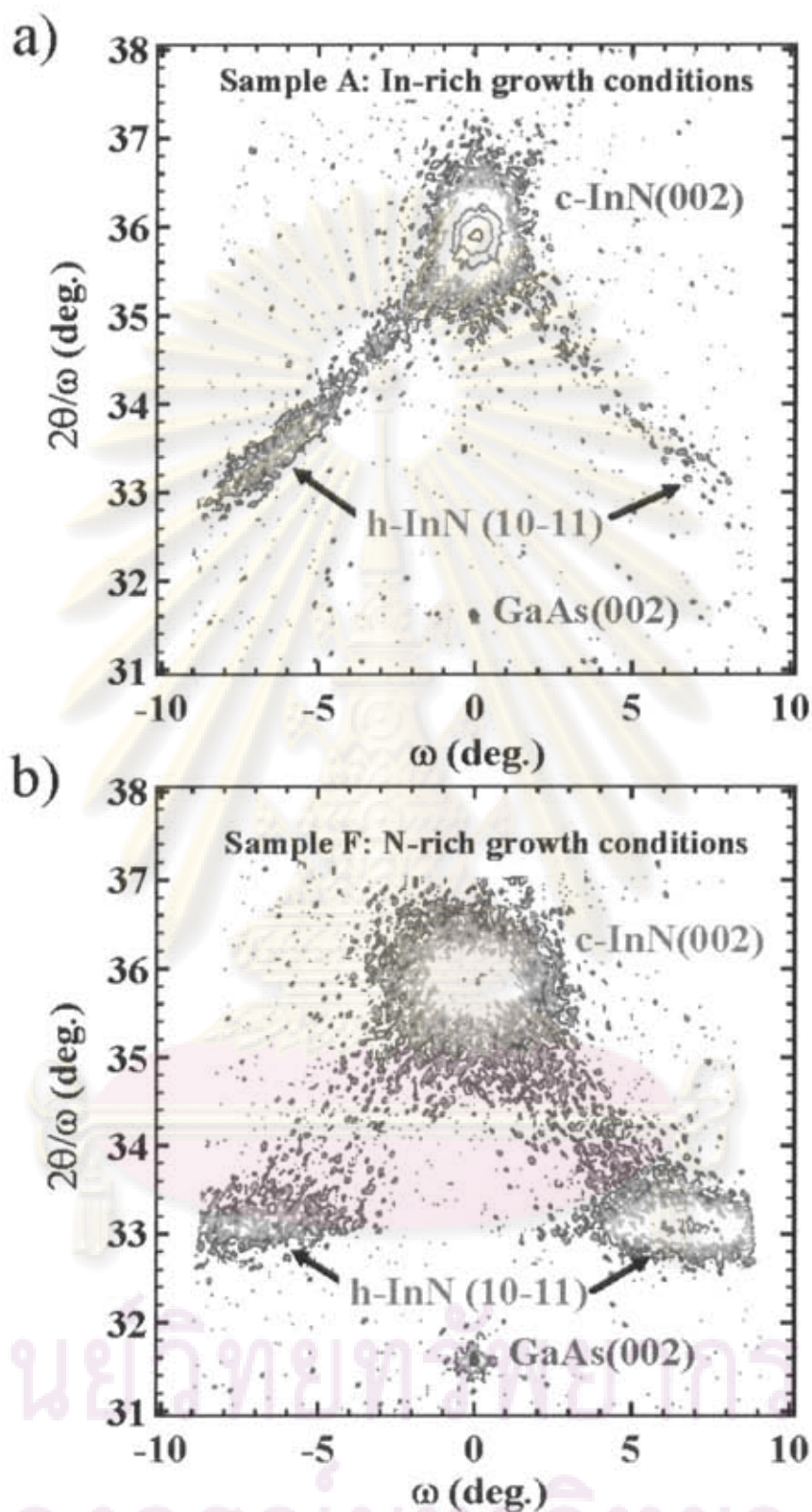
Figure 3.6: Typical (002) X-ray reciprocal space mappings of the InN films on GaAs (001) substrates grown under the In-rich growth condition (sample A, at 490°C with the N₂ flow rates of 1.50 sccm) and the N-rich growth condition (sample F, at 450°C with the N₂ flow rates of 2.25 sccm) measured along the |1-10| azimuth axis.

same as those of the cubic (111) surfaces. For this reason, there are three possible ways to interpret the structural modifications of c-InN along the <111> directions [24].

1. The streak consists of (10-11) diffraction peaks of h-InN with different lattice constants. The hexagonal phase-subdomains may mosaic in c-InN layers. The strain relaxation in h-InN domain will vary with the size of h-InN domain. Therefore, the lattice constant and crystal orientation would change with the size of h-InN subdomain. For smaller h-InN subdomains, the lattice constant and crystal orientation will be close to those of c-InN. For larger h-InN domains, they will approach to those of h-InN.

2. The domain boundaries between h-InN and c-InN are deformed regions with its crystalline structure changing gradually from cubic to hexagonal structures, namely stacking faults.

3. The layer may contain layer-like c-InN/h-InN material. From this reasons, we conclude that the average lattice plane spacings would vary from c-InN to that of h-InN due to the different amounts of hexagonal phase inclusion.

3.6 Estimation of hexagonal phase inclusion

For the N-rich growth condition, the intensity of the h-InN (10-11) reflections is larger than that of the In-rich growth condition, suggesting higher hexagonal phase generation in the c-InN film. In order to give a quantitative estimation of an amount of hexagonal phase inclusion, we calculated the integrated XRD intensities of the cubic (002) and hexagonal (10-11) diffractions measured by the ω-scan with structure factor $F(hkl)$. Figures 3.7 and 3.8 show the ω-scan profiles of c-InN (002) planes ($2\theta = 35.9°$) and h-InN (10-11) planes ($2\theta = 33.2°$) of sample A and sample F, respectively. The red circles and solid lines are the experimental and the Gaussian fitted curves, respectively. The integration data of each diffraction peaks was calculated from area under the Gaussian fitted curves as shown in Figs. 3.7 and 3.8. The FWHMs of the c-InN (002) reflections indicated in Figs. 3.7 a) – b) and Figs. 3.8 a) – b) show that the crystalline quality of sample A is better than that of sample F. Since, the value of FWHM in the ω-scan mode refers to the variation of crystal orientation, as described in Chapter II.

It has been well known that XRD peak intensities are usually different for
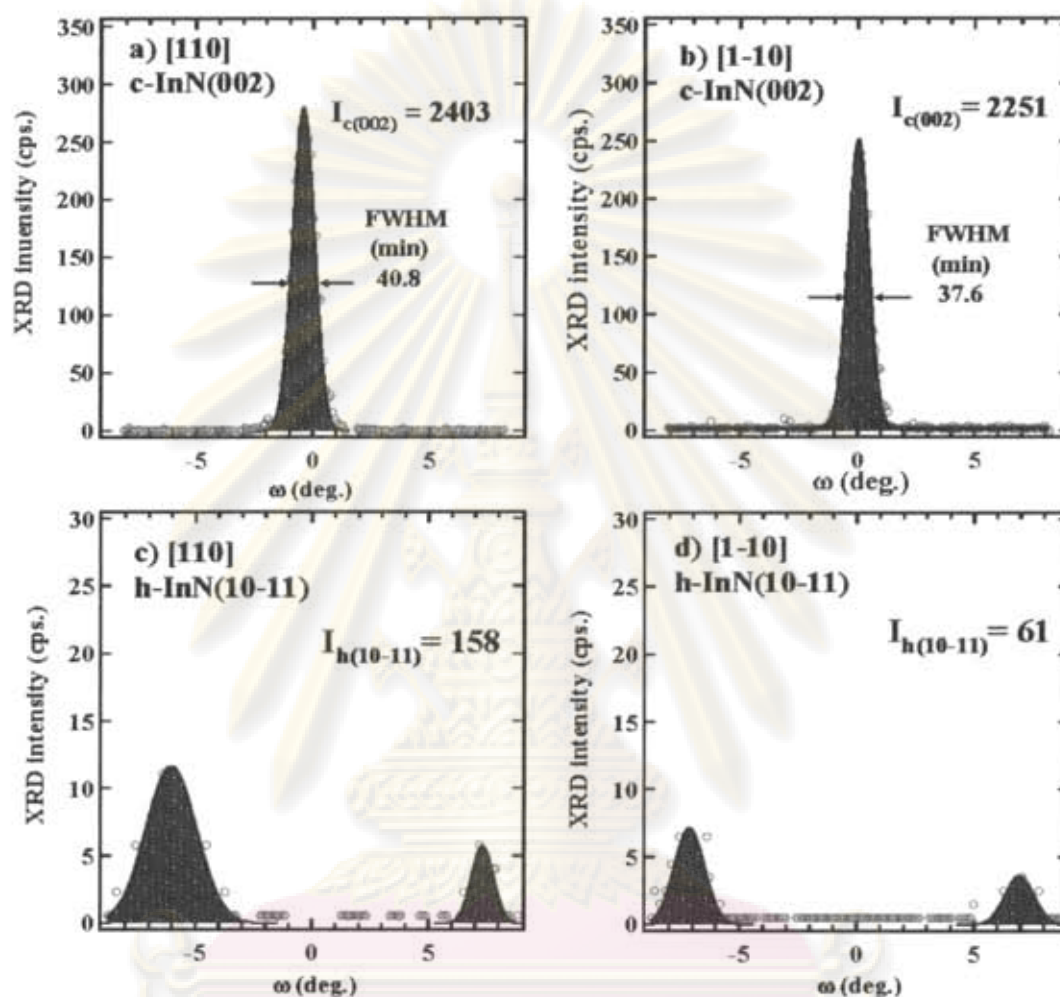
Figure 3.7: ω-scan profiles of the c-InN (002) ($2\theta = 35.9°$) and h-InN (10-11) ($2\theta = 33.2°$) diffraction peaks extracted from the X-ray RSM measured along the [110] and [1-10] azimuth axes of sample A. The red circles and solid lines are the experimental and the Gaussian fitted curves, respectively. The integration data of each diffraction peaks was calculated from the area under the Gaussian fitted curves.
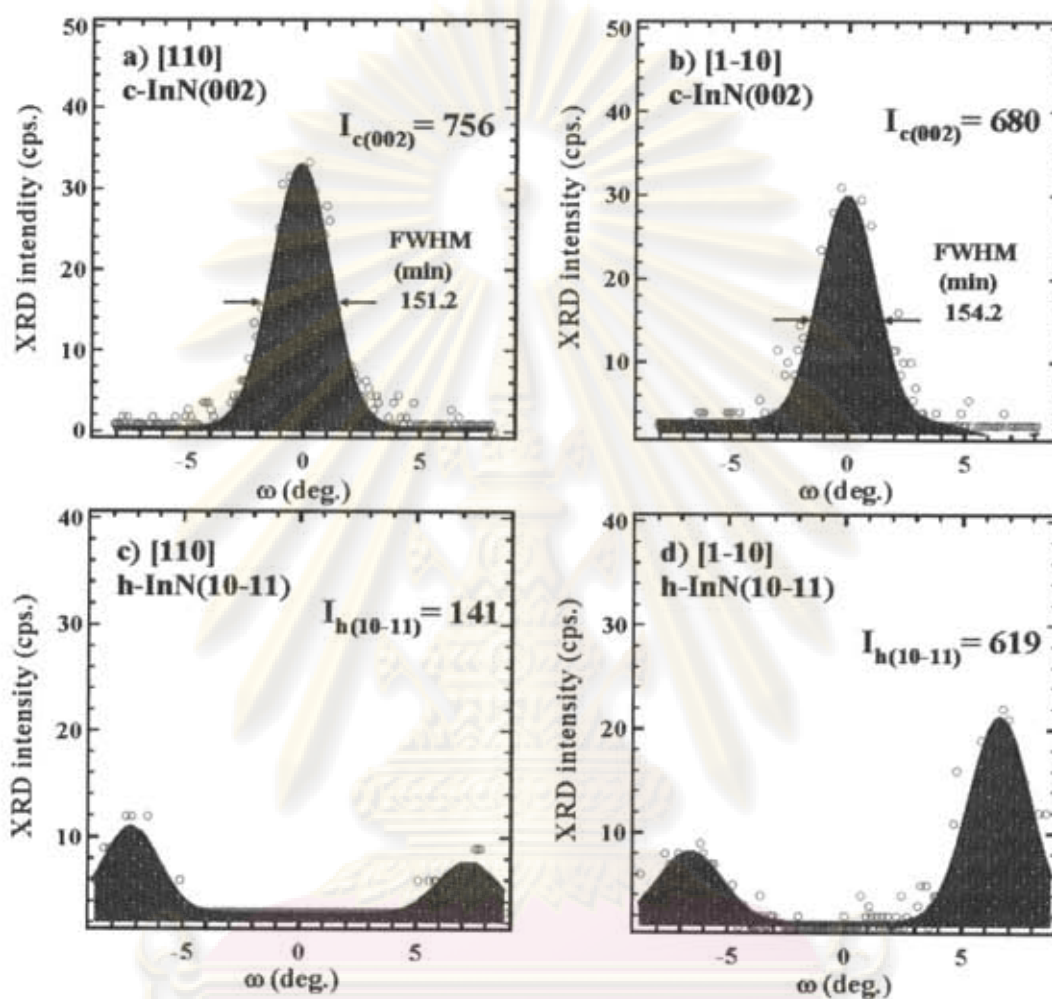
Figure 3.8: ω-scan profiles of the c-InN (002) ($2\theta = 35.9°$) and h-InN (10-11) ($2\theta = 33.2°$) diffraction peaks extracted from the X-ray RSM measured along the [110] and [1-10] azimuth axes of sample F. The red circles and solid lines are the experimental and the Gaussian fitted curves, respectively. The integration data of each diffraction peaks was calculated from the area under the Gaussian fitted curves.

different lattice planes [48]. However, there is no report on the XRD intensity of c-InN compared with that of h-InN, owing to a lack of a high quality thick c-InN layer. Thus, we calculated the theoretical integrated XRD intensities of the ω-scan for both the c-InN (002) and h-InN (10-11) planes. The integrated XRD intensity I is expressed as [36]:

$$I = I_0 \times |F(hkl)|^2 \times P \times V \times L_p \times N^2 \times e^{-2M} ,$$ (3.1)

where I_0, P, V, L_p, N and e^{-2M} are the incident X-ray intensity, multiplicity factor, irradiated volume, Lorentz polarization factor, number of unit cell per unit volume and temperature factor, respectively.

If there are N atoms in unit cell, the coordinates of the n-th atom are defined as (x_n, y_n, z_n) and f_n is the atomic scattering factor for the n-th atom, then structure factor F (hkl) can be expressed as

$$F_{hkl} = \sum_{n=1}^{N} f_n \exp[2\pi i(hx_n + ky_n + lz_n)] ,$$ (3. 2)

The value of f_n, which is corresponded to scattering strength of n-th atom, depends on both θ and λ of incident X-ray beam [28]. Table 3.1 shows atomic scattering factors of In, Ga and N atoms [37], which are used in our calculation. For low scattering angles, the atomic scattering factor can be seen to reach values close to the atomic number as seen in Fig. 3.9. According to the coordinate of all the atoms, the structure factor can be calculated. In the case of epitaxial layer, P = 1. The Lorentz polarization factor can be denoted as

$$L_p = \frac{1 + \cos^2 2\theta}{\sin^2 \theta \cos \theta} ,$$ (3.3)

where θ is being the Bragg's angle of the (hkl) reflection. In addition, as the temperature of the crystal is increased, the intensity of the Bragg reflected X-ray decreases as an exponential decay. This is so called temperature factor. Derby and Waller showed that the temperature factor depends on Boltzmann constant (k_B),

sinθ/λ	Atomic scattering factor [f (sinθ/λ)]										
(Å^{-1})	0.0	0.1	0.2	0.3	0.4	0.5	0.6	0.7	0.8	0.9	1.0
In	49	44.7	38.6	33	28.1	25	22.4	20.1	18	16.2	14.7
Ga	31	27.8	23.3	19.3	16.5	14.5	12.7	11.2	10	8.9	7.9
N	7	5.8	4.2	3	2.3	1.9	1.65	1.54	1.49	1.36	1.29

Table 3.1: Atomic scattering factors for In, Ga and N atoms, which used in our calculation [37].
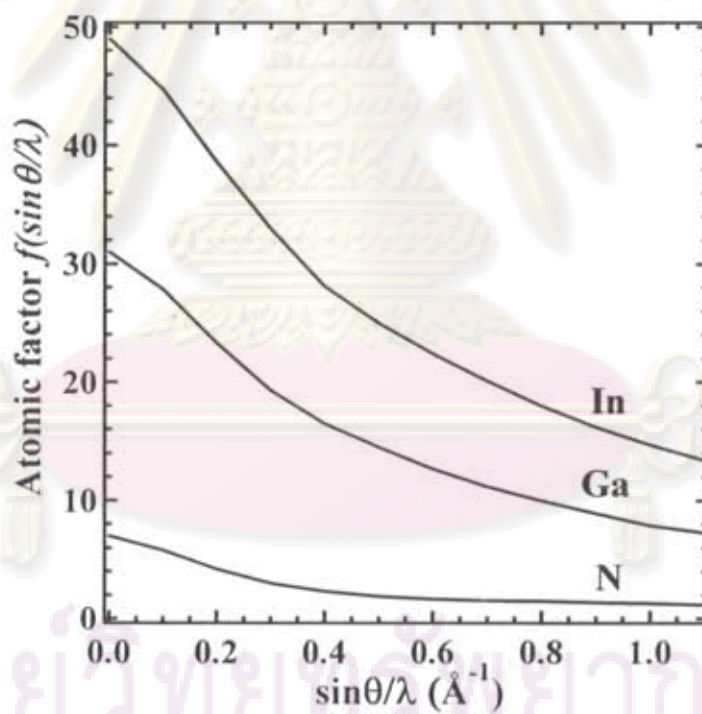
Figure 3.9: Atomic scattering factors for In, Ga and N atoms as a function of $\sin\theta / \lambda$.

temperature (T), mass of an atom (M), lattice phonon frequency (ω) and reciprocal lattice vector ($\vec{G}$, where $|\vec{G}| = 1/d_{hkl} = \sin\theta/\lambda$) and it can be denoted as the follow [39]

$$e^{-2M} = \exp\left(-\frac{k_B T}{M\omega^2} G^2\right), \qquad (3.4)$$

The exponential factor "$2M$" is so called Debye-Waller factor.

As a result, the calculation values of the relative XRD intensities from one plane for several InN planes are shown in Table 3.2. To compare with the calculated results from ref. [36], in addition, the integrated XRD intensities from one plane for several planes of GaN were also calculated as listed in Table 3.2. It was found that the integrated XRD intensity from hexagonal (10-11) plane was nearly equal to that from the cubic (002) plane. The α values, which are the ratio of the integrated XRD intensity from the summation of those from the hexagonal (10-11) planes to the cubic (002) plane, were calculated to be 1.01 and 1.07 for InN and GaN, respectively.

To estimate the amount of hexagonal phase inclusion in the c-InN layer, Eq. 3.1 is simplified. Thus, the irradiated volume is

$$V = \frac{I}{I_0 \times |F(hkl)|^2 \times P \times L_P \times N^2 \times e^{-2M}}, \qquad (3.5)$$

So, the volume ratio of hexagonal phase to cubic phase can be expressed as

$$\frac{V_h}{V_c} = \frac{I_h}{I_c} \frac{I_{0-c} \times |F(hkl)|_c^2 \times P_c \times L_{P-c} \times N_c^2 \times e_c^{-2M}}{I_{0-h} \times |F(hkl)|_h^2 \times P_h \times L_{P-h} \times N_h^2 \times e_h^{-2M}}, \qquad (3.6)$$

where h and c denote hexagonal and cubic phase structures, respectively. Finally, the amount of hexagonal phase inclusion in the total volume, $(V_h)_T$, can be calculated using

$$(V_h)_T\% = \frac{V_h/V_c}{1 + V_h/V_c} \times 100\% = \frac{I_h}{I_h + \alpha I_c} \times 100\%, \qquad (3.7)$$

Crystals	Structures	Planes	θ (deg.)	I (10^6 cps.)	$I/I_{c\text{-}002}=$ α	Ref. [36] α
InN	Cubic	(111)	15.53	5.18	1.93	
		(002)	18.01	2.68	1.00	
		(220)	25.93	1.28	0.48	
		(311)	30.85	0.62	0.23	
	Hexagonal	(10-10)	14.55	1.91	0.72	
		(0002)	15.62	5.11	1.90	
		(10-11)	16.56	2.72	1.01	
		(10-12)	21.60	0.49	0.18	
GaN	Cubic	(111)	17.16	19.77	2.35	2.35
		(002)	19.92	8.41	1.00	1.00
		(220)	28.81	4.51	0.54	0.61
		(311)	34.40	1.98	0.24	0.26
	Hexagonal	(10-10)	16.19	8.19	0.98	0.95
		(0002)	17.28	19.87	2.35	2.32
		(10-11)	18.42	8.97	1.07	1.06
		(10-12)	24.04	1.76	0.21	0.20

Table 3.2: Theoretical XRD intensities from several cubic and hexagonal planes for both the InN and GaN crystals.

where α is the weight number. I_h and $\bar{I}_c$ are the integrated XRD intensities from hexagonal (10-11) planes and the averaged integrated XRD intensities from cubic (002) planes, respectively. In our work, we use the value of $\alpha = 1.01$ for the InN crystal, thus, Eq. 3.7 becomes:

$$(V_h)_T\% = \frac{I_h}{I_h + 1.01\bar{I}_c} \times 100\% , \tag{3.8}$$

From Eq. 3.8, we demonstrate that the amount of hexagonal phase inclusion in the c-InN layer can be estimated using the ratio of integrated XRD intensity from the cubic

Samples	Growth Temperature (°C)	N₂ flow rate (sccm)	Growth conditions	h-phase inclusion [c-phase purity] (%)
A	490	1.50	In-rich	8 [92]
B	450	1.50	In-rich	12 [88]
C	490	1.75	In-rich	17 [83]
D	450	1.75	N-rich	22 [78]
E	490	2.25	N-rich	25 [75]
F	450	2.25	N-rich	52 [48]

Table 3.3: Amounts of hexagonal phase inclusion in the c-InN films on GaAs substrates grown under the In- and N-rich growth conditions with various temperatures and N₂ flow rates.

(002) plane to the summation of those from the hexagonal (10-11) planes measured by ω-scan. Then, Eq. 3.8 was used to estimate the volume ratio of cubic to hexagonal phase, namely hexagonal phase inclusion.

Dependence on the growth conditions, specifically In- and N-rich growth conditions, was investigated. Table 3.3 summarizes the amounts of hexagonal phase inclusion as well as the cubic phase purity of the c-InN film grown under In- (samples A, B and C) and N- (samples D, E and F) rich growth conditions. From these results, it was found that the amount of hexagonal phase inclusion in the c-InN layers greatly depends on the growth conditions. The c-InN films grown under the N-rich growth condition exhibited higher incorporation of h-InN. On the other hand, the In-rich growth condition gives the c-InN films with higher cubic phase purity. The lowest amount of hexagonal phase inclusion is calculated to be 8%, which was obtained for the c-InN film grown under the In-rich growth condition (sample A, at 490°C with supplied N₂ flow rate of 1.50 sccm). Our results confirmed that under the In-rich growth conditions, it was found that a cubic dominant InN layers can be grown on GaAs (001) substrates.

3.7 Summary

The effects of the In- and N-rich growth conditions on crystal quality and structural modifications of c-InN films on GaAs (001) substrates grown by RF-MBE were investigated using various investigation techniques. The results concerning the crystal structures of c-InN layers on GaAs (001) substrate are summarized as following:

(1) The InN grown layer has a cubic structure (c-InN) with an epitaxial orientation relationship with the GaAs (001) substrate.

(2) Based on $2\theta / \omega$ scan, the perpendicular lattice constant of c-InN layer was calculated to be $a_\perp \sim 4.99$ Å, which is almost strain-relieved.

(3) The hexagonal phase in the c-InN layer is mainly generated on the (111) planes as a formation of stacking faults, hexagonal-phase subdomains as well as a layer-like c-InN/h-InN material.

(4) For the c-InN films grown under the N-rich growth condition, the films with the flatter surface, higher grain-sizes uniformity and lower cubic phase purity (48%) were obtained. On the other hand, for the In-rich growth condition, the c-InN films with higher crystal quality and cubic phase purity as high as 92% were achieved.

These results suggest that the In-rich growth condition plays a critical role in the growth of single structural-phase c-InN with higher crystalline quality.

ศูนย์วิทยทรัพยากร
จุฬาลงกรณ์มหาวิทยาลัย

CHAPTER IV

EFFECTS OF THE BUFFER LAYER

In this chapter, the structural properties of c-InN films grown on MgO substrates with a c-GaN buffer layer under the In-rich growth condition by RF-MBE were analyzed by HRXRD and Raman spectroscopy. The effects of the hexagonal phase inclusion in the c-GaN buffer layer on crystal quality and hexagonal phase generation in the c-InN films are described. Finally, the influence of hexagonal phase inclusion on vibrational properties in the c-InN films is also discussed.

4.1 Sample descriptions

The c-InN films presented here were grown on MgO (001) substrates by RF-MBE with a c-GaN buffer layer [11]. All samples were grown at Saitama University, Japan. Prior to the growth of c-InN epilayer, c-GaN buffer layer with a thickness of 400 nm were grown on MgO (001) substrate at 700°C. After the growth of c-GaN buffer layer, c-InN film was grown for 1 hour at 300-550°C with various In fluxes. The details of sample structure are shown schematically in Fig. 4.1.

4.2 Crystal quality of c-InN grown films

Figure 4.2 shows a typical (002) $2\theta/\omega$-scan profile of the c-InN film with the lowest amount of hexagonal phase inclusion grown on MgO (001) substrate with a c-GaN buffer layer. As seen in Fig. 4.2, the diffraction peaks corresponding to cubic (002) in both c-GaN buffer and c-InN layers were clearly observed. This indicates that the grown film and the buffer layer have a cubic structure. The perpendicular lattice constant of c-InN was calculated to be 5.01 Å, which is larger than previously
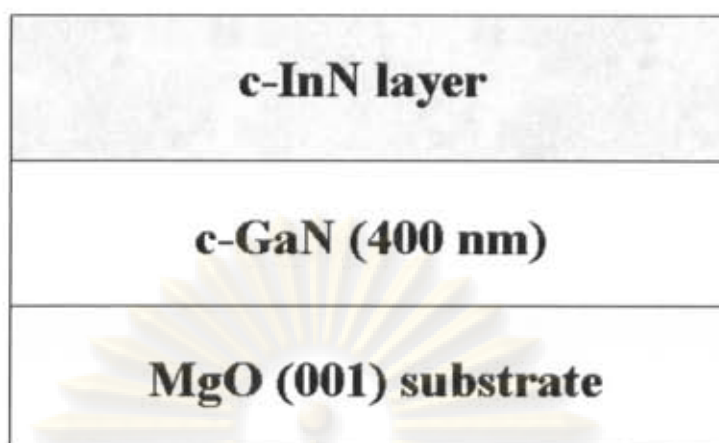
Figure 4.1: Schematic illustration of c-InN film grown on MgO (001) substrate with a c-GaN buffer layer.
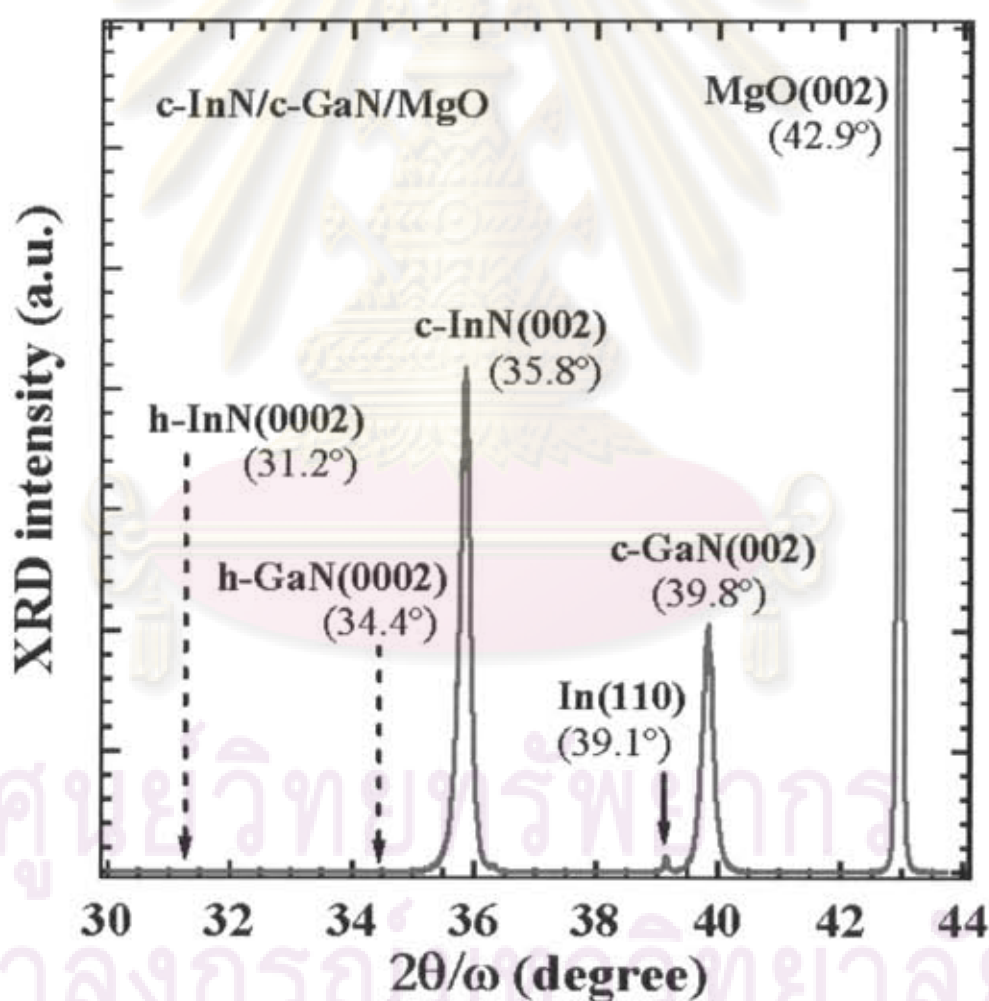
Figure 4.2: A typical (002) $2\theta/\omega$ scan profile of the c-InN film with lowest amount of hexagonal phase inclusion grown on MgO substrate using a c-GaN buffer layer.

reported in chapter 3. This discrepancy can be explained by in-plane compressive strain in the c-InN layer due to the larger lattice mismatch and thermal expansion coefficient between the layer and substrate as shown in Table 1.1. In addition, the In (110) diffraction was also observed. This reflects that the c-InN film was grown under the In-rich growth condition. In addition, it is important to note that no diffraction peak corresponding to the hexagonal-related structures was observed. This indicates that there is no hexagonal (0002) and (10-11) grains parallel to the MgO (001) substrate. However, it cannot be concluded that no generation of hexagonal-phase in both the c-GaN buffer and c-InN layers. However, it is expected that the (0002) hexagonal grains are inclined and constructed on the (111) cubic surfaces. To investigate such hexagonal phase generation, the X-ray RSM measurements were performed and will be discussed in the next section.

Furthermore, the (002) $2\theta/\omega$ scan profiles and ω-scan profiles for all the c-InN films used in this study are shown in Fig. 4.3. The results demonstrate that all the grown films have cubic structure and they were grown under the In-rich growth conditions. Also, we can show that the results can be much improved by using the c-GaN buffer layer on MgO substrates. By using these substrates, as seen in Fig. 4.3 a), the c-InN films with FWHM as small as 7-8 min in $2\theta/\omega$ scan for (002) diffractions was successfully achieved. The values of FWHM obtained from (002) ω-scan (Fig. 4.3 b)) of the c-InN films were determined in the ranges of 22-28 min, which are much lower than previously reported in chapter 3. This indicates that the crystal quality of the c-InN layers is greatly high.

4.3 Investigation of hexagonal phase inclusions

Figures 4.4 a) and b) show X-ray RSMs of the c-InN film (sample Z) grown on MgO substrate using c-GaN as a buffer layer measured along the [110] and [1-10] azimuth axes, respectively. As seen in the X-ray RSMs, the hexagonal (10-11) diffractions were observed about $\omega = \pm 7°$, whereas the hexagonal (0002) diffraction was absent in both the c-GaN buffer and the c-InN layers. These results demonstrate that the hexagonal phase presented in both the c-GaN buffer and c-InN layers is mainly constructed on the cubic (111) surfaces.
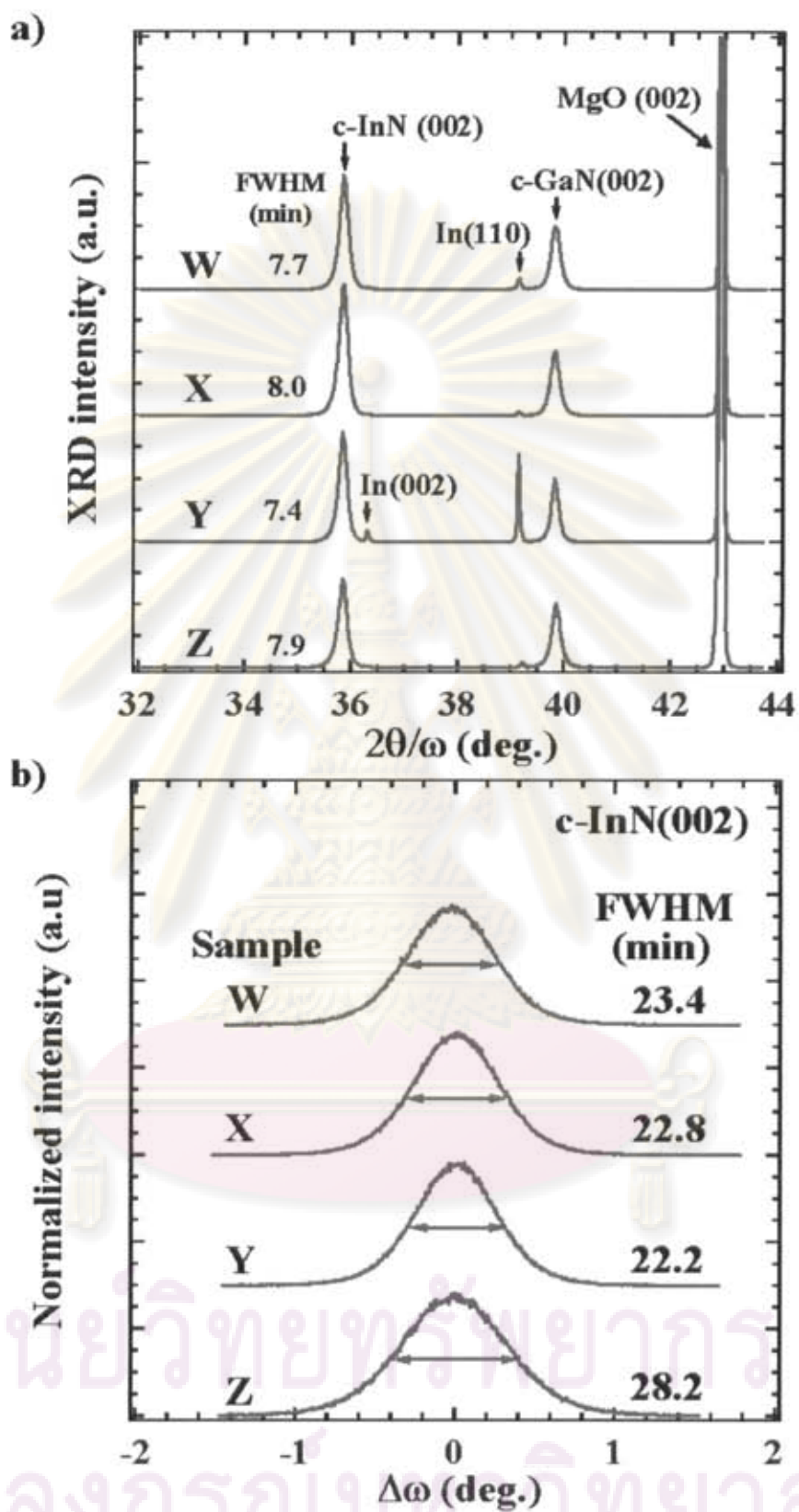
Figure 4.3: a) (002) $2\theta/\omega$-scan profiles and b) ω-scan curves of the corresponding c-InN films grown on MgO substrates using a c-GaN buffer layer.

To investigate the effect of hexagonal phase generation in the c-GaN buffer layer on structural properties of the c-InN upper layer, the hexagonal phase inclusion in both the c-GaN buffer and the c-InN upper layers were examined. Figures 4.5 a) and b) show the X-ray RSMs of the c-InN films of sample W and sample Z, respectively, measured along the [1-10] azimuth axis. As seen in the X-ray RSM result of sample Z (Fig. 4.5 b)), the intensity of the hexagonal (10-11) diffraction peaks in both the c-GaN buffer and the c-InN layers being larger than that of sample W (Fig. 4.5 a)) suggests higher amount of hexagonal phase inclusion. In order to give a quantitatively results of hexagonal phase inclusion in both the c-GaN buffer and the c-InN layers, we calculated the integrated XRD intensity from the cubic (002) and the hexagonal (10-11) diffractions measured by ω-scan. Figures 4.6 and 4.7 show the ω-scan profiles of the cubic (002) and hexagonal (10-11) planes in both the c-GaN buffer and the c-InN layers of samples W and Z, respectively. These ω-scan profiles were extracted from the X-ray RSMs along the [1-10] (Figs. 4.6 a) – d) and Figs. 4.7 a) – d)) and [110] (Figs. 4.6 e) – h) and Figs. 4.7 e) – h)) azimuth axes. The red circles and solid lines are the experimental and the Gaussian fitted curves, respectively. The integrated XRD intensity of each diffraction peaks was calculated from the area under the Gaussian fitted curves as shown in Figs. 4.6 and 4.7. Table 4.1 summarizes the values of the FWHM obtained from $2\theta/\omega$-scan and ω-scan and the amounts of hexagonal phase inclusion in both the c-GaN buffer and the c-InN layers. The amounts of hexagonal phase inclusion in all the c-GaN buffer layers were examined in the range of 2%–8%. It was found that the hexagonal phase inclusion in the c-InN layers much depends on the hexagonal phase inclusion in the c-GaN buffer layer. The highest amount of hexagonal phase inclusion (~24%) was obtained from the c-InN films grown on the c-GaN buffer layer with relatively high hexagonal phase incorporation (~8%). This suggests that the hexagonal phase generation in the c-InN layer maybe induced by the hexagonal phase presented in the c-GaN buffer layer.

a)

b)
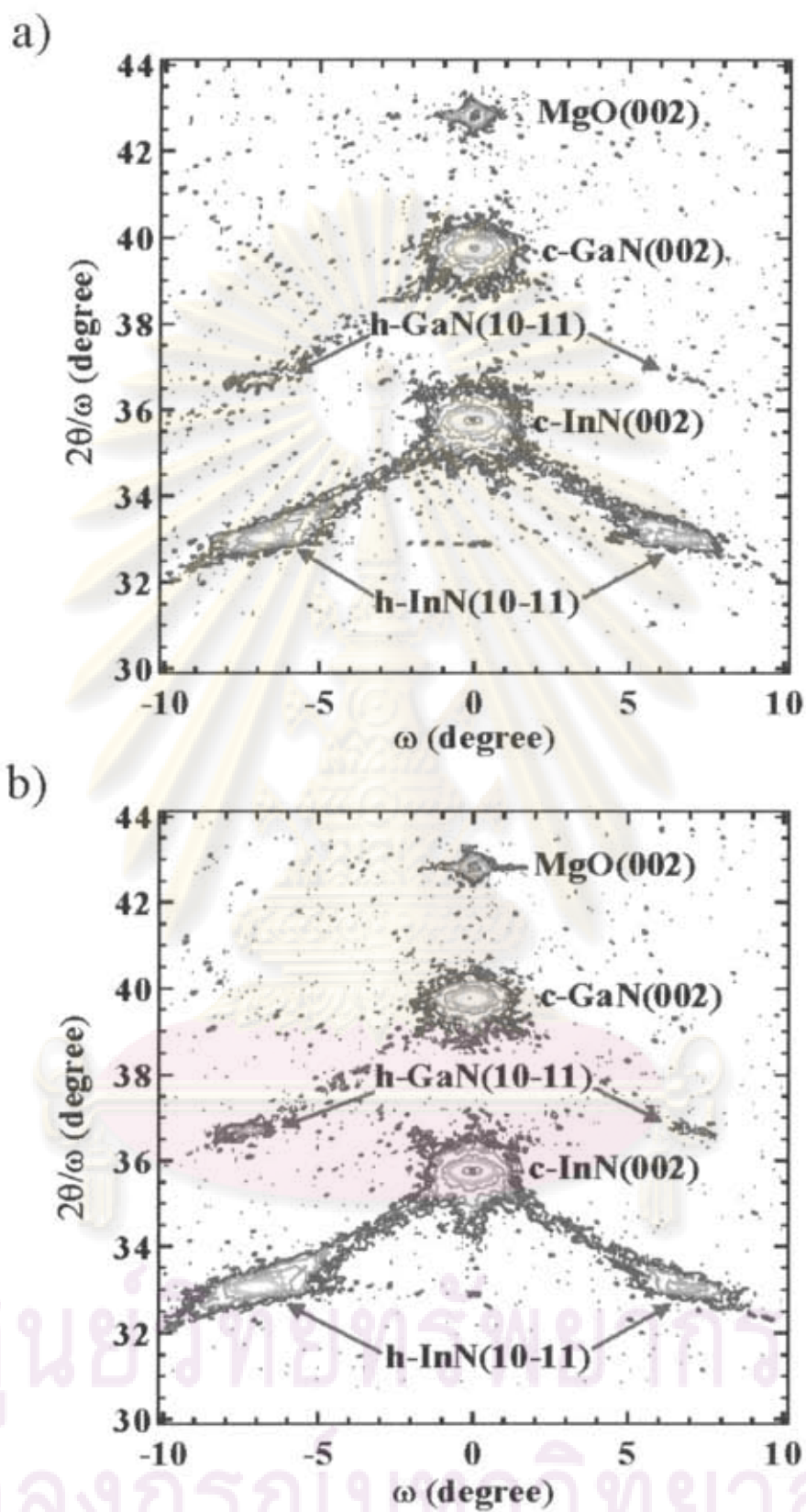
Figure 4.4 : (002) X-ray RSMs of the c-InN film (sample Z) on MgO substrates using a c-GaN buffer layer measured along the (a) [110] and (b) [1-10] azimuth axes.
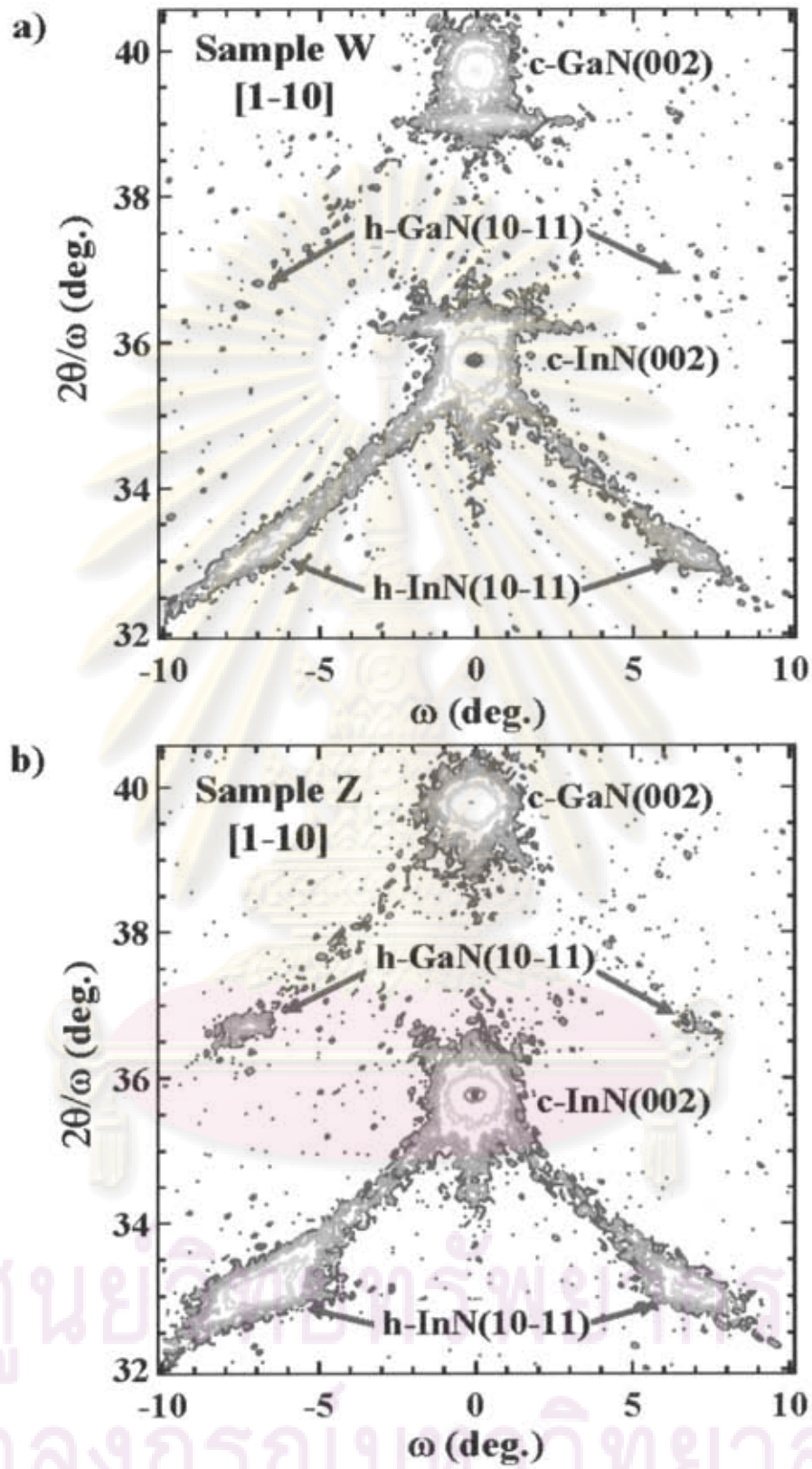
Figures 4.5: (002) X-ray RSMs of the c-InN films of (a) sample W and (b) sample Z measured along the [1-10] azimuth axis.
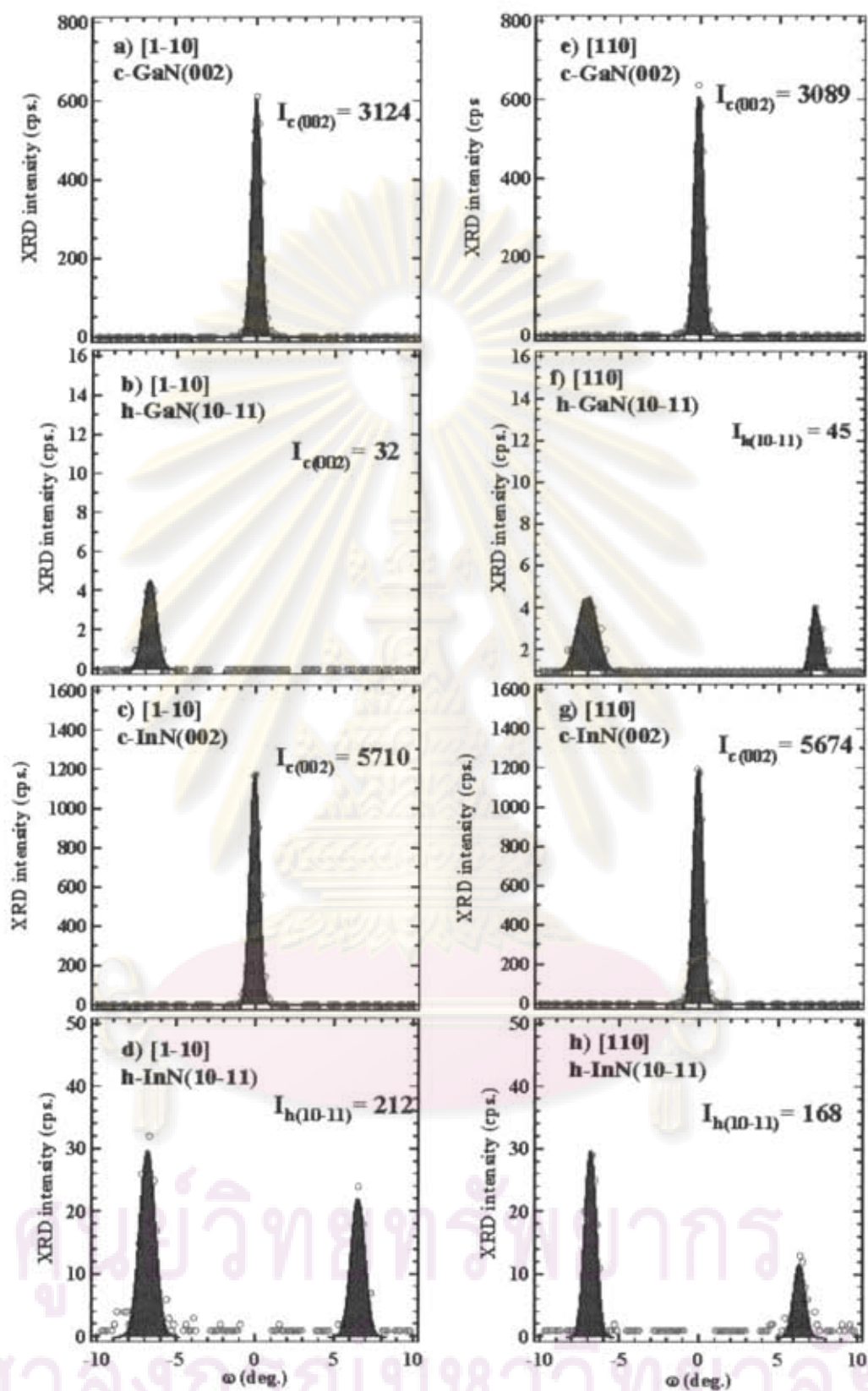
Figure 4.6: ω-scan profiles of cubic (002) and hexagonal (10-11) diffraction peaks in both the c-GaN buffer and the c-InN layers of sample W measured along the [1-10] (a-d) and [110] (e-h) azimuth axes, which were extracted from the X-ray RSMs data.
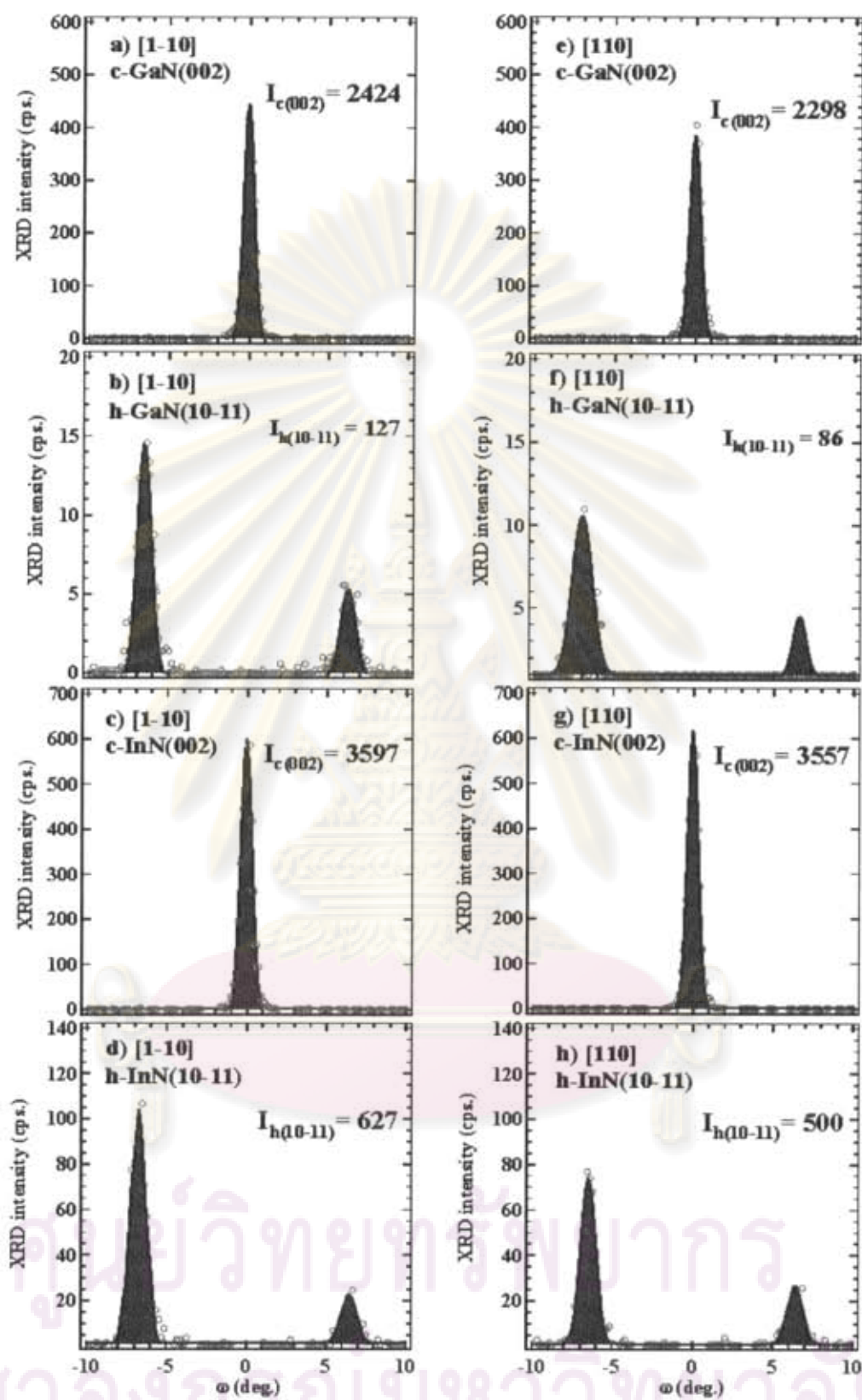
Figure 4.7: ω-scan profiles of cubic (002) and hexagonal (10-11) diffraction peaks in both the c-GaN buffer and the c-InN layers of sample Z measured along the [1-10] (a-d) and [110] (e-h) azimuth axes, which were extracted from the X-ray RSMs data.

Samples	Values of FWHM		Hexagonal phase inclusion (%)	
	$2\theta/\omega$-scan (min)	ω-scan (min)	c-GaN buffer layer	c-InN film
W	7.7	23.4	3	6
X	8.0	22.8	2	8
Y	7.4	22.2	4	15
Z	7.9	28.2	8	24

Table 4.1: The values of FWHM obtained from $2\theta/\omega$-scan and ω-scan and the amounts of hexagonal phase inclusion in both the c-GaN buffer and the c-InN layers.

4.4 Correlation between hexagonal phase inclusion and crystal quality in the c-InN layers

In this part, the possible impact of hexagonal phase inclusion in the c-GaN buffer layer on crystal quality and hexagonal phase inclusion in the c-InN layer is discussed.

Figure 4.8 shows hexagonal phase inclusion and FWHM ($\Delta\omega$) obtained from ω-scan curves, which were taken from Fig. 4.3 b) and Table 4.1, in the c-InN layers as a function of hexagonal phase inclusion in the c-GaN buffer layer. It is found that the hexagonal phase generation and crystal mosaicity in the c-InN layer linearly depend on the amount of hexagonal phase inclusion in the c-GaN buffer layer. Note that the lowest amount of hexagonal phase inclusion and $\Delta\omega$ in the c-InN layer were determined to be 6% and 22 min, respectively, which were obtained from the c-InN films grown on the c-GaN buffer layer with relatively low amount of hexagonal phase inclusion ($<$ 4%). The results indicate that the hexagonal phase inclusion in the c-GaN buffer layer greatly influences on the hexagonal phase generation and crystal quality of the c-InN layers. In addition, the c-GaN buffer layer with lower hexagonal phase inclusion ($<$ 4%) is preferable for growing the high quality pure c-InN layers.
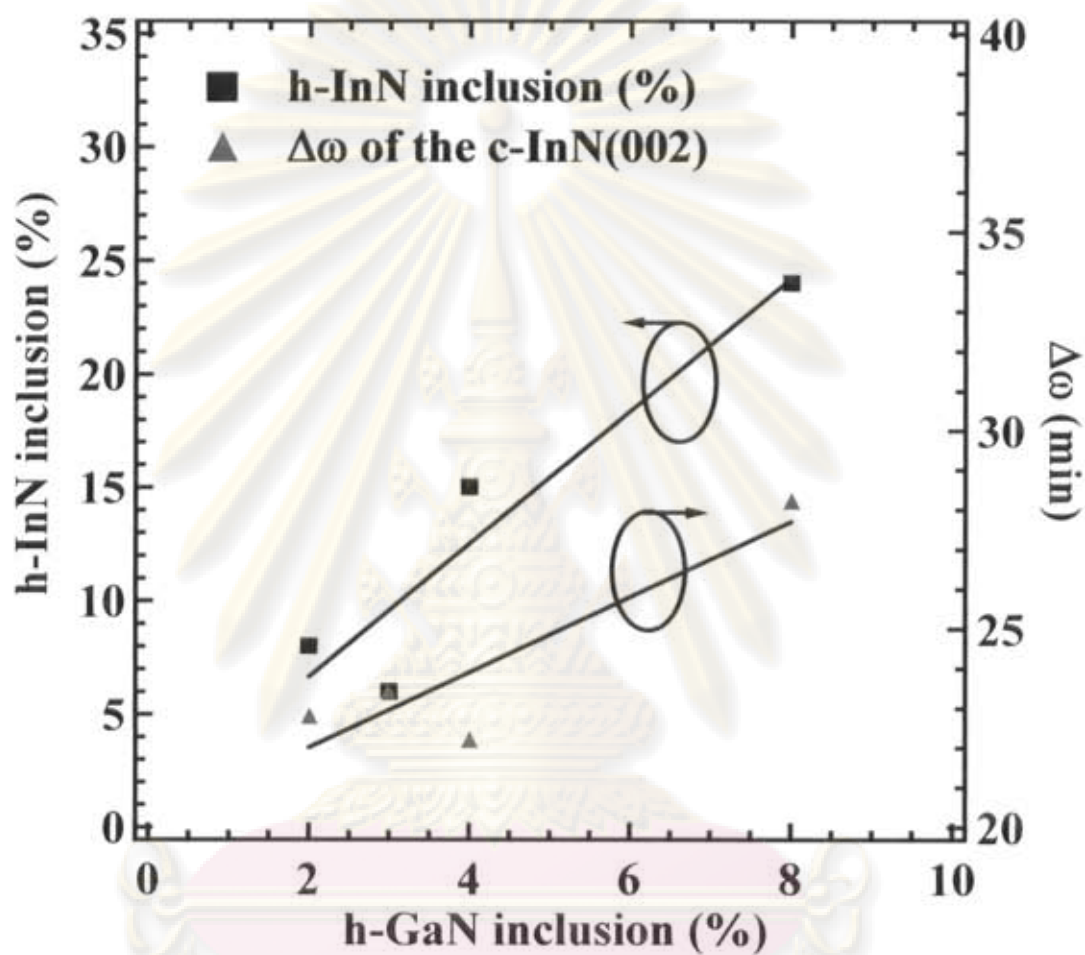
Figure 4.8: Amounts of hexagonal phase inclusion and $\Delta\omega$ in the c-InN layers as a function of hexagonal phase inclusion in the c-GaN buffer layers.

4.5 Correlation between vibrational property and crystal structure

Figure 4.9 shows Raman spectra of the c-InN films with different amounts of hexagonal phase inclusion. The circles and solid lines are the experimental and Lorentzian fitted curves, respectively. The red-dashed and blue-dotted lines indicate the characteristic phonon frequencies of cubic [44, 11] and hexagonal [49] structures, respectively. The Raman shift frequencies and Raman linewidth obtained from the Lorentzian fitted data of the c-InN films with different amounts of hexagonal phase inclusion are summarized in Table 4.2. Starting from the lowest hexagonal phase inclusion ($\sim$6%)[a], two Raman shift frequencies were clearly observed at 468 cm^{-1} and 588 cm^{-1}, which are attributed to the cubic TO [11] and LO [44] phonon modes, respectively. The Raman linewidth of these two peaks is 2 cm^{-1}. This indicates that the crystal quality of c-InN layer with hexagonal phase inclusion lower than 6% considerably high.

For higher amounts of hexagonal phase inclusion, the Raman shift frequencies at about 595 cm^{-1} was observed. As listed in Table 2.1 and 4.2, it is believed that such Raman shift frequency is attributed to the cubic LO phonon mode [11]. The larger values of cubic LO phonon frequency presented in the c-InN films with higher hexagonal phase inclusions (> 6%) is larger than those in film with low hexagonal phase inclusion ($\sim$6%). This is partly due to the strain inside the c-InN film. For the hexagonal phase inclusions of 8%[b] and 15%[c], the Raman spectra show both cubic TO and hexagonal E_2 (high) phonon modes, suggesting mixed states of cubic phase and hexagonal phase structures in the c-InN films. For the highest hexagonal phase inclusion (24%)[d], only the hexagonal E_2 (high) phonon and cubic LO phonon modes were observed while the cubic TO phonon mode was absent. It is concluded that the hexagonal phase subdomain is dominated in the c-InN layer with relatively high hexagonal phase incorporation (> 6%).

---

[a] Sample W
[b] Sample X
[c] Sample Y
[d] Sample Z
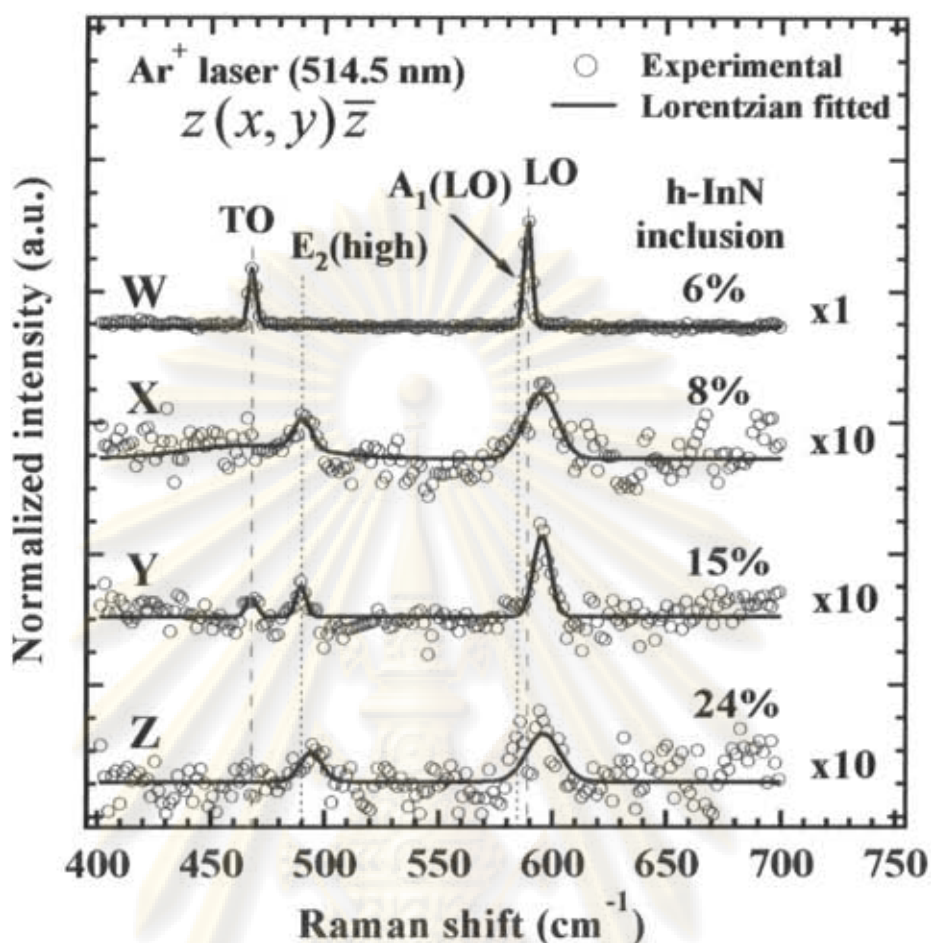
Figure 4.9: Raman spectra of the c-InN films with different amounts of hexagonal phase inclusion.

Samples	h-InN inclusion (%)	Raman shift (cm⁻¹) (FWHM)		
		cubic TO phonon	hexagonal E_2 (high) phonon	cubic LO phonon
W	6	468 (2)	-	588 (2)
X	8	467 (40)	490 (6)	594 (10)
Y	15	467 (4)	489 (4)	595 (5)
Z	24	-	495 (7)	593 (10)

Table 4.2: Lists of the Raman shift frequencies and Raman linewidth (FWHM) obtained from the c-InN films with different amounts of hexagonal phase inclusion.

4.6 Summary

Structural modification and crystal quality of c-InN films on MgO (001) substrates with a c-GaN buffer layer grown by RF-MBE under the In-rich growth condition were systematically analyzed. According to HRXRD measurements, the c-GaN buffer and the c-InN layers have a cubic structure and no hexagonal grains parallel to the MgO (001) surface. Based on the X-ray RSMs results, the hexagonal phase presented in both the c-GaN buffer and c-InN layers is mainly constructed on the cubic (111) surfaces as a formation of stacking faults as well as hexagonal phase subdomains. The hexagonal phase inclusion in the c-GaN buffer layer is found to be a key parameter that influences on the hexagonal phase generation and crystal quality of the c-InN layers. To obtain the higher quality of the c-InN films without the presence of hexagonal phase structure, thus, it is important to control the generation of hexagonal phase in the c-GaN buffer layer. In addition, the Raman scattering results from these c-InN layers confirms the existence of the mixed state of cubic phase and hexagonal phase subdomain.

CHAPTER V

CONCLUSIONS

In the thesis, the author described a study of the structural properties of the c-InN films grown by MBE in details. High-resolution X-ray diffraction (HRXRD) and Raman scattering measurements were mainly used to investigate the structural modification and crystal quality of the c-InN films. The discussion was focused on the effects of growth conditions, especially the In- and the N-rich growth conditions, as well as the buffer layer. The main results and conclusions obtained in this research work are summarized as follows:

(1) The appropriate experimental techniques, which were used to investigate the structural modification and crystal quality of the c-InN films, were selected. We reported that the generation of all the structural phases in the c-InN films can be qualitatively and quantitatively analyzed by HRXRD. Consequently, we propose the quantitatively calculation of the hexagonal phase inclusion in the c-InN layers using ω-scan extracted from the X-ray RSMs data.

(2) The effects of the In- and the N-rich growth conditions on structural modification and crystal quality of the c-InN films grown on GaAs (001) substrates by MBE were investigated. Based on HRXRD results, the InN grown films with a cubic structure and without hexagonal phase subdomains parallel to the GaAs (001) surface were grown. On the other hand, the inclined hexagonal phase subdomains presented in the c-InN films were clearly observed using X-ray RSMs. The results show that, the hexagonal phase, which is oriented in direction of [0001]//[111], is generated as a formation of stacking faults and hexagonal phase subdomains. For the N-rich growth condition, the c-InN films with flatter surface, higher uniformity of grain-size and lower cubic phase purity were obtained. In addition, the hexagonal phase becomes a main crystal structure, affecting on the vibrational property of the

InN crystal. For the In-rich growth condition, high crystal quality c-InN films with the narrowest FWHM in ω-scan of 36 min and the highest cubic phase purity of 92% were achieved. These results suggest that the In-rich growth condition is a key parameter in the growth of single structural-phase c-InN with higher crystalline quality.

(3)   Effect of a c-GaN buffer layer on the generation of hexagonal phase in the c-InN films on MgO (001) substrates grown under the In-rich growth condition was systematically investigated. HRXRD results showed that both the c-GaN buffer and the c-InN grown layers have a cubic structure and no hexagonal grain parallel to MgO (001) substrate. Based on X-ray RSMs, the hexagonal phase presented in both the c-GaN buffer and the c-InN layers was generated on the cubic (111) surfaces. Further results demonstrated that the hexagonal phase inclusion in the c-GaN buffer layer is a very important factor that induces the hexagonal phase generation in the c-InN upper layers. In addition, the Raman scattering results also show the vibrational modes related to the presence of hexagonal phase single crystal for the c-InN films with relative high amount of hexagonal phase inclusion (> 6%). To obtain higher quality c-InN films without the presence of hexagonal structure, thus, it is important to control the generation of hexagonal phase in the c-GaN buffer layer.

As shown by these results, the structural modification in the c-InN films grown by MBE is in connection with the generation of stacking faults and/or hexagonal phase sumdomains. The growth conditions and the hexagonal phase presented in the cubic buffer layer are mainly affecting parameters, which results in the generation of hexagonal phase and crystal quality of the c-InN films. To grow hexagonal phase inclusion free c-InN films, the cubic buffer layer with lower amount of the hexagonal phase inclusion (< 4%) is required. The growth should be also performed under the In-rich growth condition. The results obtained here can be not only to interpret the c-InN films; but may also be extended to explain the structural properties of other novel semiconductors. Hopefully, the obtained information is very useful for the full understanding of the structural property of cubic III-nitride base devices. Further work is still necessary to fully clarify the affecting parameters on the structural modification in the growth of epitaxial cubic III-nitride films

REFERENCES

[1] T. L. Tansley and C. P. Foley. Optical band gap of indium nitride, *J. Appl. Phys.* **59** (1986): 3241-3244.

[2] Kozo Osamura, Kazuo Nakajima and Yataro Murakami. Fundamental Absorption Edge in GaN, InN and Their Alloys, *Solid State Communications.* **11** (1972): 617-621.

[3] H. J. Hovel and J. J. Cuomo. Electrical and Optical Properties of rf-Sputtered GaN and InN, *Appl. Phys. Lett.* **20** (1972): 71-73.

[4] Takashi Matsuoka. Progress in nitride semiconductors from GaN to InN-MOVPE growth and characteristics, *Superlattices and Microstructures* **37** (2005): 19-32.

[5] K. Xu, W. Terashima, T. Hata, N. Hashimoto, Y. Ishihani and A. Yoshikawa. Step-Flow Growth of InN on N-polarity GaN Template by Molecular Beam Epitaxy with a Growth Rate of 1.3 um/h, *phys. stat. sol. (c)* **1** (2002): 377-381.

[6] Y. Saito, H. Harima, E. Kurimoto, T. Yamaguchi, N. Teraguchi, A. Suzuki, T. Araki and Y. Nanishi. Growth Temperature Dependence of Indium Nitride Crystalline Quality Grown by RF-MBE, *phys. stat. sol. (b)*. **3** (2002): 796-800.

[7] Tokou Yodo, Hiroaki Yona, Hironori Ando and Daiki Nosei. Strong Band edge Luminescence from InN films grown on Si substrates by electron cyclotron resonance-assisted molecular beam epitaxty, *Appl. Phys. Lett.* **80** (2002): 968-970.

[8] Yasushi Nanishi, Yoshiki Saito and Tomohiro Yamaguchi. RF-Molecular Beam Epitaxy Growth and Properties of InN and Related Alloys, *Jpn. J. Appl. Phys.* **42** (2003): 2549- 2559.

[9] S. V. Ivanov, T. V. Shubina, V. N. Jmerik, V. A. Vekshin, P. S. Kop'ev and B. Monerma. Plasma-assisted MBE growth and characterization of InN on sapphire, *Journal of Crystal Growth* **269** (2004): 1-9.

[10] Hiroyuki Yaguchi, Yoshihiro Kitamura, Kenji Nishida, Yohei Iwahashi, Yasuto Hijikata and Sadafumi Yoshida. Growth of high-quality hexagonal InN on 3C-SiC (001) by molecular beam epitaxy, *phys. stat. sol. (c)* **2** (2005): 2267– 2270.

[11] Y. Iwahashi, H. Yaguchi, A. Nishimoto, M. Orihara, Y. Hijikata and S. Yoshida. RF-MBE growth of cubic InN films on MgO (001) substrates, *phys. stat. sol. (c)* **3** (2006): 1515–1518.

[12] T. Nakamura, K. Iida, R. Katayama, T. Yamamoto and K. Onabe. RF-MBE growth and structural characterization of cubic InN films on GaAs, *phys. stat. sol. (b)* **243** (2006): 1451–1455.

[13] J. Ohta, K. Mitamura, A. Kobayashi, T. Honke, H. Fujioka and M. Oshima. Epitaxial growth of InN on nearly lattice-matched (Mn,Zn)Fe$_2$O$_4$, *Solid State Communications* **137** (2006): 208-211.

[14] T. Nakamura, Y. Tokumoto, P. Ktayama, T. Yamamoto and K. Onabe. RF-MBE growth and structural characterization of cubic InN films on yttria-stabilized zirconia (001) substrates, *Journal of Crystal Growth* **301-302** (2007): 508-512.

[15] G. Shikata, S. Hirano, T. Inoue, M. Orihara, Y. Hijikata, H. Yaguchi and S. Yoshida. RF-MBE growth of a-plane InN on r-plane sapphire with a GaN under layer, *Journal of Crystal Growth* **301-302** (2007): 517-520.

[16] Tohru Tsuchiya, Osamu Miki, Kohji Shimada, Masato Ohnishi, Akihiro Wakahara, and Akira Yoshida. Epitaxial growth of InN films on MgAl$_2$O$_4$ (111) substrates, *Journal of Crystal Growth* **220** (2000): 185-190.

[17] Akio Yamamoto, Masato Adachi and Akihiro Hashimoto. Enhanced two-dimensional growth of MOVPE InN films on sapphire (0001) substrates, *Journal of Crystal Growth* **230** (2001): 351–356.

[18] Akio Yamamoto, Tomohiro Shin-ya, Toshimitsu Sugiura and Akihiro Hashimoto. Characterization of MOVPE-grown InN layers on α-Al$_2$O$_3$ and GaAs substrates, *Journal of Crystal Growth* **189/190** (1998): 461-465.

[19] Ashraful G. Bhuiyan, A. Yamamoto, A. Hashimoto and Y. Ito. High temperature growth of InN on GaP (111)B substrate using a new two-step growth method, *Journal of Crystal Growth* **236** (2002): 59–65.

[20] C.-L. Wu, C.-H. Shen, H.-Y. Chen, S.-J. Tsai, H.-W. Lin, H.-M. Lee, S. Gwo, T.-F. Chuang, H.-S. Chang and T.-M. Hsu. The effects of AlN buffer on the properties of InN epitaxial films grown on Si (111) by plasma-assisted MBE, *Journal of Crystal Growth* **288** (2006): 247-253.

[21] J. Wu, W. Walukiewicz, K. M. Yu, J. W. Ager III, E. E. Haller, Hai Lu, William J. Schaff, Yoshiki Saito and Yasushi Nanishi. Unusual properties of the fundamental band gap of InN, *Appl. Phys. Lett.* **80** (2002): 3967-3969.

[22] A. G. Bhuiyan, A. Hashimoto and A. Yamamoto. Indium nitrides (InN): A review of growth, characterization and properties, *J. Appl. Phys.* **94** (2003): 2779-2808.

[23] Akio Yamamoto, Mitsunori Tsujino, Mitsugu Ohkubo and Akihiro Hashimoto. Metalorganic chemical vapor deposition growth of InN for InN/Si tandem solar cell, *Solar Energy Materiel and Solar cells* **35** (1994): 53-60.

[24] Z. Q. Li, H. Chen, H. F. Liu, J. H. Li, L. Wan, S. Liu, Q. Huang and J. M. Zhou. MBE Growth and X-ray study of high quality cubic-GaN on GaAs (001), *Journal of Crystal Growth* **208** (2000): 786-790.

[25] H. Okamura, S. Yoshida and T. Okahisa. Optical properties near the band gap on hexagonal and cubic GaN, *Appl. Phys. Lett.* **64** (1994): 2997-3000.

[26] H. Okumura, K. Ohta, G. Feuillet, K. Balakrishnan, S. Chichibu, H. Hamaguchi, P. Hacke and S. Yoshida. Growth and Characterization of cubic GaN, *Journal of Crystal Growth* **178** (1997): 113-133.

[27] X. Wang and A. Yoshigawa. Molecular beam epitaxy growth of GaN, AlN and InN, *Progress in Crystal Growth and Characterization of Materials* **48/49** (2004): 42-103.

[28] Mario Birkholz. *Thin Film Analysis by X-ray Scattering*. Berlin: Wiley-VCH, 2006.

[29] D. Keith Brown and Brian K. Tanner. *High Resolution X-ray Diffractometry and Tophography*. UK: T. J. International Ltd, 1998.

[30] M. Kuball. Raman spectroscopy of GaN, AlGaN and AlN for process and growth monitoring/control, *Surface and Interface Analysis* **31** (2001): 987-999.

[31] M. Balkanski and R. F. Wallis. *Semiconductor Physics and Applications*. UK: Oxford University Press, 2000.

[32] M. Kaball, J. W. Pomeroy, M. Wintrebert-Fouquet, K. S. A. Butcher, Hai Lu and W. J. Schaff. A Raman spectroscopy study of InN, *Journal of Crystal Growth* **269** (2004): 59-65.

[33] Hiroyuki Yaguchi, Jun Wu, Baoping Zhang, Yusabura Segawa, Hiroyuki Nagasawa, Kentaro Onabe and Yasuhiro Shiraki. Micro Raman and micro photoluminescence study of cubic GaN grown on 3C-SiC (001) substrates by metalorganic vapor phase epitaxy, *Journal of Crystal Growth* **195** (1998): 323-327

[34] X. L. Sun, Hui Yang, L. X. Zheng, D. P. Xu, J. B. Li, Y. T. Wang, G. H. Li and Z. G. Wang. Stability investigation of cubic GaN films grown by metalorganic chemical vapor deposition on GaAs (001), *Appl. Phys. Lett.* **74** (1999): 2827-2829.

[35] M. Moret, S. Ruffenach-Clur, N. Moreaud, O. Briot, J. Calas and R.L. Aulombard. MOCVD Growth of Cubic Gallium Nitride: Effect of V/III Ratio, *phys. stat. sol. (a)* **176** (1999): 493-496.

[36] Harutoshi Tsuchiya, Kenji Sunaba, Syogo Yonemura, Takashi Suemasu and Fumio Hasegawa. Cubic dominant GaN growth on (001) GaAs substrates by hydride vapor phase epitaxy, *Jpn. J. Appl. Phys.* **36** (1997): L1-L3.

[37] บัญชา ธนบุญสมบัติ. *การศึกษาวัสดุโดยเทคนิคดิฟแฟรกชัน.* กรุงเทพฯ: สำนักพิมพ์สมาคม ส่งเสริมเทคโนโลยี (ไทย-ญี่ปุ่น), 2537.

[38] X.L. Sun, Y.T. Wang, Hui Yang, J.B. Li, L.X. Zheng, D.P. Xu and Z.G. Wang. The content calculation of hexagonal phase inclusions in cubic GaN films on GaAs (001) substrates grown by metalorganic chemical vapor deposition, *Thin Solid Films* **368** (2000): 237-240.

[39] Charles Kittel. *Introduction to Solid State Physics.* California: John Wiley & Sons, 1996.

[40] X. H. Zheng, B. Qu, Y. T. Wang, Z. H. Feng, J. Y. Han, Hui Yang and J. W. Liang. Investigation of {111}A and {111}B planes of c-GaN epilayers grown on GaAs (001) by MOCVD, *Journal of Crystal Growth* **233** (2001): 52-56.

[41] P. Rinke, M. Sceffler, A. Qteish, M. Winkelnkemper, D. Bimberg and J. Neugebauer. Band gap and band parameters of InN and GaN from quasi-particle energy calculations based on exact-exchange density-functional theory, *Appl. Phys. Lett.* **89** (2006): 161919-1 -161919-3.

[42] C. A. Arguello, D. L. Rousseau and S. P. S. Porto. First-order Raman effect in wurtzite-type crystalls, *Phys. Rev.* **181** (1969): 1351-1363.

[43] Ming-Chih Lee, Heng-Ching Lin, Yung-Chung Pan, Chen-Ke Shu, Jehn Ou, Wen-Hsiung chen and Wei-Kuo Chen. *Appl. Phys. Lett.* **73** (1998): 2606-2608.

[44] A. Tabata, A. P. Lima, L. K. Teles, L. M. R. Scolfaro, and J. R. Leite, V. lemos, B. Schöttker, T. Frey, D. Schikora and K. Lischka. Structural properties and Raman modes of zinc blende InN epitaxial layers, *Appl. Phys. Lett.* **74** (1999): 362-364.

[45] G. Kaczmarczyk, A. Kaschner, S. Reich, A. Hoffmann, C. Thomsen, D.J. As, A.P. Lima, D. Schikora, K. Lischka, R. Averbeck and H. Riechert. Lattice dynamics of hexagonal and cubic InN: Raman scattering experiment and calculation, *Appl. Phys. Lett.* **76** (2000): 2122-2124.

[46] S. Suandon. *Structural property analysis of GaN grown on GaAs by MOVPE using transmission electron microscopy.* Master's thesis, Department of Physics, Faculty of Science, Chulalongkorn University, 2005.

[47] F. Hasegawa. *Growth of high quality thick cubic GaN on (001) GaAs by halide vapor phase epitaxy: influence of As autodoping from the substrate*, Institute of Material Science, University of Tsukuba, Japan, 1997.

[48] B. D. Cullity. *Elements of X-ray diffraction.* London: Addison-Wesley, 1956.

[49] V. Yu. Davydov, V. V. Emtsev, I. N. Goncharuk, A. N. Smirnonov, V. D. Petrikov, V. V. Mamutin, V. A. Vekshin, S. V. Ivanov, M. B. Smirnov and T. Inushima. Experimental and theoretical studies of phonons in hexagonal InN, *Appl. Phys. Lett.* **75** (21999): 3297-3299.

[50] D. B. Holt and B. G. Yacobi. *Extended Defects in Semiconductors: Electronic properties, Device Effects and Structures.* UK: Cambridge University Press, 2007.

APPENDICES

APPENDIX A

Contributions from this thesis to the field

The MBE grown samples that have been used in the thesis were prepared at Prof. Kentaro Onabe's laboratory, the University of Tokyo and Prof. Hiroyuki Yaguchi's laboratory, Saitama University, Japan. The author did experiments of HRXRD and participated during the SEM, EDX and AFM measurements at the Scientific and Technological Research Equipment Centre (STREC), Chulalongkorn University. The author also did Raman spectroscopy experiments at the Gem and Jewelry Institute of Thailand (Public Organization), Chulalongkorn University. The author did the simulation and analyzed all the obtained results. The author performed the optical microscopy at the National Metal and Materials Technology Center (MTEC) and interpreted the obtained results. The author summarized all results, concluded the research work, participated in the regional and international conferences for seven times (APPENDIX B), and wrote two international scientific paper (APPENDICES C and D).

APPENDIX B

Publications

1.   **S. Kuntharin,** S. Sanorpim, T. Nakamura, R. Katayama and K. Onabe, 'Structural Investigation of Cubic-phase InN on GaAs (001) Grown by MBE Under In- and N-rich Growth Conditions', *Advanced Materials Research*, **31** (2008): 215-217.

2.   **S. Kuntharin** , S. Sanorpim, H. Yaguchi, Y. Iwahashi, M. Orihara, Y. Hijakata and S. Yoshida "High Resolution X- ray Diffraction and Raman Scattering Studies of Cubic-phase InN Films Grown by MBE", *Advanced Materials Research*, (2008), Accepted.

International Conference Presentations

3.   **S. Kuntharin**, S. Sanorpim, T. Nakamura, R. Katayama, and K. Onabe 'Structural investigation of Cubic-phase InN on GaAs(001) Grown by MBE Under In- and N-rich Growth Conditions' *4th International Conference on Materials for Advanced Technologies* (ICMAT 2007), Singapore, July 1-6, 2007. (oral presentation)

4.   **S. Kuntharin**, S. Sanorpim, Y. Iwahashi, H. Yaguch, A. Nishimoto, M. Orihara, Y. Hijakata and S. Yoshida, 'Examination and analysis of hexagonal component in cubic InN films grown on MgO substrates by MBE with cubic GaN buffer layer' *3rd Mathematics and Physical Sciences Graduate Congress* (MPSGC 2007), Malaysia, December 12-14, 2007. (oral presentation)

5.   **S. Kuntharin**, S. Sanorpim, Y. Iwahashi, H. Yaguchi, A. Nishimoto, M. Orihara, Y. Hijakata and S. Yoshida 'X-ray and Raman Studies of Hexagonal-Phase Incorporation on Cubic-Phase InN Films Grown By MBE' *International Conference on Smart Materials-Smart/Intelligent Materials and Nano Technology & 2nd International Workshop on Functional Materials and Nanomaterials (SmartMat-'08 & IWOFM-2)*, Chaingmai, Thailand, April 22-24, 2008. (oral presentation)

Regional Conference Presentations

6.   **S. Kuntharin**, S. Sanorpim, T. Nakamura, R. Katayama and K. Onabe, 'STRUCTURAL INVESTIGATION OF CUBIC-InN GROWN ON GALLIUM ASENIDE BY MBE UNDER INDIUM AND NITROGEN-RICH GROWTH CONDITIONS' *15th Academic Conference*, Faculty of science, Chulalongkorn University, Thailand, March 15-16, 2007. (oral presentation)

7.   **S. Kuntharin**, S. Sanorpim, T. Nakamura, R. Katayama and K. Onabe, 'Effect of Indium and Nitrogen-rich growth conditions on structural property of cubic-InN on GaAs' *Siam Physics Congress* (SPC 2007), Nakorn Pratom, Thailand, March 22-24, 2007. (oral presentation)

8.   **S. Kuntharin**, Sakultum Sanorpim, Takahisa Nakamura, Ryuji Katayama and Kentaro Onabe' STRUCTURAL INVESTIGATION OF c-InN FILMS GROWN ON GaAs BY MBE UNDER INDIUM OR NITROGEN-RICH GROWTH CONDITIONS' *33th Congress on Science and Technology of Thailand* (STT 2007), Walailuk University, Thailand, October 18-20, 2007. (oral presentation)

9.   **S. Kuntharin**, S. Sanorpim, Y. Iwahashi, H. Yaguchi, A. Nishimoto, M. Orihara, Y. Hijakata and S. Yoshida 'Investigation of hexagonal-phase generation in cubic InN films on MgO (001) substrates grown by MBE with cubic GaN buffer layer' *Siam Physics Congress* (SPC 2008), Thailand, March 20-22, 2008. (oral presentation)
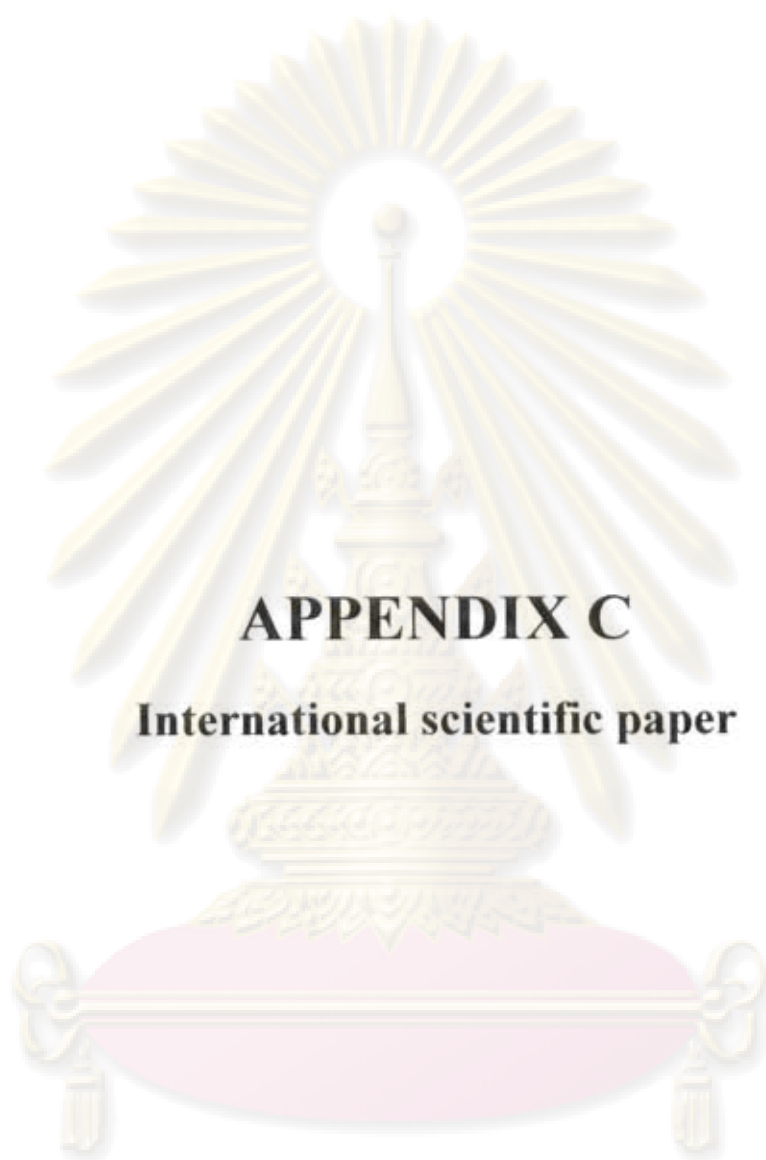
APPENDIX C

International scientific paper

ศูนย์วิทยทรัพยากร
จุฬาลงกรณ์มหาวิทยาลัย

Structural Investigation of Cubic-phase InN on GaAs (001) Grown by MBE Under In- and N-rich Growth Conditions

S. Kuntharin[1], S. Sanorpim[1,a], T. Nakamura[2], R. Katayama[2] and K. Onabe[2,b]

[1]Department of Physics, Faculty of Science, Chulalongkorn University, Bangkok 10330, Thailand
[2]Department of Advance Material Science, The University of Tokyo, Kashiwanoha, Kashiwa 277-8561, Japan
[a]Sakuntam.S@chula.ac.th, [b]onabe@k.u-tokyo.ac.jp

Keywords: c-InN, In-rich growth condition, high resolution x-ray diffraction, Raman scattering

Abstracts. We have investigated effect of the In- and N-rich growth conditions on the structural modification of cubic-phase InN (c-InN) films grown on GaAs (001) substrates by rf-plasma-assisted molecular beam epitaxy (RF-MBE). High resolution x-ray diffraction (HRXRD) and Raman scattering measurements were performed to examine the hexagonal phase generation in the c-InN grown films. It is evident that higher crystal quality c-InN films with higher cubic phase purity (~82%) were achieved under the In-rich growth condition. On the other hand, for the N-rich growth condition, the c-InN films exhibited higher incorporation of hexagonal phase, which is generated in the cubic phase through the incidental stacking faults on the c-InN (111) planes. Our results demonstrate that the In-rich growth condition plays a critical role in the growth of high quality c-InN films with higher cubic phase purity.

Introduction

Indium nitride (InN) is a very attractive material for future optoelectronic devices due to its outstanding of material properties such as smallest electron effective mass and smallest direct bandgap among III-nitride semiconductors [1]. In fact, InN crystallizes usually in either a thermodynamically stable wurtzite structure with a hexagonal symmetry or a metastable zinc-blende structure with a cubic symmetry [2, 3]. Less work has been done with cubic phase InN (c-InN) than with hexagonal phase InN (h-InN). However, some physical properties of c-InN are more suitable for device applications. It has been demonstrated that c-InN grown on GaAs substrate can be used to fabricate light-emitting diodes (LEDs) with an upright structure and can be incorporated in the mature GaAs device technology more easily than h-InN. Further, zinc-blende structure, which has the cubic symmetry, is expected to have a higher mobility due to its lower phonon scattering such the higher crystallographic symmetry [4]. However, high quality c-InN films with high cubic-phase purity are usually prepared under certain special growth conditions due to the metastable nature of c-InN.

In this paper, we report effect of the growth conditions, namely In- and N-rich growth conditions, on the structural modification of the c-InN films grown on GaAs (001) substrates by the rf-plasma-assisted molecular beam epitaxy (RF-MBE).

Experiment

The c-InN films for this study were grown at the University of Tokyo by RF-MBE in a system described elsewhere [5]. A standard MBE source provides the In flux. A rf-plasma source was used to produce active N flux. The growth temperature was varied in the range of 450-500 °C. While the In flux and the rf power were kept constant at 1.5×10^{-4} Pa and 300 W, respectively. To change the V/III ratio, the supplied N_2 flow rate was varied in the range of 1.5 ~ 2.5 sccm. According to these growth conditions, it is found that the In- and N-rich growth conditions can be controlled by the growth temperature and the supplied N_2 flow rate as well as the V/III ratio. The c-InN films were characterized by high resolution x-ray diffraction (HRXRD), scanning electron microscopy (SEM), atomic force microscopy (AFM), optical microscopy and Raman scattering.
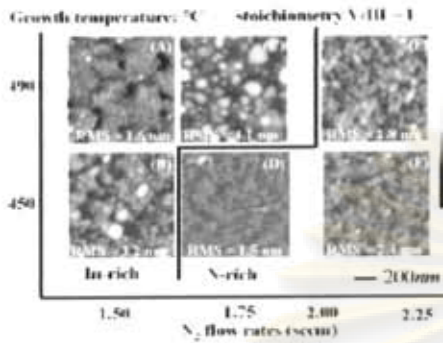
Fig. 1 AFM images of the c-InN films grown at different growth temperatures and supplied N₂ flow rates.
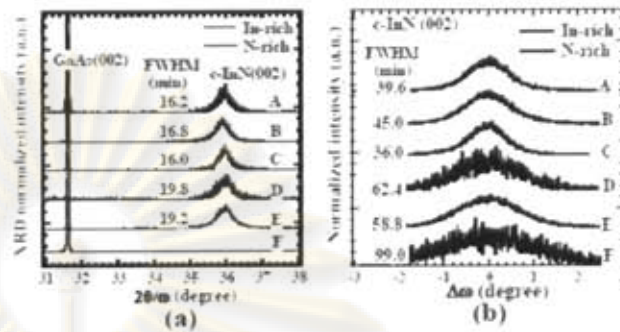
Fig. 2 (a) (002) 2θ-ω HRXRD profiles and (b) ω-rocking curves of the corresponding c-InN films.

Results and discussion

The key issue to identify the growth conditions is the In droplets [5], which are seen on the surface for lower supplied N₂ flow rates and higher growth temperatures. An appearance of the In droplets indicate an insufficient V/III ratio, resulting in the In-rich growth condition. On the other hand, the In-droplet-free surface reflects that the growing surface is under the N-rich growth condition. Details of the film morphology are given elsewhere [5]. Here, we evaluated an impact of the In- and N-rich growth conditions on the size of the grains in our films. Figure 1 shows AFM plan-view images of the films grown at different growth temperatures and supplied N₂ flow rates. The condition for the surface-stoichiometry is designated by the bolded line. In the particular example of Fig. 1, it is clearly seen that the In- and N-rich growth conditions strongly effect on the size of the grains. For the In-rich growth condition, the surface RMS roughness of the films increases with decreasing growth temperature. In contrast, for the N-rich growth condition, the surface RMS roughness of the films increases with increasing growth temperature. The results suggest that, unlike the N-rich growth condition [5], the formation of grains in the c-InN films grown under In-rich growth condition is caused by limited surface diffusion processes due to the insufficient V/III ratio.

The (002) HRXRD 2θ-ω and (002) ω-rocking curves are shown in Figs. 2(a) and 2(b), respectively. Full width at half maximum (FWHM) of the c-InN (002) reflections obtained from 2θ-ω and ω-rocking curves for all the films grown under the In-rich condition (bolded line) are narrower than that for the films grown under the N-rich condition (thinned line). The narrowest FWHM of ω-scan is around 36 min for the film grown at 490°C with supplied N₂ flow rate of 1.50 sccm. These results indicate that the c-InN films with higher crystal quality can be archived under the In-rich condition.

Finally, we evaluated the possible impact of the In- and N-rich growth conditions on the hexagonal phase generation in the c-InN films. Figure 3 shows X-ray reciprocal space mappings with the incident azimuth axis of the X-ray beam along the <1-10> direction of the InN films grown under In-(sample A, Fig. 3(a)) and N-rich (sample E, Fig. 3(b)) growth conditions. It is seen that the GaAs (002) and c-InN (002) diffractions were observed at ω = 18° and the h-InN (10-11) diffractions were observed at ω = 18 – 7°. This indicates that the hexagonal phase incorporated in the cubic phase through the incidental stacking faults on the c-InN (111) planes as known for c-GaN grown on GaAs [6]. Further, amount of the incorporated hexagonal phase was determined from the ratio of the integrated X-ray diffraction intensities of the cubic (002) and hexagonal (10-11) diffractions measured by the ω-scan [7]. It is found that the cubic phase purity as high as more than 82% was obtained for the c-InN film grown under the In-rich growth condition with growth temperature of 490°C and supplied N₂ flow rate of 1.50 sccm. On the other hand, the hexagonal phase structure becomes dominated in the c-InN films grown under the N-rich growth condition. We also find that, as shown in Fig. 4, Raman spectra of the c-InN films grown under the N-rich
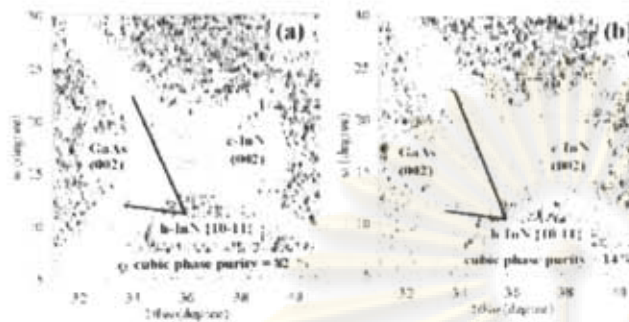
Fig. 3 X-ray reciprocal space mappings of the InN films grown at 490 °C with the N_2 flow rates of (a) 1.5 sccm (sample A) and (b) 2.25 sccm (sample E).
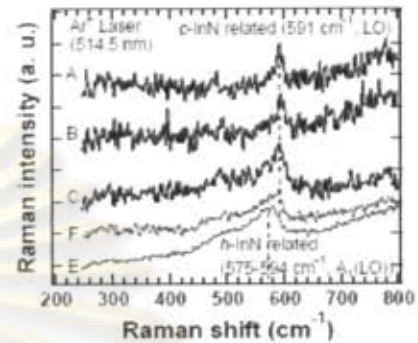
Fig. 4 Raman spectra of the c-InN films grown at different growth temperatures and N flow rates.

growth condition (samples E and F) include hexagonal A_1 longitudinal optical (LO)-phonon mode at 591 cm^{-1} [8] as well as the cubic longitudinal optical (LO)-phonon mode at 594 cm^{-1} [8, 9]. The broadening of Raman spectra is attributed to disorder-activated Raman scattering, relating to phonon density of state of c-InN crystal [9]. On the other hand, no h-InN related Raman features were observed from the c-InN films grown under the In-rich growth condition (samples A, B and C). The difference in the Raman spectra is in connection with the different amount of incorporated hexagonal phase in the c-InN films, which agrees well with the results of HRXRD.

Summary: The effects of the In- and N-rich growth conditions on the structural modification of c-InN films grown on GaAs (001) substrates by RF-MBE were investigated. Higher crystal quality c-InN films can be achieved under the In-rich growth conditions with the narrower FWHM of ω-scan of 36 min and higher cubic phase purity of 82%. Our results demonstrate that the surface-stoichiometry plays a critical role in the growth of single structural-phase c-InN with higher crystalline quality.

References

[1] A. G. Bhuiyan, A. Hashimoto and A. Yamamoto: J. Appl. Phys. Vol. 94 (2003), p. 2779

[2] S. V. Ivanov, T. V. Shubina, V. N. Jmerik, V. A. Vekshin, P. S. Kop'ev and B. Monemar: J. Crystal Growth Vol. 269 (2004), p. 1

[3] D.J. As, D. Schikora and K. Lischka: phys. stat. sol. (c) Vol. 6 (2003), p. 1607

[4] O. Brandt, H. Yang, H. Kostial, K.H. Ploog : Appl. Phys. Lett. Vol. 69 (1996), p. 2707

[5] T. Nakamura, K. Iida, R. Katayama and K. Onabe: phys. stat. sol. (b) Vol. 235 (2003), p. 1451

[6] S. Sanorpim, E. Takuma, R. Katayama, K. Onabe, H. Ichinose and Y. Shiraki: phys. stat. sol. (b) Vol. 234 (2002), p. 840

[7] H. Tsuchiya, K. Sunaba, S. Yonemura, T. Suemasu, and H. Seki: Jpn. J. Appl. Phys. Vol. 36 (1997), p. L1

[8] Y. Iwahashi, H. Yaguchi, A. Nishimoto, M. Orihara, Y. Hijikata and S. Yoshida: phys. stat. sol. (c) Vol. 3 (2006), p. 1515

[9] H. W. Leite Alves, J. L. A. Alves, L. M. R. Scolfaro, J. R. Lite: Mater. Sci. Eng. Vol. B93, p. 90

APPENDIX D

Accepted for publication in
the Advanced Materials Research

High Resolution X- ray Diffraction and Raman Scattering Studies of Cubic-phase InN Films Grown by MBE

S. Kuntharin[1,a], S. Sanorpim[1,b], H. Yaguchi[2,c],
Y. Iwahashi[2], M. Orihara[2], Y. Hijakata[2] and S. Yoshida[2]

[1]Department of physics, Faculty of Science, Chulalongkorn University, Bangkok 10330, Thailand
[2]Department of Electrical and Electronic System Engineering, Faculty of Engineering,
Saitama University, Saitama-shi 338-8570, Japan
[a]saman.k@student.chula.ac.th, [b]sakuntam.s@chula.ac.th, [c]yaguchi@opt.ees.saitama-u.ac.jp

Keywords: c–InN; h-InN; MBE; Raman scattering; high-resolution X-ray diffraction

Abstract: We demonstrate the use of high resolution X-ray diffraction and Raman scattering to assess the generation of hexagonal-phase in the cubic-phase InN (c-InN) films on MgO substrates grown by molecular beam epitaxy with a cubic-phase GaN buffer layer. The X-ray reciprocal-lattice space mapping was used to examine the hexagonal-phase generated on the cubic (111) planes in the c-InN films. Ratio of hexagonal to cubic components in the c-InN grown layers was estimated from the ratio of the integrated X-ray diffraction intensities of cubic (002) and hexagonal (10-11) reflections measured by ω–scans. Amount of hexagonal-phase presented in the c-InN films was determined in the range of 6% to 24%. It was found that the Raman characteristics are also sensitive to hexagonal-phase incorporation in the c-InN films. For the lowest amount of hexagonal-phase (6%), only Raman scattering characteristics of c-InN was observed, indicating formation of a small amount of stacking faults, which not affected on the vibrational property. Based on our results, relatively easy access to the generation of hexagonal-phase suggests that it may be very useful for HRXRD and Raman scattering measurements of c-InN.

Introduction

Indium nitride (InN) has been extensively studied due to its promising applications in long wavelength optoelectronic devices. Generally, InN crystallizes in either a thermodynamically stable hexagonal (wurtzite) structure or a metastable cubic (zinc-blend) structure. Recently, numerous studies have concentrated on the growth of hexagonal-phase InN (h-InN) [1, 2]. However, the interest on the cubic-phase InN (c-InN) has been motivated by a desire to explore its advantages including lower phonon scattering and superior electronic properties [3]. Due to metastability of c-InN crystal, the hexagonal-phase often coexists with the cubic phase. Based on our knowledge, the coexistence of hexagonal and cubic phase, for an example, in GaN is often examined using X-ray diffraction [4], transmission electron microscopy (TEM) [5] or Raman scattering [6].

In this works, high resolution X-ray diffraction (HRXRD) and Raman spectroscopy were applied to examine the formation of hexagonal-phase in the c-InN films grown on MgO (001) substrates grown by plasma molecular beam epitaxy (MBE) using a c-GaN buffer layer. To clarify the effect of hexagonal phase generation on the structural quality, correlation between hexagonal phase inclusion and Raman scattering characteristics as well as crystal orientation was measured.

Experiment

The c-InN films used in this study were grown on MgO (001) substrates by MBE using c-GaN as a buffer layer. Details of the growth have been described elsewhere [7]. A c-GaN buffer layer with thickness of 400 nm was first deposited on the MgO substrate at 700°C. Then, c-InN film was grown for 1 hour at 300-550°C with various V/III ratios. Amount of hexagonal phase inclusion in the c-InN films was determined from the ratio of the integrated XRD intensities of cubic (002) and hexagonal (10-11) reflections measured by ω–scan extracted from the X-ray reciprocal-lattice space mappings (RSMs) [4]. The Raman spectroscopy was performed to clarify the vibrational
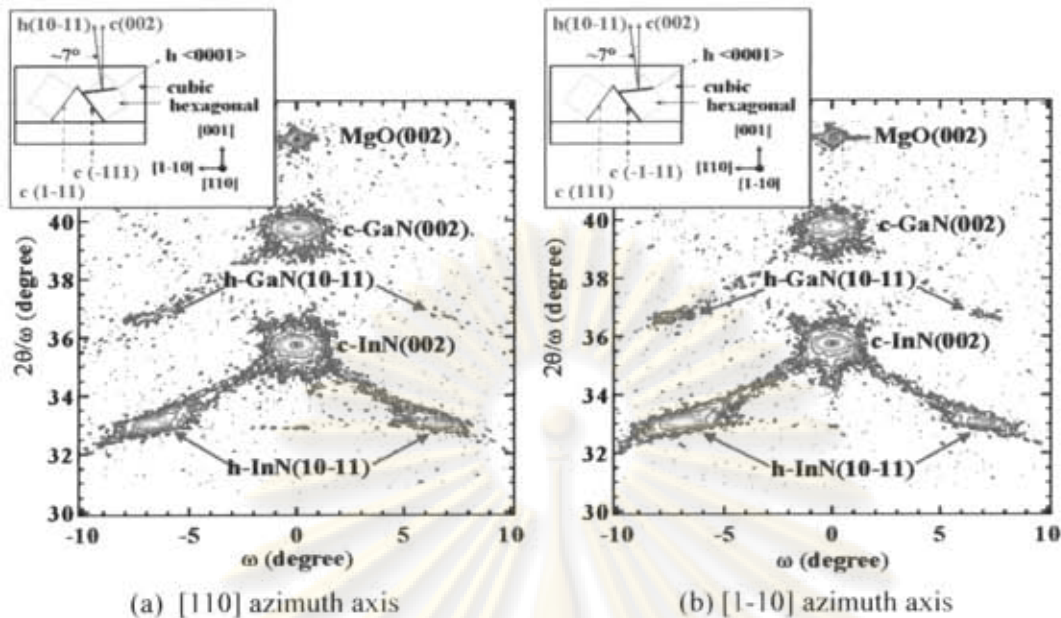
Figure 1. Typical X-ray reciprocal-lattice space mappings of the c-InN layer grown on MgO substrate using a c-GaN buffer layer measured along the (a) [110] and (b) [1-10] azimuth axes. Inset figures show the crystal relationship between cubic (002) and hexagonal (10-11) planes.

properties related to the cubic and hexagonal structures. The HRXRD measurements were carried out using a four-circle X-ray diffractometer (Bruker-AXS D8 DISCOVER). The Raman scattering experiments were carried out using the Renishaw Ramanscope RM1000. The 514.5 nm line of an Ar$^+$ laser is used as a light source. The scattered light was detected in the backscattering geometry, namely $z(x, y)\bar{z}$.

Results and discussion

Figures 1(a) and 1(b) show typical X-ray RSMs of c-InN film on MgO substrate with a c-GaN buffer layer measured along the [110] and [1-10] azimuth axes, respectively. As seen in the figures, the horizontal axis ω is the tilted angle related to the rocking curve indicating crystal orientation and the vertical axis $2\theta/\omega$ is the diffraction angle related to the lattice spacing. For both azimuth axes, the tilted angles between MgO (002) and cubic (002) and hexagonal (10-11) planes in both the c-GaN buffer and the InN layers are 0° and ±7°, respectively. This demonstrates that the hexagonal-phase presented in both the c-GaN and c-InN layers is mainly constructed on the cubic (111) surfaces. This indicates that the crystal orientation relationship between hexagonal phase inclusion and c-InN is $(0001)_h$ // $(111)_c$. According to this crystalline relationship, which is shown in the inset figures, for cubic (002) plane, its peak should appears only one time and it is generated from all the cubic planes in the irradiated region. However, the same diffraction information will appear two times in the RSMs, one for the [110] azimuth axis and two for the [1-10] azimuth axis, repeatedly. On the other hand, for hexagonal (10-11) planes, the diffraction peaks appear four times and each peak is not scattered from all the hexagonal plane, but only a portion whose (0002) plane parallel to the corresponding {111} planes.

It is well known that XRD intensities are usually different for different lattice planes. However, there is no report on the XRD intensity of c-InN compared with that of h-InN, owing to a lack of a high quality thick c-InN layer. Thus, we calculated the theoretical XRD intensities of the ω-scan for both the c-InN (002) and h-InN (10-11) planes. Detailed calculation can be found in the literature [4]. Table 1 summarizes the relative theoretical calculated XRD intensities from the cubic (002) and hexagonal (10-11) planes of InN. To compare with the calculated results from ref. [4], in addition, we also calculated the XRD intensities from the cubic (002) and hexagonal (10-11) planes for GaN. The calculated results show that the XRD intensity from the hexagonal (10-11) plane was nearly equal to
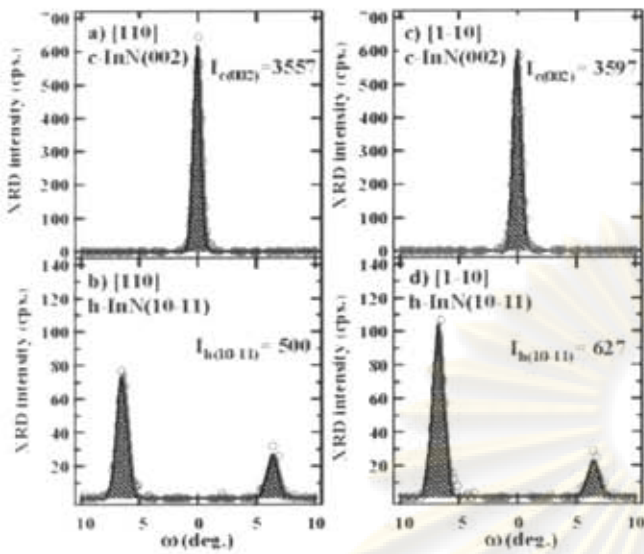
Figure 2. ω-scan profiles of the cubic (002) and hexagonal (10-11) reflections for InN measured along the (a and b) [110] and (c and d) [1-10] azimuth axes, which were extracted from RSM data shown in Figs. 1(a) and 1(b), respectively.

Table 1. Theoretical calculated XRD intensities of InN and GaN.

Crystals	planes	2θ (deg.)	I (10^5)	$I_h/I_c = \alpha$
InN	c(002)	36.0	26.85	-
	h(10-11	33.2	27.15	1.01
GaN	c(002)	39.8	8.41	-
	h(10-11	36.8	8.97	1.07 (1.06)[4]

that from the cubic (002) plane. Therefore, ratio of hexagonal to cubic phase component (hexagonal phase inclusion, %h-InN) in the c-InN layers can be obtained by [8]:

$$\%h - InN = \frac{I_{h(10-11)}}{I_{h(10-11)} + \alpha \cdot \overline{I}_{c(002)}} \times 100\% . \ (1)$$

where $I_{h(10-11)}$ and $\overline{I}_{c(002)}$ were the integrated XRD intensities of hexagonal (10-11) plane and the average integrated XRD intensity of cubic (002) plane, respectively, which were obtained by ω-scan in X-ray RSM. α is referred to the ratio of $I_{h(10-11)}/\overline{I}_{c(002)}$. Figure 2 shows ω-scan profiles of the cubic (002) and hexagonal (10-11) reflections, which were extracted from the X-ray RSM data shown in Fig. 1. In Fig. 2, the integration data is also calculated and illustrated. To examine hexagonal phase in the c-InN layer, the integrated XRD intensities from hexagonal (10-11) planes were summed up. On the other hand, the integrated XRD intensities from the cubic (002) plane were averaged due to its reflected from the same plane. Amounts of hexagonal phase inclusion in the c-InN layers used in the present study were calculated in the range of 6%–24%. In addition, full width at half maximum (FWHM) of ω-scan profiles for the c-InN (002) plane was increased from 22 min to 28 min with increasing hexagonal phase inclusion from 6% to 24%, as shown in Fig.4, indicating a degradation of crystal quality with incorporation of h-InN. To investigate the possible impact of the hexagonal phase incorporation on the vibrational properties in the c-InN films, Raman scattering characteristics of all the c-InN and h-InN structures are considered. Figure 3 shows Raman spectra of the c-InN films with different amounts of hexagonal phase inclusion. The red-dashed and blue-dotted lines indicate characteristic phonon frequencies of cubic [9] and hexagonal [10] structures, respectively. It is found that the Raman characteristics are very sensitive to
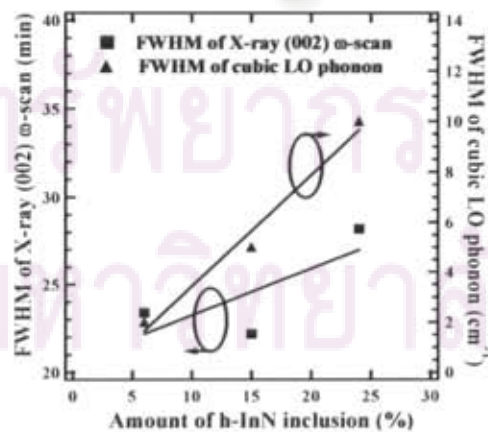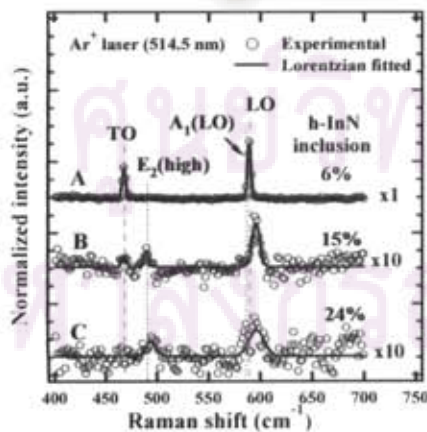

Figure 3. (left) Raman spectra of the c-InN films with different amounts of hexagonal phase inclusion.
Figure 4. (right) FWHM of X-ray (002) ω-scan profiles and Raman linewidth of cubic LO phonon of c-InN as a function of hexagonal phase inclusion in the c-InN films.

hexagonal-phase incorporation in the c-InN films. For the lowest hexagonal phase incorporation (~ 6%), two Raman shift frequencies were clearly observed at 468 cm^{-1} and 588 cm^{-1}, which are attributed to the cubic TO and LO phonon modes, respectively. The Raman linewidth of these two peaks is 2 cm^{-1}. This indicates that the crystal quality of c-InN layer with hexagonal phase inclusion lower than 6% considerably high. As the hexagonal phase inclusions increase to 15% and 24%, the Raman shift frequencies at about 595 cm^{-1} was observed. This suggests that such Raman shift frequency is attributed to the cubic LO phonon mode [7] due to the strain inside the c-InN film. Moreover, the hexagonal E_2 (high) phonon mode was also observed. These results illustrate that the hexagonal phase structure is dominated in the c-InN layers with relatively high hexagonal phase incorporation (> 6%). The difference in the Raman spectra is in connection with the difference amount of hexagonal phase inclusion in the c-InN films, which agrees well with the results of HRXRD. In order to further assess the effect of hexagonal phase generation on crystal quality of c-InN films, FWHM of cubic LO phonon is considered as shown in Fig. 4. Thus, our Raman scattering results suggest that the crystal quality of c-InN film with hexagonal phase inclusion lower than 6% is remarkably high with no incorporation of hexagonal single crystal (h-InN), which supports our HRXRD results.

Conclusions

HRXRD and Raman scattering measurements were performed to analyze the generation of hexagonal phase in the c-InN films on MgO substrates grown by MBE with a c-GaN buffer layer. The orientation relationship between h-InN and c-InN is $(0001)_h$ // $(111)_c$. The amount of hexagonal phase inclusion can be estimated from the ratio of the integrated XRD intensities of cubic (002) and hexagonal (10-11) reflections measured by ω–scan in the X-ray RSMs. The amount of hexagonal phase inclusion in the c-InN films was determined in the range of 6% to 24%. In addition, the Raman scattering characteristics of c-InN films are shown to be very sensitive to the presence of the single-crystal h-InN, which good supports the results of HRXRD studies.

Acknowledgements
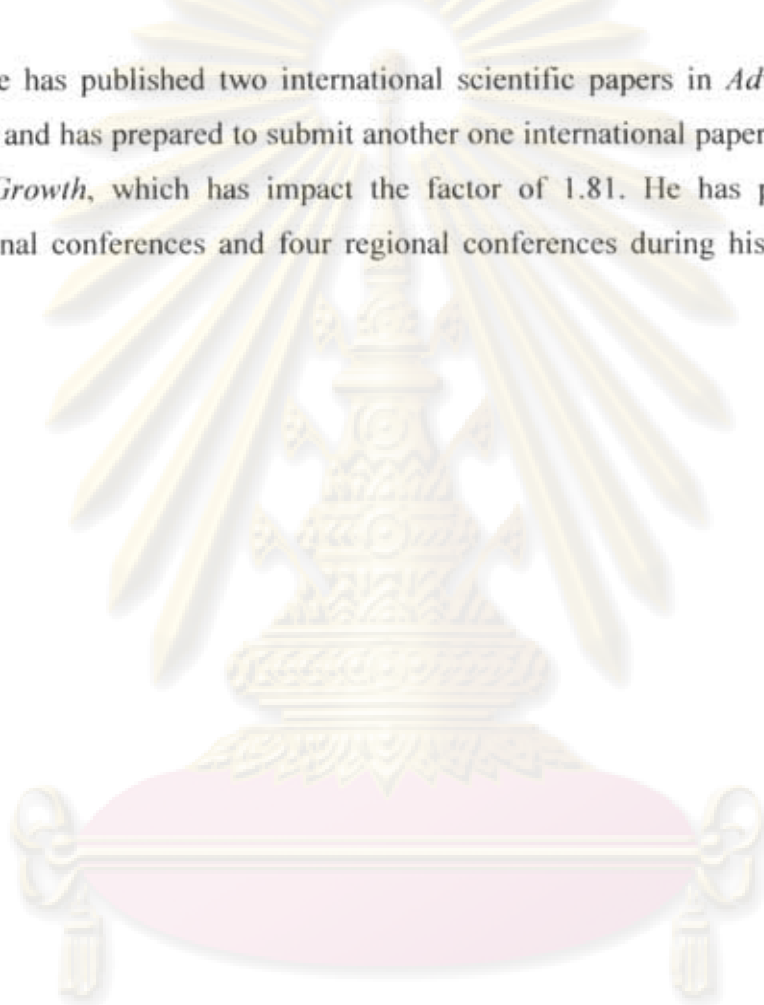
References

[1] Ming-Chin Lee, Heng-Ching Lin, Yung-Chung Pan, Chen-Ke Shu, Jehn Ou, Wen-Hsing Chen and Wei-Kuo Chen: Appl. Phys. Lett. Vol. 73 (1998), p. 2606.

[2] T. Inushima, V.V. Mamutin, V.A. Vekshin, S.V. Ivanov, T. Sakon, M. Motokawa, S. Ohoya: Journal of Crystal Growth Vol. 227–228 (2001), p. 481.

[3] A. G. Bhuiyan, A. Hashimoto, and A. Yamamoto: J. Appl. Phys. Vol. 94 (2003), p. 2779.

[4] H. Tsuchiya, K. Sunaba, S. Yonemura, T. Suemasu, and H. Seki: Jpn. J. App. Phys. Vol. 36 (1997), p. L1.

[5] S. Suandon, S. Sanorpim, K. Yoodee, and K. Onabe: Thin Solid Films Vol. 515 (2007), p. 4393.

[6] H. Yaguchi, J. Wu, B. Zhang, Y. Segawa, H. Nagasawa, K. Onebe, and Y. Shiraki: Journal of Crystal Growth Vol. 195 (21998), p. 323.

[7] Y. Iwahashi, H. Yaguchi, A. Nishimoto, M. Orihara, and Y. Hijikata: phys. stat. sol. (c) Vol. 3 (2006), p. 1515.

[8] B. Qu, X. H. Zheng, Y. T. Wang, Z. H. Feng, S. A. Liu, S. M. Lin, H. Yang, and J. W. Liang: Thin Solids Films. Vol. 392 (2001), p. 29.

[9] A. Tabata, A. P. Lima, L. K. Teles, L. M. R. Scolfaro, and J. R. Leite, V. lemos, B. Schöttker, T. Frey, D. Schikora, and K. Lischka: Appl. Phys. Lett. Vol. 74 (1999), p. 362.

[10] O. Birot, B. Maleyre, S. Ruffenach, B. Gil, C. Pinquier, F. Demangeot, and J. Frandon: Journal of Crystal Growth. Vol. 269 (2004), p. 22.

VITAE

Mr. Saman Kuntharin was born on April 5, 1982 in Nongkhai, Thailand. He has been a student in the Development and Promotion for Science and Technology Talents Project (DPST). He received his Bachelor degree of Science in Physics from Khonkean University in 2004, and continued his Master's degree study in 2005.

He has published two international scientific papers in *Advanced Materials Research* and has prepared to submit another one international paper to the *Journal of Crystal Growth*, which has impact the factor of 1.81. He has participated three international conferences and four regional conferences during his Master's degree study.